OPTIMIZATION, FABRICATION, AND CHARACTERIZATION OF DUAL-BAND INGAAS NBN PHOTODETECTORS

A THESIS SUBMITTED TO
THE GRADUATE SCHOOL OF NATURAL AND APPLIED SCIENCES
OF
MIDDLE EAST TECHNICAL UNIVERSITY

BY

ALPER ŞAHİN

IN PARTIAL FULFILLMENT OF THE REQUIREMENTS
FOR
THE DEGREE OF MASTER OF SCIENCE
IN
ELECTRICAL AND ELECTRONICS ENGINEERING

AUGUST 2022

Approval of the thesis:

OPTIMIZATION, FABRICATION, AND CHARACTERIZATION OF DUAL-BAND INGAAS NBN PHOTODETECTORS

submitted by **ALPER ŞAHIN** in partial fulfillment of the requirements for the degree of **Master of Science in Electrical and Electronics Engineering Department, Middle East Technical University** by,

Prof. Dr. Halil Kalıpçılar
Dean, Graduate School of **Natural and Applied Sciences** _____

Prof. Dr. İlkay Ulusoy
Head of Department, **Electrical and Electronics Engineering** _____

Assoc. Prof. Dr. Serdar Kocaman
Supervisor, **Electrical and Electronics Engineering, METU** _____

Examining Committee Members:

Prof. Dr. Cengiz Beşikci
Electrical and Electronics Engineering, METU _____

Assoc. Prof. Dr. Serdar Kocaman
Electrical and Electronics Engineering, METU _____

Prof. Dr. Tayfun Akın
Electrical and Electronics Engineering, METU _____

Assist. Prof. Dr. Ahmet Cemal Durgun
Electrical and Electronics Engineering, METU _____

Prof. Dr. Yüksel Ergün
Physics, Eskişehir Technical University _____

Date: 31.08.2022

I hereby declare that all information in this document has been obtained and presented in accordance with academic rules and ethical conduct. I also declare that, as required by these rules and conduct, I have fully cited and referenced all material and results that are not original to this work.

Name, Surname: Alper Şahin

Signature :

ABSTRACT

OPTIMIZATION, FABRICATION, AND CHARACTERIZATION OF DUAL-BAND INGAAS NBN PHOTODETECTORS

Şahin, Alper
M.S., Department of Electrical and Electronics Engineering
Supervisor: Assoc. Prof. Dr. Serdar Kocaman

August 2022, 84 pages

Shortwave and extended shortwave infrared regions are attracting significant attention since many applications utilize infrared wavelengths between 1-3 μm. Gas sensing, spectroscopy, food safety, astronomy, imaging, and optical communication are among the applications that utilize SWIR/eSWIR detectors. Typically Low radiation levels at SWIR/eSWIR bands require SWIR/eSWIR photodetectors to have outstanding performance, including high quantum efficiency and very low dark current. Photodetectors built with InGaAs lattice matched to InP provide the best performance at affordable costs, although they suffer from surface leakage currents. However, extending the cut-off wavelength from 1.7 μm to 2.5 μm causes material quality to decrease significantly due to the lattice mismatch between InGaAs/InP. nBn detectors, introduced relatively recently, offer effective solutions to dark current mechanisms due to surface leakage and material-related problems. In the scope of this thesis study, an nBn type InGaAs photodetector at 1.7 μm / 2.0 μm with dual-band capacity was designed, fabricated, and characterized. An unintentionally doped InAlGaAs layer was placed between two n-type InGaAs absorbers as the barrier material. p-type delta doping was applied to the barrier to arrange the band structure of the overall device so that

there is no valance band offset that hinders the flow of the photoexcited minority carriers. Dark current measurements at 300 K on a large area pixel yield 3.40 mA/cm^2 and 0.61 $\mu A/cm^2$ for the eSWIR and SWIR sides, respectively. Dark current values at 200 K for the eSWIR decreased to 8.05 $\mu A/cm^2$, while the SWIR side provided 1.09 nA/cm^2. Arrhenius plots for both SWIR and eSWIR sides presented a fixed slope, meaning tunneling and surface components were successfully eliminated. Suppression of surface leakage currents was also verified with dark current measurements on different area pixels. Optical measurements without anti-reflective coating yielded 67% and 53% peak quantum efficiencies for eSWIR and SWIR sides, respectively. High quantum efficiency values acknowledged the absence of valance band offset.

Keywords: Infrared, Photodetector, Dual Band, Dual Color, Shortwave, SWIR, InGaAs, nBn

ÖZ

ÇİFT BANTLI INGAAS NBN FOTOALGILAYICILARIN OPTİMİZASYONU, ÜRETİMİ VE KARAKTERİZASYONU

Şahin, Alper
Yüksek Lisans, Elektrik ve Elektronik Mühendisliği Bölümü
Tez Yöneticisi: Doç. Dr. Serdar Kocaman

Ağustos 2022 , 84 sayfa

Birçok uygulama 1-3 μm aralığındaki kızılötesi dalga boylarını kullandığı için Kısa Dalga Boylu Kızılötesi (KDK) ve Genişletilmiş Kısa Dalga Boylu Kızılötesi (gKDK) bölgeleri oldukça ilgi çekmektedir. Gaz algılama, spektroskopi, gıda güvenliği, astronomi, görüntüleme ve optik iletişim bu uygulamalar arasında yer almaktadır. Tipik olarak KDK/gKDK bantlarındaki düşük radyasyon seviyeleri KDK/gKDK fotoalgılayıcılarının yüksek kuantum verimliliği ve düşük karanlık akım değerlerine sahip üstün bir performans göstermesini gerektirmektedir. InP'a örgü eşlenik InGaAs malzemeler ile üretilen fotoalgılayıcılar, yüzey kaçak akımlarından dolayı olumsuz etkilenmelerine rağmen kabul edilebilir maliyetlerle en iyi performansı sunmaktadır. Ancak algılama kesim dalga boyunun 1.7 μm seviyesinden 2.5 μm seviyesine doğru uzaması, 1.7 μm dalga boyundan uzun dalga boylarında InGaAs ve InP örgü eşlenik olmadığı için malzeme kalitesinin ciddi ölçüde düşmesine sebep olmaktadır. Görece daha yeni olan nBn tipi algılayıcılar ise yüzey kaçak akımları ve malzeme kaynaklı karanlık akım mekanizmalarına karşı etkili çözümler sunmaktadır. Bu tez çalışması kapsamında, çift bant algılama kabiliyetine sahip 1.7 μm / 2.0 μm dalga boyunda ça-

lışan nBn tipi InGaAs fotoalgılayıcı tasarlanmış, üretilmiş ve karakterize edilmiştir. İstem dışı seviyede katkılanmış InAlGaAs katmanı, iki InGaAs n-tipi emici katman arasına bariyer olarak yerleştirilmiştir. Bariyere p-tipi delta katkılama uygulanarak bütün cihazın bant yapısı, valans bandında fotouyarılmış taşıyıcıların akışını engelleyecek bir kayma oluşmayacak şekilde ayarlanmıştır. 300 K sıcaklıkta ve büyük alanlı bir piksel üzerinde yapılan karanlık akım ölçümü KDK ve gKDK kısımları için sırasıyla 3.40 mA/cm^2 ve 0.61 $\mu A/cm^2$ karanlık akım değerlerini vermiştir. 200 K sıcaklıktaki karanlık akım yoğunluğu değerleri gKDK bandı için 8.05 $\mu A/cm^2$ seviyesine düşerken KDK bandı 1.09 nA/cm^2 seviyesinde karanlık akım yoğunluğu vermiştir. Arrhenius grafikleri hem KDK hem de gKDK bantları için tünelleme ve yüzey bileşenlerinin başarılı bir şekilde elendiği anlamına gelen sabit bir eğim göstermiştir. Yüzey kaçak akımlarının bastırıldığı değişik alanlı pikseller üzerinde yapılan karanlık akım yoğunluğu ölçümleriyle ayrıca doğrulanmıştır. Yansıma önleyici kaplama olmaksızın gerçekleştirilen optik ölçümler gKDK ve KDK kısımları için sırasıyla 67% ve 53% tepe kuantum verimliliği değerleri ölçülmüştür. Yüksek kuantum verimliliği değerleri valans bandında bir kayma olmadığını doğrulamıştır.

Anahtar Kelimeler: Kızılötesi, Fotoalgılayıcı, Çift Bantlı, Çift Renkli, Kısa Dalga Boylu Kızılötesi, InGaAs, nBn

Anneme ve Babama

ACKNOWLEDGMENTS

First, I would like to express my gratitude to my thesis advisor, Assoc. Prof. Serdar Kocaman for his guidance and advice during my thesis study. Certainly, this thesis study would not survive without his support.

I would like to thank Prof. Dr. Cengiz Beşikci for his valuable technical comments and critics during the time I spent in ODTU-KANAL.

I would like to thank Prof. Dr. Tayfun Akın, Assist. Prof. Dr. Ahmet Cemal Durgun and Prof. Dr. Yüksel Ergün for being in my thesis committee.

I would like to thank Scientific and Technological Research Council of Turkey (TUBITAK) for funding this study under grant number 118E771.

I would like to thank my colleagues, Musa Selim Gül, Onur Akdeniz, Fatih Uzgur, Halil İbrahim Binici, Veysel Balcı, Necati Işık, and Oğuz Onur Güngör for increasing the survival probability in the working environment with their technical abilities as well as their friendliness. I also would like to thank Özgür Şen for keeping the laboratory working.

I would like to thank Furkan Alp Eren and Ahmet Gürhan for always truly being with me since we met during high school. I would like to thank Esen Özbay for her friendliness.

Last but not least, I would like to thank my father and mother since they have always supported me with the deepest love throughout my life.

TABLE OF CONTENTS

ABSTRACT v

ÖZ vii

ACKNOWLEDGMENTS x

TABLE OF CONTENTS xi

LIST OF TABLES xiv

LIST OF FIGURES xv

LIST OF ABBREVIATIONS xix

CHAPTERS

1 INTRODUCTION 1

1.1 Fundamentals of Infrared Radiation 2

1.2 Common Infrared Photodetector Types 6

1.3 Figure of Merits of Infrared Photodetectors 11

1.3.1 Responsivity 11

1.3.2 Dark Current 13

1.3.3 Noise 13

1.3.4 Detectivity and Noise Equivalent Power 14

2 SWIR/ESWIR PHOTODETECTOR, APPLICATIONS AND STATUS . . . 17

2.1 Applications 17

2.2 Material Systems for SWIR/eSWIR Detection 20
2.2.1 Mercury Cadmium Telluride (HgCdTe) 20
2.2.2 Indium Gallium Arsenide (InGaAs) 21
2.2.3 The 6.1 Å Family 24
2.3 Recent Examples from the Literature 26
3 DESIGN, FABRICATION AND CHARACTERIZATION OF A DUAL-BAND INGAAS NBN PHOTODETECTOR 31
3.1 Properties and Advantages of Barrier Photodetectors 31
3.1.1 Dark Current Components in pn Junctions 31
3.1.2 Unipolar Barrier Photodiodes 34
3.1.3 nBn Photodetectors 35
3.2 Design 37
3.2.1 InGaAs nBn Photodetector at 2.2 μm 41
3.2.2 Dual-Band InGaAs nBn Photodetector at 1.7 μm / 2.2 μm . . . 50
3.3 Realization 56
3.3.1 Growth Using Molecular Beam Epitaxy 56
3.3.2 Fabrication of the Photodetector 58
3.4 Characterization 60
3.4.1 Optical Performance 60
3.4.2 Dark Current 64
3.4.3 Noise 68
3.4.4 Specific Detectivity 70
4 CONCLUSION AND FUTURE WORK 71

REFERENCES 75

LIST OF TABLES

TABLES

Table 3.1 Simulation parameters 40

LIST OF FIGURES

FIGURES

Figure 1.1 Spectral exitance diagrams for various blackbody temperatures. . 3

Figure 1.2 Spectral atmospheric transmission of infrared radiation for a distance of 1800 m with a water precipitation of 17 mm. Redrawn after [7]. 5

Figure 1.3 An illustration of a photoconductor with reading circuit. 7

Figure 1.4 An illustration of a photodiode with n-type absorber. 7

Figure 1.5 Energy band diagram of conduction band of a typical AlGaAs/-GaAs QWIP. Adapted and redrawn after [8]. 8

Figure 1.6 Energy band diagram a typical GaInSb/InAs type-II superlattice detector. Adapted and redrawn after [10]. 9

Figure 1.7 A typical thermocouple and thermopile structure. Adapted and redrawn after [11]. 10

Figure 1.8 A typical microbolometer structure. Redrawn after [12]. 11

Figure 2.1 Illumination levels of various light sources in the shortwave infrared region. Adapted and redrawn from [20]. 18

Figure 2.2 Illumination levels due to the night glow with different moon conditions. Adapted and redrawn from [21]. 19

Figure 2.3 Bandgap of HgCdTe vs. CdTe mole fraction at 78 K and 300 K. Adapted and redrawn after [28]. 20

Figure 2.4 Bandgap and lattice constants of semiconductors in the InP material system. Solid lines represent direct bandgaps while dashed lines represent indirect bandgaps. Adapted from [34]. 23

Figure 2.5 Energy band diagrams presenting Fermi level pinning at the surface of InGaAs. 24

Figure 2.6 Bandgap and lattice constants of semiconductors in the 6.1 Å Family. Solid lines represent direct bandgaps while dashed lines represent indirect bandgaps. Adapted from [34]. 25

Figure 2.7 Band alignments of semiconductors in the 6.1 Å Family. Boxes represent semiconductors, where bottom edges represent valence band and top edges represent conduction bands. Adapted from [40]. 26

Figure 3.1 Illustration of various current sources in pn junctions using energy band diagrams. (a) Photocurrent, (b) diffusion current, (c) generation-recombination current (c), and (d) trap-assisted tunneling are presented. Adapted and redrawn after [54]. 32

Figure 3.2 (a) Illustration of filtering achieved by unipolar barrier placed on the n-side, (b) on the p-side. Adapted and redrawn after [54,55]. 34

Figure 3.3 Illustration of flow of photocurrent and dark current components in an nBn photodetector. Adapted and redrawn after [56]. 35

Figure 3.4 (a) Comparison of the flow of photocurrent and dark current components in an nBn photodetector, (b) and in a unipolar photodiode. Adapted and redrawn after [54,55,56]. 36

Figure 3.5 Comparison of the Arrhenius plots of an nBn photodetector and a photodiode. Adapted and redrawn after [56]. 37

Figure 3.6 (a) Simulated band alignments between InGaAs and graded InAlGaAs assuming no doping, (b) assuming doping levels except the delta doping. 42

Figure 3.7 Epilayer of the proposed nBn structure. 43

Figure 3.8 (a) Simulated band diagrams of the nBn photodetector at bias voltages of 0 mV, (b) and 240 mV. Solid lines represent conduction and valence bands while dashed lines represent quasi-Fermi levels. 44

Figure 3.9 (a) Dark current values, and (b) photocurrent values at delta doping profiles with various thicknesses and doping densities. 45

Figure 3.10 Epilayer of the pn structure. 46

Figure 3.11 Comparison of dark currents of nBn and pn. 47

Figure 3.12 Built-in electric fields of nBn and pn structured photodetectors. . 47

Figure 3.13 SRH recombination rates observed in nBn and pn structured photodetectors. 48

Figure 3.14 Dark currents calculated for different SRH recombination lifetimes for nBn and pn. 49

Figure 3.15 Comparison of photocurrents of nBn and pn. 49

Figure 3.16 Epilayer of the npn structure. 50

Figure 3.17 Dual-band operation. (a) SWIR mode in nBn, (b) in npn, (c) eSWIR mode in nBn, (d) in npn. 51

Figure 3.18 Dark current density vs. SWIR absorber doping density. 52

Figure 3.19 Band diagrams for different SWIR absorber doping levels, where band-bending occurring between the SWIR absorber and the barrier should be noticed. 52

Figure 3.20 SRH rates for different SWIR absorber doping levels. 53

Figure 3.21 Photo current density vs. SWIR absorber doping density. 54

Figure 3.22 Dark current-voltage characteristics of nBn and npn photodetectors. 54

Figure 3.23 Photocurrent-voltage characteristics of nBn and npn photodetectors. 55

Figure 3.24 Schematical drawing of a typical MBE system. 57

Figure 3.25 Fabrication of the Photodetector. 58

Figure 3.26 (a) Fabricated photodetector chip ready for flip-chip bonding, (b) optical microscope image showing different area pixels, (c) SEM images of $20 \times 20\ \mu m^2$ pixels with insets showing etching profiles. . . . 59

Figure 3.27 Schematical drawing of a monochromator similar to the one used for characterization. 60

Figure 3.28 Illustration of lateral collection, where red dots demonstrate photogenerated carriers. 62

Figure 3.29 Photocurrent readings from signals with different areas for both SWIR and eSWIR regions. 62

Figure 3.30 Room temperature quantum efficiencies at bias voltages -50 mV for SWIR and 300 mV for eSWIR. 63

Figure 3.31 Temperature dependent dark current density vs. applied bias. . . 64

Figure 3.32 Arrhenius plot for current density. 65

Figure 3.33 Arrhenius plot for resistance area product. 66

Figure 3.34 Dark current densities in different sized pixels. 67

Figure 3.35 Noise characteristic of the eSWIR detector for a biasing voltage of +300 mV at different temperatures. 68

Figure 3.36 Arrhenius plot of noise characteristic of the eSWIR detector for a biasing voltage of +300 mV at different temperatures. 69

Figure 3.37 Specific detectivity of the eSWIR detector for a biasing voltage of +300 mV at room temperature. 70

LIST OF ABBREVIATIONS

IR	Infrared
NIR	Near Infrared
SWIR	Shortwave Infrared
MWIR	Midwave Infrared
LWIR	Longwave Infrared
VLWIR	Very Longwave Infrared
FIR	Far Infrared (FIR)
GR	Generation - Recombination
SRH	Schokley - Read - Hall
QWIP	Quantum Well Infrared Photodetector
T2SL	Type-II Superlattice
QE	Quantum Efficiency
NETD	Noise Equivalent Temperature Distance
NEI	Noise Equivalent Irradiance
TCAD	Technology Computer Aided Design
MBE	Molecular Beam Epitaxy
XRD	X-Ray Diffraction
RHEED	Reflecting High Energy Electron Diffraction
FPA	Focal Plane Array

CHAPTER 1

INTRODUCTION

Infrared(IR) radiation was discovered nearly 200 years ago by the simple thermometer experiment of W. Herschel. The experiment consisted of a prism to disperse the incident sunlight and a thermometer to observe the effect of incident light on temperature. The unexpected temperature change even when no color is incident to temperature revealed that the sunlight includes some form of radiation that is invisible to the human eye. Since the discovery of the infrared region, IR radiation has become an essential part of our daily life with its diverse applications such as thermal imaging, optical communication, spectroscopy, gas sensing, and others [1].

The infrared region covers wavelengths from 0.7 μm to 100 μm of the electromagnetic spectrum, where subregions are utilized for particular applications using different approaches and technologies. On the other hand, this thesis study will focus on only a small portion covering between 0.7 μm to 2.5 μm, called the short wave infrared (SWIR) region. Among the alternative material systems and technologies, this thesis presents the design, fabrication, and characterization of an nBn type Indium Gallium Arsenide (InGaAs) photodetector.

Chapter 1 cites the basics of infrared radiation, photodetector technologies, and figure of merits of infrared photodetectors.

Chapter 2 addresses detailed features of the SWIR region and covers the literature regarding the SWIR region applications, material systems used for SWIR detectors, and SWIR photodetector design approaches.

Chapter 3 discusses barrier type infrared photodetector and presents the design, realization, and characterization of a dual-band InGaAs nBn photodetector. Detailed dark

current characterization includes measurement of FPA-like pixels as well as large-area pixels at different temperatures. Optical measurements reveal the high optical responsivity for both bands, whose cut-off wavelengths are 1.7 μm and 2.0 μm.

Chapter 4 concludes the thesis study and discusses some possible future work.

It should be noted that some parts of the material presented in this thesis were published in the literature. The theoretical study was presented in SPIE Defense and Commercial Sensing, including nBn photodetector design and sensitivity analysis for the possible growth deviations [2]. The possibility of dual-band operation of the device discussed in this thesis study was demonstrated in Photonics West [3]. Finally, experimental and numerical results were published in Applied Physics Letters [4].

1.1 Fundamentals of Infrared Radiation

Substances having a temperature above 0 K emit radiation depending on their temperature and specific properties. Assuming a thermal equilibrium between an object and the surrounding environment, the object should emit energy equal to the energy it absorbs to maintain the thermal equilibrium. That is usually summarized as "A good absorber is a good emitter.", which is the simplest form of Kirchoff's law of thermal radiation. In addition, all forms of energy do not have to interact with the object. The energy either can be reflected from the object or can transmit through the object. However, to maintain the thermal equilibrium and conservation of energy, the sum of reflectance (ρ), transmittance (T), and absorbance (α) must equal to 1 [5]:

$$1 = \alpha + \rho + T \tag{1.1}$$

If the reflectance and transmittance are equal to zero, the equation 1.1 leads to a special case called the black body. The black body is considered as an object that absorbs all radiation incident to it and therefore emits. Since classical physics approaches fail to address the emission spectrum of the black body, the derivation of Planck's Law is considered an important milestone at the beginning of the quantum era. Planck's Law treats the light as quantized energy packets called photons, unlike the classi-

cal approach in the Rayleigh-Jeans Law diverging for high energies. Then, h being Planck's constant, λ being wavelength, k_b being Boltzman constant, T being the temperature of the blackbody, and c being the speed of light; spectral emitted radiation per unit area M_λ is given by Planck's formula as follows [6]:

$$M_\lambda(\lambda, T) = \frac{2\pi hc^2}{\lambda^5} \frac{1}{e^{hc/\lambda k_b T} - 1} \; W/cm^2\mu m \tag{1.2}$$

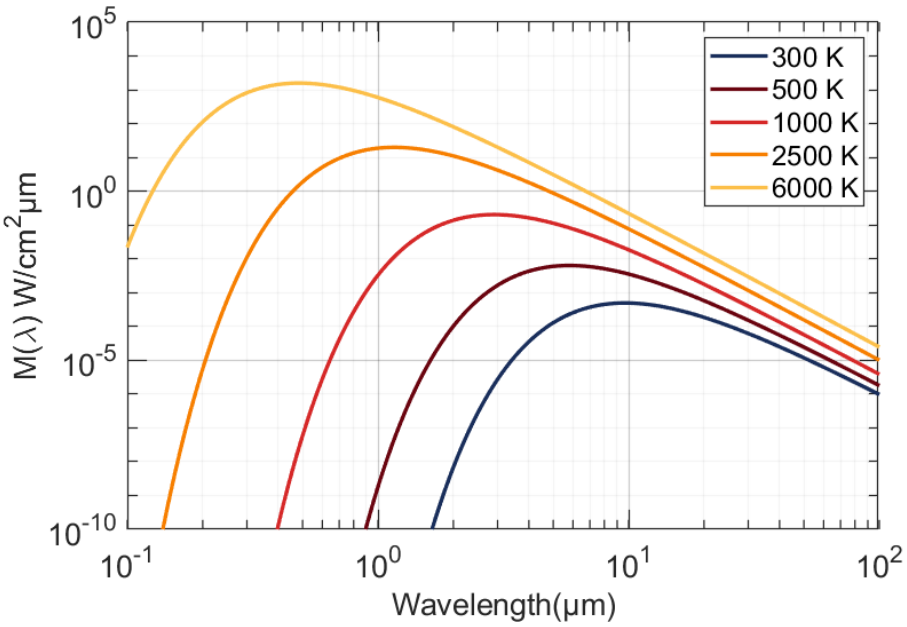


Figure 1.1: Spectral exitance diagrams for various blackbody temperatures.

Two important facts are observed when spectral emitted radiation per unit area, exitance, is obtained according to Planck's formula for different temperatures as in Figure 1.1. Peak of the exitance curve shift to shorter wavelengths, and total emitted radiation increases as temperature rises. Then, two important laws, Stefan-Boltzmann Law and Wien's Displacement Law, conclude the discussion related to the blackbody. Stefan-Boltzmann Law considers the total emitted energy from a black body at a specific temperature simply by integrating Planck's formula for the entire electromagnetic spectrum as follows:

$$M_\lambda(T) = \int_0^\infty M_\lambda(\lambda, T) d\lambda = \sigma T^4 \; W \cdot cm^{-2} \tag{1.3}$$

The Stefan-Boltzmann Law explains the increase in the total energy with increasing temperature, where $\sigma = 5.67 \times 10^{-12}\ W \cdot cm^{-2} \cdot K^{-4}$ is called Stefan-Boltzmann constant. The derivative of Planck's curve is taken with respect to wavelength and set to zero to address the blue shift of the peak with increasing temperature. As a result, Wien's Displacement Law is obtained as follows:

$$\frac{\partial M_\lambda(\lambda, T)}{\partial \lambda} = 0 \tag{1.4}$$

$$\lambda_{max} T = 2898\ \mu m \cdot K \tag{1.5}$$

where λ_{max} denotes the wavelength that has the highest spectral exitance.

Before concluding the discussion on the black body, one more essential parameter, emissivity, should be defined. All objects hotter than 0 K emit radiation but emitted radiation at a temperature or wavelength does not have to be the same as that from a black body. Then, emissivity denoted by ε is the ratio of the exitance of a source to an ideal black body:

$$\varepsilon = \frac{M_{Source}}{M_{Black\ Body}} \tag{1.6}$$

where M_{Source} and $M_{Black\ Body}$ denote the exitances of the source and an ideal black body, respectively.

Interestingly, having an emissivity value of $\varepsilon = 0.98$, the human body shows similar exitance characteristics to a black body. Considering the exitance at human body temperature in Figure 1.1, emitted radiation mainly lies in the infrared region. Then, producing devices that can detect infrared photons emitted from the human body and room temperature objects might be useful. On the other hand, the transparency of the atmosphere should be questioned to ensure that emitted infrared photons can propagate long distances without being disturbed so that infrared detectors can detect them. The infrared transmission spectrum of the atmosphere up to 15 μm is shown in Figure 1.2, in which distinct subregions can be easily identified [7].

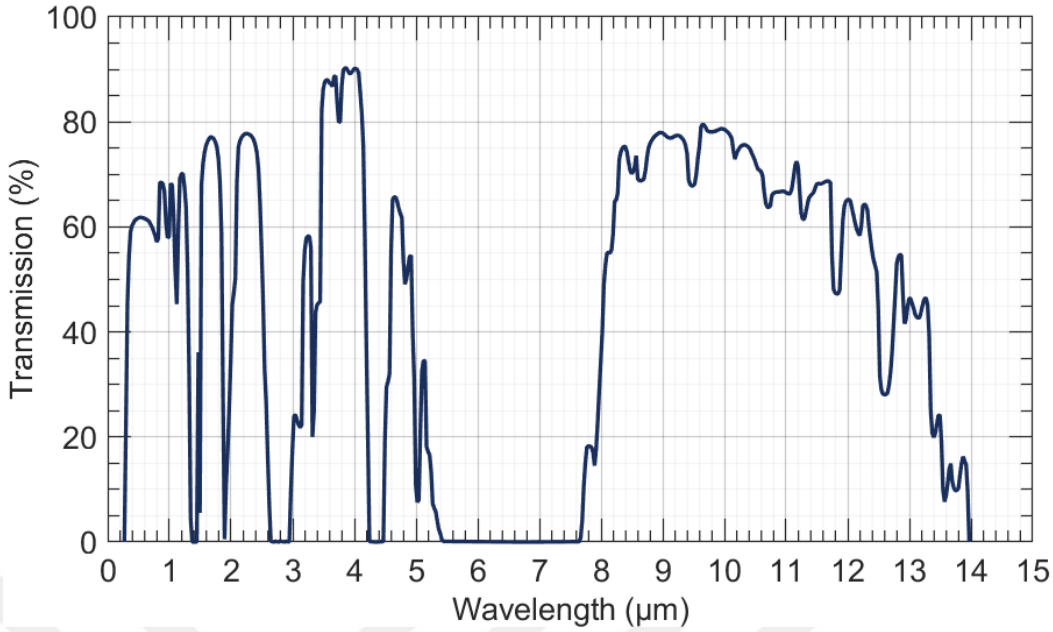


Figure 1.2: Spectral atmospheric transmission of infrared radiation for a distance of 1800 m with a water precipitation of 17 mm. Redrawn after [7].

These subregions that are transparent to infrared radiation are called atmospheric windows. In addition, the atmospheric windows are also considered to divide the infrared region into subregions as follows:

- Near Infrared (NIR): 0.7 μm - 1.0 μm
- Shortwave Infrared (SWIR): 1 μm - 3 μm
- Midwave Infrared (MWIR): 3 μm - 5 μm
- Longwave Infrared (LWIR): 8 μm - 14 μm
- Very Longwave Infrared (VLWIR): 14 μm - 30 μm
- Far Infrared (FIR): 30 μm -100 μm

MWIR and LWIR regions can be utilized to detect self-emitted photons from near room temperature objects considering Figure 1.1 and Figure 1.2 together. LWIR region is associated with the largest amount of emitted energy, while the MWIR region

provides the highest thermal contrast. SWIR and NIR regions can be utilized to detect reflecting radiation from objects due to the very low exitance.

1.2 Common Infrared Photodetector Types

Using different material systems and technical approaches, infrared detectors covering NIR to VLWIR are designed and fabricated. Here, some common types of infrared detectors will be briefly discussed.

Infrared detectors are divided into two main groups: photon detectors and thermal detectors. Photon detectors directly interact with photons and sense them, while thermal detectors detect the effects of infrared radiation. Both groups come with desired and undesired properties. When high performance, high sensitivity, and high frame rates are required for a particular application, photon detectors should be the choice. On the other hand, photon detectors come with expenses of cooling requirements and high costs. Photon detectors are based on semiconductor crystals, where photons cause interband or band-to-band transitions in the semiconductor material. Generated carriers due to the excitation by photons generate a current difference between the illuminated and dark conditions. Then, incident optical power can be obtained by measuring the photocurrent. Being direct bandgap semiconductors, HgCdTe, InAs, InGaAs, and InSb are among the most widely used materials. Despite the indirect bandgap and poor optical absorption, silicon is the most common material in the visible and NIR region because silicon photodetectors can easily and inexpensively be fabricated through CMOS processes. Another indirect bandgap material utilized is germanium, where researchers engineer the band diagram of germanium by straining or highly doping. Since those semiconductors and many others can absorb the light and generate photoexcited carriers, they are employed to design and fabricate detectors in various architectures.

Photoconductors are basically semiconductor slabs, where an example is drawn as in Figure 1.3. Incident light significantly changes the number of carriers inside the semiconductor causing a photocurrent to flow. Early HgCdTe detectors were based on photoconductor schemes. Since there is no potential barrier for the majority carriers in

photoconductors, they are usually associated with high dark current levels. The other drawback of photoconductors is that they lack a built-in electric field. Then, relatively higher bias voltages are required to be applied to collect photoexcited carriers before they recombine.

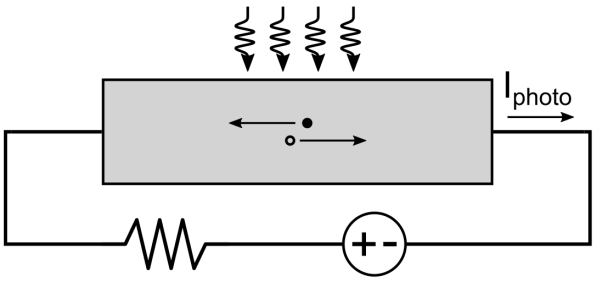


Figure 1.3: An illustration of a photoconductor with reading circuit.

Photovoltaic detectors or **photodiodes** are special diodes based on infrared materials, where a typical photodiode with n-type absorber is schematically shown in Figure 1.4. Depletion region is denoted by W, diffusion lengths for holes and electrons are denoted by L_p and L_n. Hollow circles and filled circles represent photogenerated holes and electrons, respectively. Generated photoexcited carriers diffuse through to the absorbing layer and reach to the depletion region. Then, the strong built-in electric field in the depletion region collects the carriers.

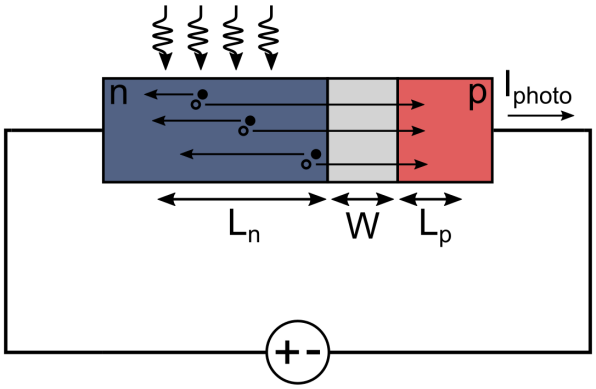


Figure 1.4: An illustration of a photodiode with n-type absorber.

If carefully engineered and fabricated, very low undesired leakage currents are possible in this kind of photodetectors. The built-in electric field inside the depletion

region also removes the requirement for large applied bias voltages. Usually, readout integrated circuits (ROIC) drive the photodiodes under reverse bias voltages of tens of millivolts, where the highest possible photocurrent levels are still achieved. Bulk materials like HgCdTe, InSb, and InGaAs, as well as engineered materials like superlattices, are utilized to design photovoltaic detectors. To create larger potential barriers, it is pretty common to build heterojunctions combining higher bandgap materials with the photon-absorbing regions.

Engineering quantum structures is also an alternative way of detecting infrared photons. In this type of photodetectors, large bandgap materials are usually brought together to create smaller energy level differences. Then, photons interact with carriers bounded in energy levels to create photoexcited carriers.

Quantum Well Infrared Photodetectors are based on energy levels of quantum well constructed with semiconductors, where a typical AlGaAs/GaAs QWIP is presented in Figure 1.5 [8]. A small bandgap material with a thickness of a couple of nanometers is sandwiched between larger bandgap materials. The bandgap difference between the semiconductors constitutes confinement of electrons in the smaller bandgap material, where energy levels are calculated according to Schrödinger's equation. Then, it is possible to arrange quantum well widths so that the energy difference between the confined states or between the confined states and the continuum states corresponds to the energy of infrared photons to be detected.

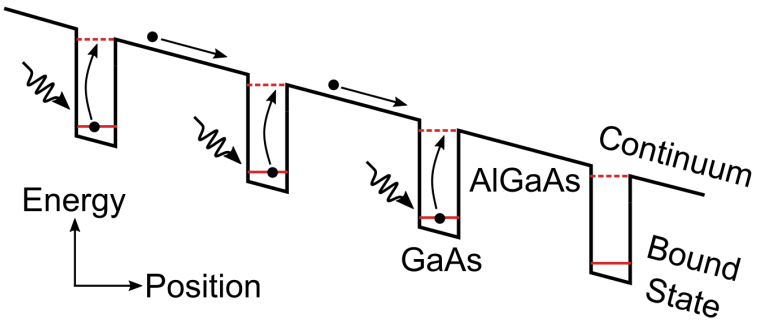


Figure 1.5: Energy band diagram of conduction band of a typical AlGaAs/GaAs QWIP. Adapted and redrawn after [8].

QWIPs are typically made of GaAs/AlGaAs, InP/InGaAs, and AlGaAs/InGaAs material systems, where high-quality materials with great uniformities are relatively easier to grow. On the other hand, the main drawback of QWIP technology is low optical performance because quantum wells can not absorb direct incident radiation. Diffraction gratings, plasmonic resonant structures, or corrugated pixels are utilized to change the polarization of incident radiation so that QWIP can see it, whereas some rare examples can detect direct incident radiation [9]. In addition to low photocurrent levels, QWIPs typically require more cooling to suppress dark current and require ROICs that can provide larger bias voltages.

Type II superlattice (T2SL) detectors also utilize quantum structures, where plentiful semiconductor layers having thicknesses of a couple of nanometers are brought together to build an artificial material. Different from the QWIPs, where wells are strongly separated, T2SL technology is based on the interaction between thin layers of semiconductors. Usually, antimony-containing structures have Type-2 staggered energy band alignment with other semiconductors. Constructing periodic structures containing tiny layers causes the wavefunction of those layers to overlap and create minibands. The energy separation between these minibands, as a typical band structure is presented in Figure 1.6 [10], is employed to detect infrared photons.

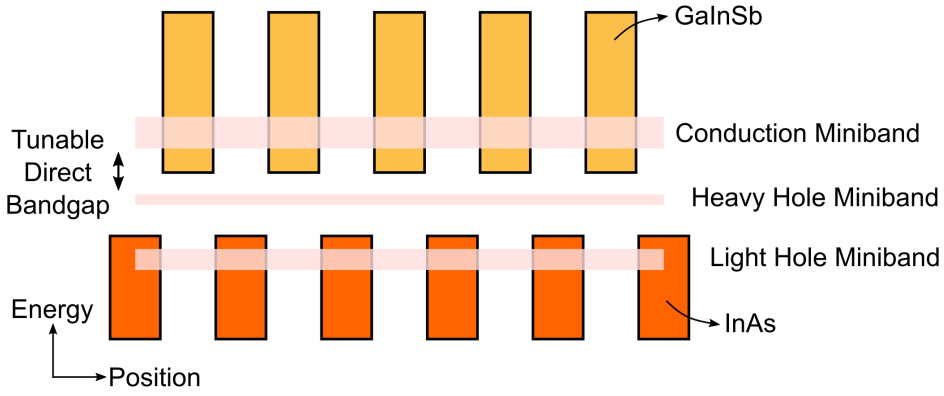


Figure 1.6: Energy band diagram a typical GaInSb/InAs type-II superlattice detector. Adapted and redrawn after [10].

The main advantage of T2SL detectors is that energy levels of minibands can be tailored to cover the infrared region from SWIR to LWIR. On the other hand, opti-

mization of growth conditions for complex epilayer structures containing hundreds of material interfaces is not straightforward. In addition, photosensitivity directly depends on wavefunction overlap in the layers constituting the T2SL, which does not absorb the incident photon as much as bulk materials do.

Pyroelectric Detectors are another type of thermal detectors, where polarization change of materials with respect to temperature is utilized. Similar to the thermopiles, one side of the pyroelectric detector is subject to radiation, generating a temperature gradient inside the pyroelectric crystal. Then, temperature gradient causes a voltage difference to occur between two electrodes of the pyroelectric detector. If the detector receives radiation for a long time, both sides of the detector will heat up and the gradient will be removed. Since pyroelectric detectors is only responsive to temperature gradient, they cannot operate in continuous mode without cooling.

Thermopiles or **Thermocouples**, whose typical schematic drawings are present in Figure 1.7 [11], are one of the detector types that can be classified as thermal detectors. Two different metal alloys are brought together to form a thermocouple, where only one metal is subject to infrared radiation. Infrared energy absorbed by the metal with the help of some absorbing coatings causes the metal heats up. Temperature difference between cold and hot metals of the junction creates a low voltage difference between two metals due to the Seeback Effect. In order to increase the voltage difference, thermocouples are arranged in special configurations and connected in series to construct thermopiles.

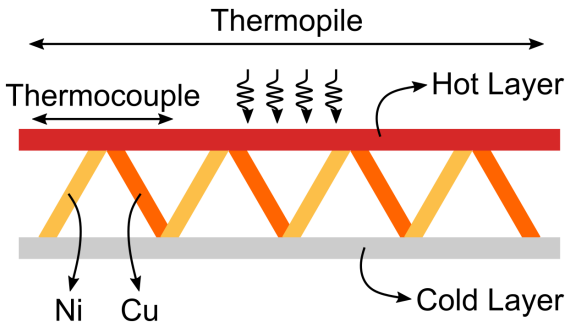


Figure 1.7: A typical thermocouple and thermopile structure. Adapted and redrawn after [11].

Microbolometers are the most widely used examples of thermal detectors, whose typical schematic drawing is present in Figure 1.8 [12]. Microbolometers are suspended bridges with precisely known resistances, where temperature change due to the incident radiation disturbs the resistance of the bridge. Under constant voltage operation, decrease in resistance equivalents to increase in current.

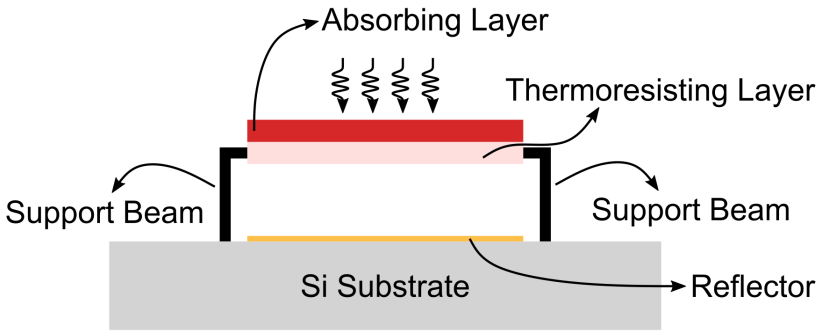


Figure 1.8: A typical microbolometer structure. Redrawn after [12].

To generaly speak about thermal detectors, they are based on much simpler concepts comparing to photon detectors. Therefore, they are inexpensively fabricated and commercially available at considerably low prices. Thermal detectors usually do not require cooling or require coolers just for temperature stabilization near room temperature. On the other hand, neither of thermal detectors can provide high sensitivity, high frame rate and high performance as photon detectors.

1.3 Figure of Merits of Infrared Photodetectors

After mentioning different types of infrared photodetectors, performance metrics of photodetectors will be introduced here.

1.3.1 Responsivity

A good photodetector should detect the radiation effectively. Responsivity is the measure of how effectively a photodetector detects infrared radiation. An electrical signal, either a voltage or a current, should be generated when infrared radiation is incident

to the detector. Responsivity can be estimated as follows:

$$R = \frac{Output\ Signal}{Incident\ Power} = \frac{I_{photo}}{\phi_e} A \tag{1.7}$$

Responsivity is given in A/W when the signal is an electrical current, and incident power is considered in Watts. Most photodetectors do not provide the same responsivity for the entire operating region. Therefore, responsivity is usually given in the form of spectral responsivity. Another parameter related to optical performance is external quantum efficiency, which is the ratio of measured optically generated electrical electron-hole pairs (EHP) to the number of incident photons. It should be noted that, generally, the term "quantum efficiency" is employed instead of external quantum efficiency. When quantum efficiency and responsivity are considered together, it is trivial to see that they are connected parameters. Product of rate of incident photons and energy of incident photons simple gives the incident power:

$$\phi_e = \phi_p \frac{hc}{\lambda} W \tag{1.8}$$

where ϕ_e corresponds to incident infrared energy, ϕ_p corresponds to rate of incident photons, λ corresponds to wavelength of incident photons, h is the Planck's constant, and c is the speed of the light. The photocurrent can be written as follows:

$$I_{photo} = ngq \tag{1.9}$$

where, q represents the elementary charge, n represents the rate of flowing EHP, and g represents the gain if any gain mechanism is present. Then, combining Equations 1.8 and 1.9 yields the quantum efficiency as follows, where gain should be excluded:

$$\eta = \frac{n}{\phi_p} \tag{1.10}$$

Finally, combining Equations 1.7, 1.8, 1.9, and 1.10 relates the quantum efficiency

and the spectral responsivity:

$$R(\lambda) = \frac{nqg}{\phi_p hc}\lambda = \eta g \frac{q\lambda}{hc} \ A/W \tag{1.11}$$

1.3.2 Dark Current

The infrared photodetectors, unfortunately, provides current to the reading circuit without the incident infrared light. This undesired current, which makes detection more difficult and introduces noise, is called dark current. Dark current has different sources depending on the device type and the detector's material system. Usually, the dark current is decreased by cooling the detector. However, depending on the source of the dark current, it might not be straightforward to suppress a particular dark current component by cooling. Therefore, it is critical to design the photodetector so that it provides the lowest dark current. Mechanisms that generate the dark current must be well understood to idealize that vital performance metric.

1.3.3 Noise

Infrared radiation incident to the detector is generally low power, making the noise a crucial figure of merit. Noise mechanisms should be carefully investigated to achieve the lowest possible noise. There are various noise mechanisms, where Johnson noise, generation-recombination noise, shot noise, and 1/f noise will be discussed here.

Johnson (Thermal) Noise originates from the random movement of carriers inside a conducting material. This frequency-independent noise mechanism is active even without any applied bias. Δf being the measurement bandwidth, R is the detector's dynamic resistance, k_b is the Boltzmann constant, and T is the temperature; Johnson Noise current is given as follows:

$$i_{n,Johnson} = \sqrt{\frac{4k_b T \Delta f}{R}} \tag{1.12}$$

Generation Recombination (GR) Noise occurs due to random behavior of gener-

ation or recombination of carriers inside the photodetector. Although there is an equilibrium at the macro level for a time instant, the number of carriers fluctuates. This fluctuation can be due to both optical and thermal generation recombination processes. Random arrival times of photons cause fluctuations in photocurrent while different dark current mechanisms fluctuate the dark current. Δf being the measurement bandwidth, g is the gain, I_{photo} being the photocurrent, and I_{dark} being the dark current; GR noise is given as follows:

$$i_{n,GR} = \sqrt{4q(I_{photo} + I_{dark})g\Delta f} \tag{1.13}$$

Shot (Poisson) Noise is due to the carriers overcoming an energy barrier with random behavior. It can be formulated as follows:

$$i_{n,Shot} = \sqrt{2q(I_{photo} + I_{dark})\Delta f} \tag{1.14}$$

where Δf is the measurement bandwidth, q is the elementary charge, I_{photo} is the photocurrent, and I_{dark} is the dark current.

1/f Noise degrades the detector performance, especially at low frequencies. Although the origin is not clearly shown yet, it is believed to occur due to trap states or other imperfections in the detector.

To conclude the discussion on noise mechanisms of infrared photodetectors, various existing noise mechanisms contribute to the total noise as follows:

$$i_{n,total} = \sqrt{i^2_{n,shot} + i^2_{n,GR} + i^2_{n,Johnson} + i^2_{n,1/f} + \cdots} \tag{1.15}$$

1.3.4 Detectivity and Noise Equivalent Power

Although responsivity provides the measure of how sensitive a detector is to infrared radiation, it does not convey information about the noise performance of the detector. Then, parameters such as noise equivalent power, detectivity, and specific detectivity are introduced to assess the noise level of the detector. The self-explanatory parameter

noise equivalent power (NEP) is defined as infrared radiation power that generates a signal equivalent to the detector's noise level. It is straightforward to express NEP using Equation 1.7.

$$NEP = i_{noise}/R_i \tag{1.16}$$

Detectivity is defined as $D = 1/NEP$, where its dependence on detector area and measurement bandwidth should be avoided to compare detector performances more easily. Normalizing the detectivity with the detector area and the measurement bandwidth yields specific detectivity (D^*) as follows:

$$D^* = \frac{\sqrt{A\Delta f}}{i_{noise}} R_i \tag{1.17}$$

Since infrared detectors are generally used for thermal imaging, it is common to point out the overall optical performance of photodetectors as noise-equivalent temperature difference (NETD). While NETD is a comprehensive measure of optical performance, it is defined considering particular configurations. The f-number of the employed lens system and integration time of the detector should be defined while providing the NETD value. Finally, the NETD value can be described as follows:

$$NETD = \frac{(1 + 4f/\#^2)}{\sqrt{A}\,\sqrt{2\tau}\int_0^\infty T(\lambda)D^*(\lambda)\dfrac{dM_{target}(\lambda)}{dT}d\lambda} \tag{1.18}$$

where $f/\#$ is the f-number of optics, τ is the integration time of the ROIC, $T(\lambda)$ is atmospheric transmission, $M(\lambda)$ is spectral exitance, $D^*(\lambda)$ is specific detectivity, A is the detector area, and T is the temperature. Investigating the NETD equation, it can be seen that increasing the integration time of the ROIC helps to decrease NETD. However, this is a trade-off between a large frame rate. Another trade-off exists in the f-number, where a smaller f-number means heavier and larger lenses.

CHAPTER 2

SWIR/ESWIR PHOTODETECTOR, APPLICATIONS AND STATUS

This chapter presents detailed information regarding shortwave infrared (SWIR) and the extended shortwave infrared (eSWIR) regions. Applications utilizing SWIR/eSWIR, material systems for the development of SWIR/eSWIR photodetectors, and some recent devices from the literature will be discussed in this chapter.

2.1 Applications

Many applications such as earth observation [13], biology imaging [14], gas sensing [15], spectroscopy [16], food safety [17] and internet of things (IoT) [18] utilize infrared radiation up to 2.5 μm to make use of the favorable properties of the SWIR/eSWIR region.

Imaging for night vision and surveillance is one of the leading applications of the SWIR/eSWIR region. As previously presented in Figure 1.1, self-emitting radiation levels are very low in the SWIR band, covering up to 1.7 μm. Therefore, imaging applications use reflecting photons from objects illuminated by other natural or external sources. Shifting the imaging wavelength from the visible to the infrared region provides some advantages regarding scattering and atmospheric transmission. As shown in Figure 1.2, atmospheric attenuation is slightly lower for longer wavelengths than the visible range, yielding a significant superiority for SWIR cameras in distant imaging. In addition, longer wavelengths suffer less from scattering due to haze or smoke, where imagers can provide better pictures than visible imagers in bad weather conditions [19].

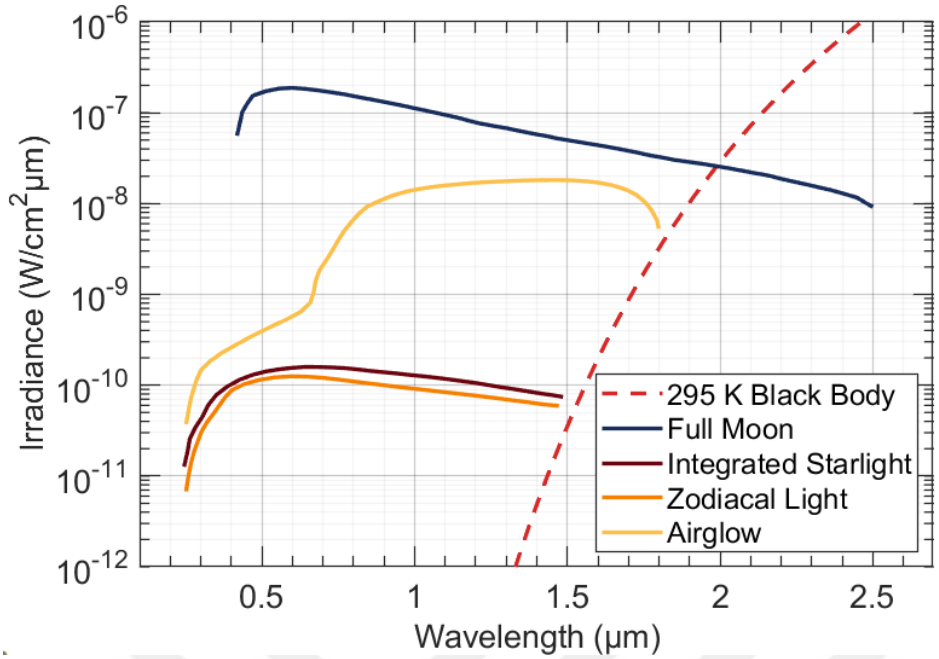


Figure 2.1: Illumination levels of various light sources in the shortwave infrared region. Adapted and redrawn from [20].

The moonlight is the most dominant illumination source at night time compared to other sources as depicted in Figure 2.1 [20]. However, it is still possible to do night vision imaging even at nights without the moon, where radiation due to the night glow might be sufficient. As presented in Figure 2.2, O-H molecules residing in the atmosphere emit radiation [21], making the night glow the most important light source depending on the phase of the moon [22]. On the other hand, the SWIR region covers up the 1.7 μm, without any physical meaning except the cut-off wavelength of high-performance commercial InGaAs photodetectors [23]. The atmosphere is still transparent up to 2.5 μm, and self-emitted radiation from objects becomes a significant photon source. Then, it is pretty logical to extend the cut-off wavelengths of the photodetectors beyond 1.7 μm as many research studies focusing on this aim are conducted. Although various light sources can contribute to night imaging in the SWIR/eSWIR band, the photocurrent density due to all those weak light sources is on the order of nA/cm^2. Therefore, the extremely low level of expected photocurrent requires photodetectors to operate with very low dark currents.

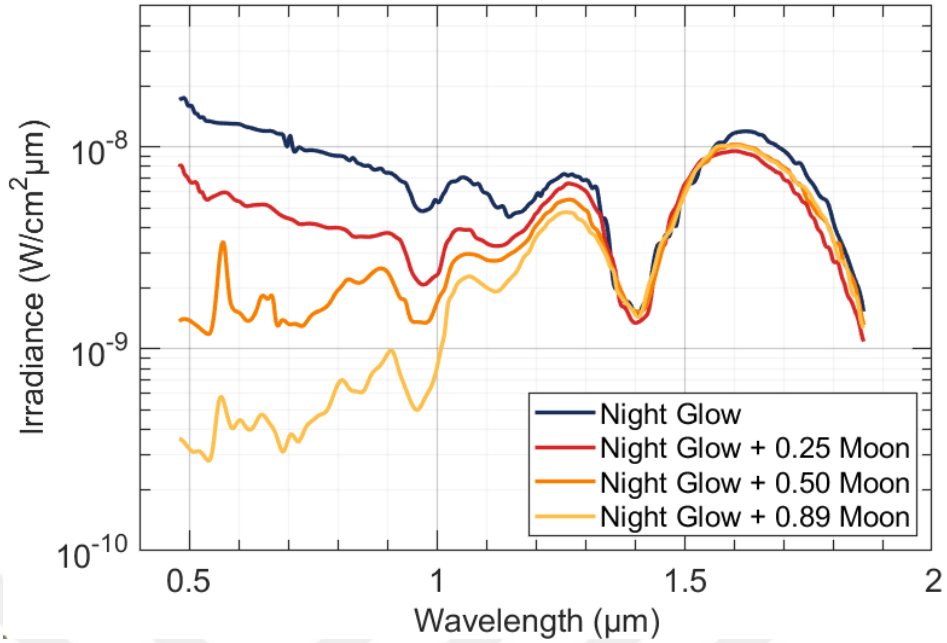


Figure 2.2: Illumination levels due to the night glow with different moon conditions. Adapted and redrawn from [21].

Another application area employing SWIR/eSWIR photodetectors is biological studies such as medicine, food safety, and agriculture. Usage of shortwave wavelengths provides deeper and more detailed images of the eyes, helping physicians to diagnose diseases. In addition to the eye, illuminating wrists or arms reveals high-contrast pictures showing veins, arteries, and bones [24]. Since there is a water absorption near 1.85 μm it is possible to inspect food or agricultural products and pick the rotten ones. Studies on onions revealed the signs of harmful bacteria species [25], and studies regarding peanuts detected fungi contamination [26] by using the SWIR/eSWIR light sources and photodetectors. The water content of the soil also variates and discloses information to the shortwave infrared cameras due to the effect of water content on the reflectance spectrum of the soil.

The shortwave region is also the primary interest of high-speed optical communication since optical fibers provide the lowest dispersion for 1310 *nm* and the lowest optical attenuation for 1550 *nm* [27].

2.2 Material Systems for SWIR/eSWIR Detection

Several material alternatives are possible for detecting shortwave and extended shortwave infrared radiation, and some of them will be discussed in this section.

2.2.1 Mercury Cadmium Telluride (HgCdTe)

HgCdTe is a prevalent infrared material since its bandgap can be adjusted to cover the entire infrared region without considerably changing the lattice constant. The bandgap of the HgCdTe alloy is tailored by adjusting the CdTe mole fraction, as shown in Figure 2.3 [28]. Nearly constant lattice parameter essentially means that an HgCdTe alloy with desired cut-off wavelength can be grown on a suitable substrate without a significant lattice mismatch. Thus, higher quality materials containing low defect densities and long recombination lifetimes are possible. When a high-quality HgCdTe epilayer can be achieved with high-quality CdZnTe substrates, HgCdTe might offer unrivaled performance.

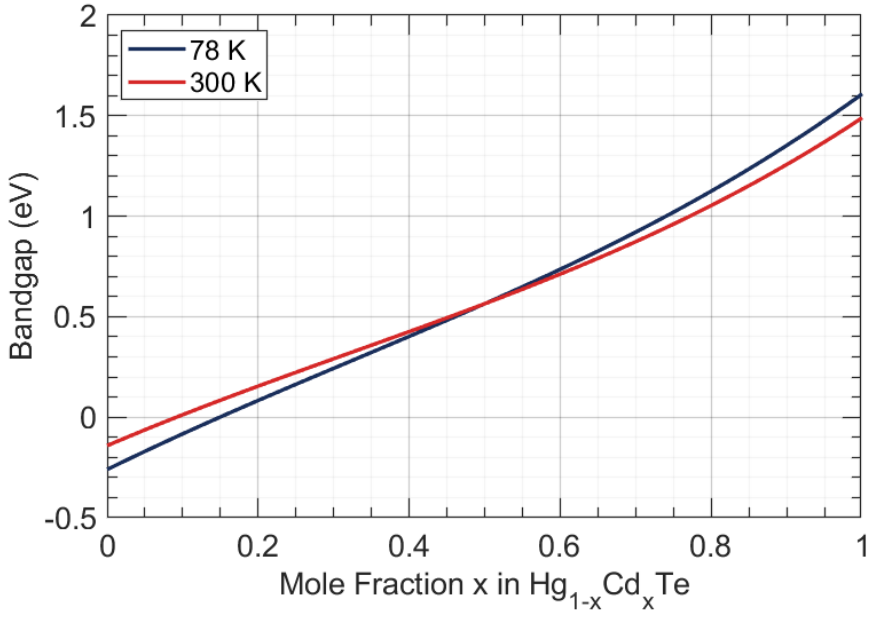


Figure 2.3: Bandgap of HgCdTe vs. CdTe mole fraction at 78 K and 300 K. Adapted and redrawn after [28].

On the other hand, HgCdTe growth is challenging due to the very narrow growth temperature window and low strength Hg-Te bonds, even if the highest quality CdZnTe substrates are employed. In addition, CdZnTe substrates are too expensive, too small, and generally restricted access [29]. Therefore, many studies are conducted by researchers and companies to grow high-quality HgCdTe on alternative substrates like Si, GaAs, GaSb, Ge, or InP [30, 31, 32]. Although promising results appear in the literature, growth uniformity, reproducibility, and yield issues still exist. In addition, to match the performance of InGaAs/InP photodetectors, HgCdTe photodetectors typically require more cooling [33].

2.2.2 Indium Gallium Arsenide (InGaAs)

Indium Gallium Arsenide (InGaAs) is the most common material to fabricate photodetectors operating in the shortwave infrared region. Uncomplicated epilayer growth conditions on high-quality InP substrates, which are widely available for relatively lower prices, and high yield during the fabrication are some of the underlying reasons for that prevalence. InGaAs is a ternary alloy of GaAs and InAs with an adjustable bandgap between 0.354 eV to 1.423 eV at 300 K, depending on the indium mole fraction. Since the binary compounds of InGaAs have a direct bandgap, InGaAs has a direct bandgap in the entire range yielding high absorption coefficients. The bandgap of InGaAs can be estimated using the parameters and models from the literature. Before the InGaAs, bandgaps of InAs and GaAs should be obtained as follows:

$$E_{g,InAs}(T) = 0.417 - \frac{0.276 \times 10^{-3} T^2}{93 + T}\ eV \tag{2.1}$$

$$E_{g,GaAs}(T) = 1.519 - \frac{0.540 \times 10^{-3} T^2}{204 + T}\ eV \tag{2.2}$$

where T is the temperature, and the appearing numbers are empirical Varshni parameters. Then, the relation between the indium mole fraction and the bandgap can be estimated as follows:

$$E_{g,InGaAs}(T) = xE_{g,InAs}(T) + (1 - x)E_{g,GaAs}(T) - 0.477x(1 - x)\ eV \tag{2.3}$$

where x is the indium mole fraction. Finally, assuming 300 K temperature, the Equation 2.3 leads to:

$$E_{g,InGaAs} = 0.354x + 1.423(1 - x) - 0.477x(1 - x)\, eV \tag{2.4}$$

In addition, the lattice constant of the InGaAs can be estimated from temperature dependent lattice parameters of binaries as follows:

$$a_{InAs} = 6.0583 + 2.74 \times 10^{-5}(T - 300)\ \text{Å} \tag{2.5}$$

$$a_{GaAs} = 5.6533 + 3.88 \times 10^{-5}(T - 300)\ \text{Å} \tag{2.6}$$

$$a_{InGaAs} = a_{InAs}x + a_{GaAs}(1 - x)\ \text{Å} \tag{2.7}$$

Considering 300 K, the lattice constant becomes:

$$a_{InGaAs} = 6.0583x + 5.6533(1 - x)\ \text{Å} \tag{2.8}$$

The other important semiconductor in the material system is InAlAs, which is usually employed in optoelectronic devices or transistors together with InGaAs. Bandgap and lattice constant of InAlAs can be modeled similarly with InGaAs. In addition to bandgaps and lattice constants, other properties of the III-V semiconductors can be found in [34]. As the InGaAs/InP material system is outlined in Figure 2.4, InGaAs can be grown lattice-matched to InP with an indium mole fraction of ~ 0.53. This composition yields a bandgap of $\sim 0.74\, eV$, corresponding to a cut-off wavelength of $\sim 1.70\, \mu m$. It should be noted that InAlAs can also be grown lattice-matched to InP with an indium fraction of ~ 0.52.

When the lattice-matched composition of InGaAs is employed to fabricate a photodetector with a cut-off wavelength of 1.70 μm, high quantum efficiency values and room temperature operation can be achieved. Increasing the indium mole fraction makes it possible to cover the extended shortwave infrared region. On the other hand, extending the cut-off wavelength brings a significant lattice mismatch, which causes epilayer quality to decrease significantly. Deterioration in the layer quality results in higher dark current and noise levels [35, 36]. Increased intrinsic carrier concentrations due to the lowered bandgap of InGaAs with high indium concentrations make the situation even worse.

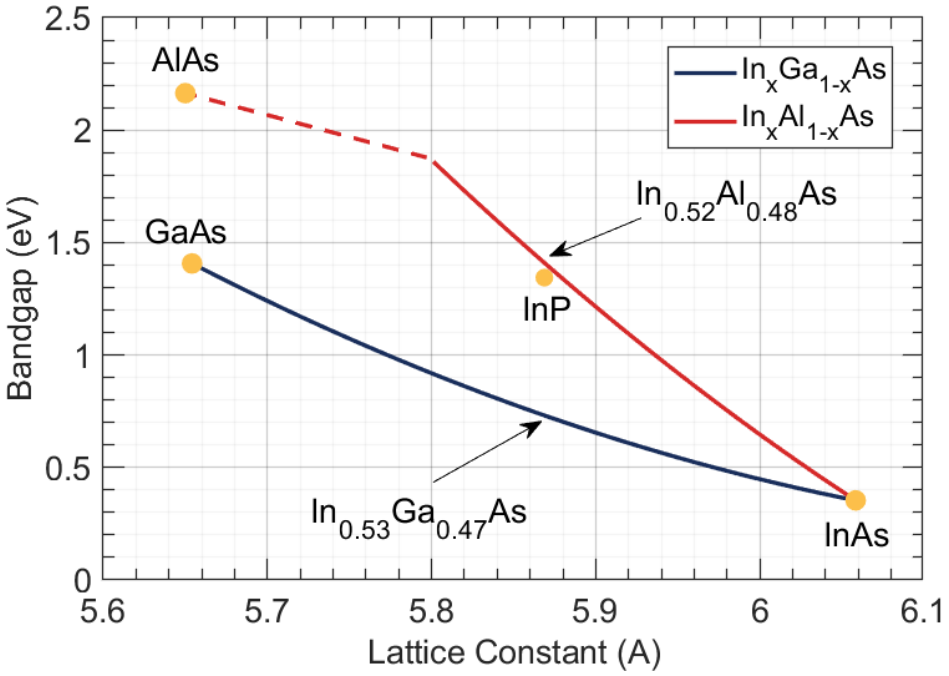


Figure 2.4: Bandgap and lattice constants of semiconductors in the InP material system. Solid lines represent direct bandgaps while dashed lines represent indirect bandgaps. Adapted from [34].

Another and one of the most devastating issues of the InGaAs material systems is the surface instability, where the surface leakage behavior is subject to many research studies. The Fermi level at the surface of the InAs rich compound semiconductors is pinned so that the surface of the device is n-type regardless of bulk doping, where the arsenic vacancy related surface Fermi level pinning behavior is outlined in Figure 2.5 [37, 38, 39]. That surface Fermi level pinning causes highly conductive regions to

build up in the surfaces. Furthermore, in p-InGaAs, the surface is inverted, meaning that an n-type surface channel is present.

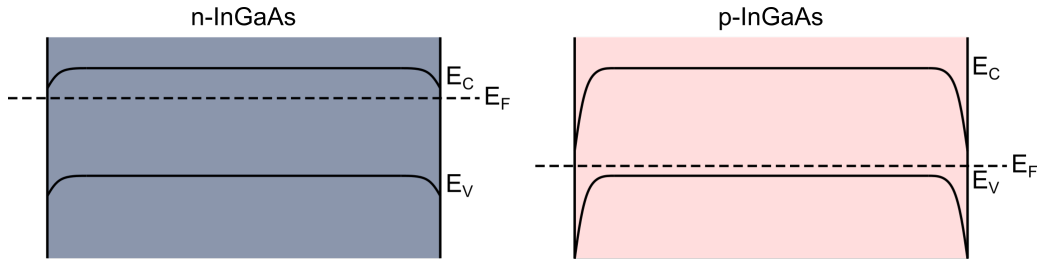


Figure 2.5: Energy band diagrams presenting Fermi level pinning at the surface of InGaAs.

2.2.3 The 6.1 Å Family

Over a decade, the photodetector device architectures based on type-II superlattice (T2SL) materials are frequently reported. The main reason for the popularity of T2SL structures is the flexibility achieved in this material system to cover the infrared region from SWIR to LWIR using various device approaches. Since T2SL materials are grown on GaSb substrates, whose lattice constant is ~6.1 Å, they are also named the 6.1 Å Family. The members of The 6.1 Å Family are outlined in Figure 2.6, where their parameters are obtained using [34].

The thing which makes the 6.1 Å Family special is the type-II broken or staggered band alignments of antimony-containing semiconductors with others, as shown in Figure 2.7 [40]. In other words, if GaSb or InSb is brought together with InAs, the energy bands will align so that the conduction band of the InAs will have lower energy than the valence band of the GaSb. Researchers use this property to design artificial energy bands by combining the family members as hundreds of nanolayers. Then, wavefunctions of adjacent materials constructing the superlattice interact to create minibands for electrons and holes as presented in Figure 1.6. The energy seperation between minibands constitute the optical bandgap, where photons having larger energy than the artificial bandgap can excite carriers to create photocurrent. The artificial bandgap can be adjusted by either changing layer thicknesses or mole fractions of layers forming the T2SL. Although T2SL devices can cover the infrared

region from SWIR to LWIR, devices with cut-off wavelengths longer than 2.5 μm are considered beyond the scope of this thesis.

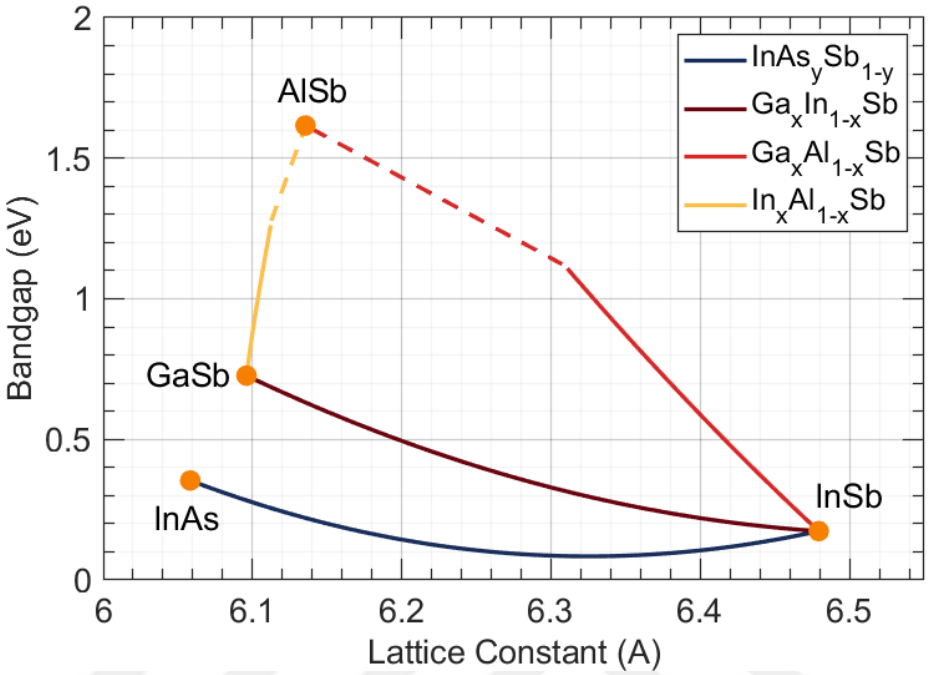


Figure 2.6: Bandgap and lattice constants of semiconductors in the 6.1 Å Family. Solid lines represent direct bandgaps while dashed lines represent indirect bandgaps. Adapted from [34].

T2SL structures can be tailored to detect eSWIR radiation with low dark current values. On the other hand, the optical performances of T2SL detectors in the shortwave infrared region are still under development. The quantum efficiencies are not as high as bulk detectors due to the small overlap of wavefunctions for relatively high energies of the SWIR region. The small overlap of wavefunctions results in low absorption coefficients [41]. In addition, low diffusion lengths make it complicated to increase the optical performance [42]. Growing a thicker absorber region will increase the ratio of total absorbed photons to total incident photons. On the other hand, it is not certain that all photoexcited carriers reach to the contact to contribute the photocurrent. In other words, if the minority diffusion length is too short, making the absorber thicker will not likely increase the optical performance.

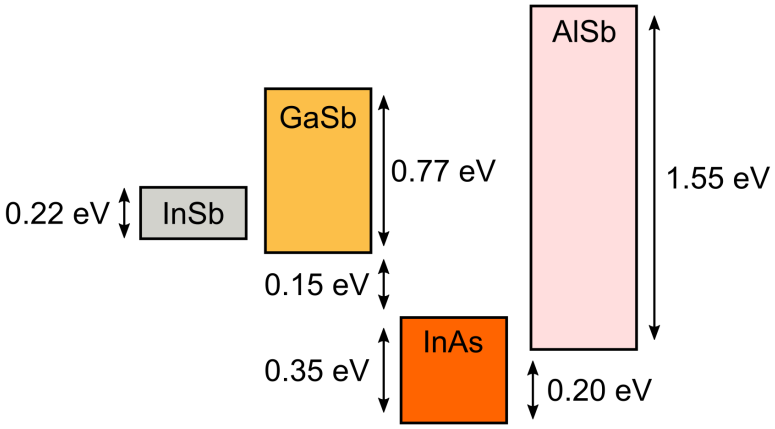


Figure 2.7: Band alignments of semiconductors in the 6.1 Å Family. Boxes represent semiconductors, where bottom edges represent valence band and top edges represent conduction bands. Adapted from [40].

2.3 Recent Examples from the Literature

Selected articles that can be comparable with the study conducted in the scope of this thesis will be briefly summarized here.

A state-of-the-art HgCdTe dual-band detector operating at 2.5 μm and 5.0 μm cut-off wavelengths was manufactured by Teledyne and loaded onto the famous James Webb Space Telescope. Some performance metrics were published, whereas some technical details were not disclosed. The detector grown on CdZnTe substrate yielded $> 80\%$ quantum efficiency, $> 99\%$ pixel operability, and $10^{-2}\ e^-/s$ dark current per pixel at 37 K [43]. Images recently published by NASA were appreciated by scientists and the community.

Klem et al. demonstrated an nBp $In_{0.53}Ga_{0.47}As$ photodiode with a graded InAlGaAs barrier, where the band alignments were adjusted with the help of p-type delta doping [44]. Solid source molecular beam epitaxy (MBE) grown photodiodes exhibited a dark current density of $10 \times 10^{-9}\ A/cm^2$ at 295 K for a $25 \times 25\,\mu m^2$ pixel. Despite the reduced dark current for a mesa device, the contribution of surface current was noted. Quantum efficiency of 50% was reported for incident wavelengths of 1.55 μm.

Çırçır et al. proposed an in-situ passivation technique for the lattice-matched mesa InGaAs photodetectors [45]. A fully depleted p+InP nanolayer was grown between the p-InGaAs contact layer and the n-InGaAs absorber layer. Numerical results were verified with experiments, where nearly an order of improvement in dark current density for various area pixels was reported.

Arslan et al. reported a large format InGaAs FPA [46], where excellent pixel operability of 99.8% was achieved. The 2.5 μm thick unintentionally doped absorber was grown on InP via InAlAs buffer. The detector yielded a peak quantum efficiency of over 90% with a 2.65 μm cut-off wavelength. Pixels yielded $5 \times 10^{-6}\ A/cm^2$ dark current density at -50 mV, and a significant contribution of deep trap centers to the dark current was identified. DLTS studies on extended wavelength InGaAs detectors verified the existence of deep level traps near the intrinsic level [47, 48]. Despite the significant lattice-mismatch between the epilayer and the substrate, no 1/f noise was observed in noise measurements. Thus, specific detectivity of the detector was obtained to be $2 \times 10^{10}\ cm\ \sqrt{Hz}/W$ at room temperature with a possibility for 40 times improvement after cooling to 200 K.

Liu et al. investigated the surface current to bulk current ratio in $In_{0.83}Ga_{0.17}As$ detectors [49]. $In_{0.83}Ga_{0.17}As/In_{0.83}Al_{0.17}As$ photodiode was grown on InP substrate via 2 μm thick InAlAs grading layer and a $In_{0.83}Ga_{0.17}As/In_{0.83}Al_{0.17}As$ digitally graded superlattice. Mesas with different etch depths and various areas were defined using a Cl_2/N_2 reactive ion etching (RIE) recipe. 400 nm SiN_x passivation layer was deposited at low temperature after a short wet etching to eliminate RIE damage and byproducts. At room temperature, $20 \times 20\ \mu m^2$ detector yielded $5 \times 10^{-4}\ A/cm^2$ and $3 \times 10^{-3}\ A/cm^2$ dark current densities for 0.9 μm and 2.6 μm etch depths. The difference reached nearly one order at 200 K, where dark currents of $1 \times 10^{-6}\ A/cm^2$ and $9 \times 10^{-6}\ A/cm^2$ were observed for 0.9 μm and 2.6 μm etch depths, respectively. Arrhenius plots for bulk current yielded 0.41 eV activation energy, while the surface current activation energy was recorded as 0.27 eV. The authors concluded that surface leakage behavior is more important and dominant at lower temperatures.

The lowest dark current in the literature was reported by Ma et al. for mesa-type detectors [50]. $In_{0.83}Ga_{0.17}As$ detector grown on InP substrate via linearly graded

InAlAs buffer region was processed using four etching recipes. The dark current densities of $3.5 \times 10^{-4}\ A/cm^2$ at 300 K and $6 \times 10^{-7}\ A/cm^2$ at 200 K were obtained under -10 mV bias. The etching recipe consisting of SF_6 inductively coupled plasma etching and diluted HCl cleaning yielded those dark current densities with an activation energy of 0.46 eV. The authors finally reported a peak quantum efficiency of 68%.

Ma et al. investigated the noise performance of extended shortwave InGaAs photodetectors, whose epilayers are similar to the studies reported by Liu et al. [49], and Ma et al. [50]. The detectors with cut-off wavelengths of 2.2 μm and 2.5 μm presented bias, temperature and indium mole-fraction dependent 1/f noise characteristic up to the frequency of 1 kHz. The presence of the flicker noise was attributed to the dislocations occuring due to the significant lattice-mismatch between the epilayer and the substrate. At 180 K and for 1 ms of integration time, the detector with 2.5 μm cut-off yielded $6 \times 10^{11}\ cm\sqrt{Hz}/W$ of peak detectivity while the detector with 2.2 μm cut-off yielded $6 \times 10^{12}\ cm\sqrt{Hz}/W$ of detectivity.

Shafir et al. reported an InGaAsSb photodiode lattice-matched to GaSb substrate [41]. 2 μm thick absorber yielded 73% peak quantum efficiency, implying a high absorption coefficient and high diffusion length. The photodiode provided dark current densities of $4.6 \times 10^{-3}\ A/cm^2$ at 300 K and $2.9 \times 10^{-6}\ A/cm^2$ at 200 K under -100 mV bias. Arrhenius plot for the dark current density of the lattice-matched detector showed diffusion limited performance at higher temperatures while a slight deviation from the diffusion line was observed below 240 K. On the other hand, the bandgap of 0.75 eV of GaSb should behave like a filter blocking the incident photons having shorter wavelengths than 1.7 μm. The peak detectivity of $7.5 \times 10^{11}\ cm\sqrt{Hz}/W$ at 200 K was calculated by assuming that the detector is shot noise-dominated, where the accuracy of the assumption would be worth checking.

A comparative study between the mesa and the planar p-i-n structures in InGaAs/-GaAsSb on GaSb was reported by Uliel et al [51]. A peak quantum efficiency of 40% was obtained at room temperature under a bias voltage of higher than -1 V. Cooling the detectors to decrease the dark current also caused a decrease in the quantum efficiency due to the dependence of minority carrier mobility on the temperature. Fabricated mesa and planar detector structures using the same grown wafer yielded sepa-

rated dark current densities with different activation energies. The existence of surface currents was also acknowledged by dark current density measurements conducted on various area pixels. The detectivity value was calculated to be $7.5 \times 10^{11}\ cm\sqrt{Hz}/W$ with the assumption of shot noise dominated characteristic.

Nguyen et al. proposed a combination of InGaAsSb and GaSb absorbers to obtain SWIR/eSWIR dual-band response [52]. The GaSb SWIR absorber was grown after the InGaAsSb eSWIR so that the front illuminated detectors could avoid filtering due to the GaSb substrate. The bias selectable dual-band nBn type detector utilized AlGaSb as the barrier layer. Dark current measurements presented high dark current on the order of $10^{-2}\ A/cm^2$ for both bands, even at cryogenic temperatures. Photoresponse measurements was vaguely disclosed and commented.

Xie et al. combined, for SWIR/eSWIR dual-band operation, $In_{0.53}Ga_{0.47}As$ with $In_{0.53}Ga_{0.47}As/GaAs_{0.50}Sb_{0.50}$ superlattice on InP substrate in npn configuration. The SWIR absorber was grown on top of the eSWIR absorber considering front illumination [53]. Peak quantum efficiencies of 48% and 21% were measured for SWIR and eSWIR detectors, respectively. Spectral crosstalk between subdetectors was calculated to be below -10 dB for a wide range covering up to 1690 nm. The device exhibited room temperature dark current densities of $1.26 \times 10^{-5}\ A/cm^2$ for the SWIR subdetector and $3.78 \times 10^{-2}\ A/cm^2$ for the eSWIR subdetector. Activation energies of 0.50 eV and 0.24 eV were obtained down to 220 K for the SWIR and eSWIR sides, respectively. However, the slope of the activation energy decreased for operation temperatures cooler than 220 K. Assuming shot noise-dominated noise performance, room temperature peak detectivities of $2 \times 10^{11}\ cm\sqrt{Hz}/W$ and $2 \times 10^{9}\ cm\sqrt{Hz}/W$ was calculated for SWIR and eSWIR subdetectors, respectively.

CHAPTER 3

DESIGN, FABRICATION AND CHARACTERIZATION OF A DUAL-BAND INGAAS NBN PHOTODETECTOR

This chapter discusses barrier and nBn photodetectors at first. Then, it presents the design, the fabrication, and the characterization of an nBn type SWIR/eSWIR dual-band InGaAs photodetector. In the design section, the dependencies of performance metrics on device parameters, and approaches to improve the detector performance will be explained in detail. Then, the realization of designed detectors will be presented, starting from material growth to fabrication steps. Characterization results will be reported and rigorously discussed.

3.1 Properties and Advantages of Barrier Photodetectors

Most of the common photodetectors are based on architectures of pn junctions, as some of the recent ones were cited in Chapter 2. Typically, photodiodes can provide high quantum efficiencies and low dark currents if they are carefully designed, fabricated, and sufficiently cooled. On the other hand, there is still room for improvement in their dark current performances to achieve higher operating temperatures or lower dark current at the same operating temperatures. To engineer the dark currents of pn junctions, the origins of the leakage current should be well understood.

3.1.1 Dark Current Components in pn Junctions

There are a couple of main dark current mechanisms in a pn junction diode, including diffusion current, generation-recombination current, tunneling currents, and surface

leakage, as illustrated in Figure 3.1 [54].

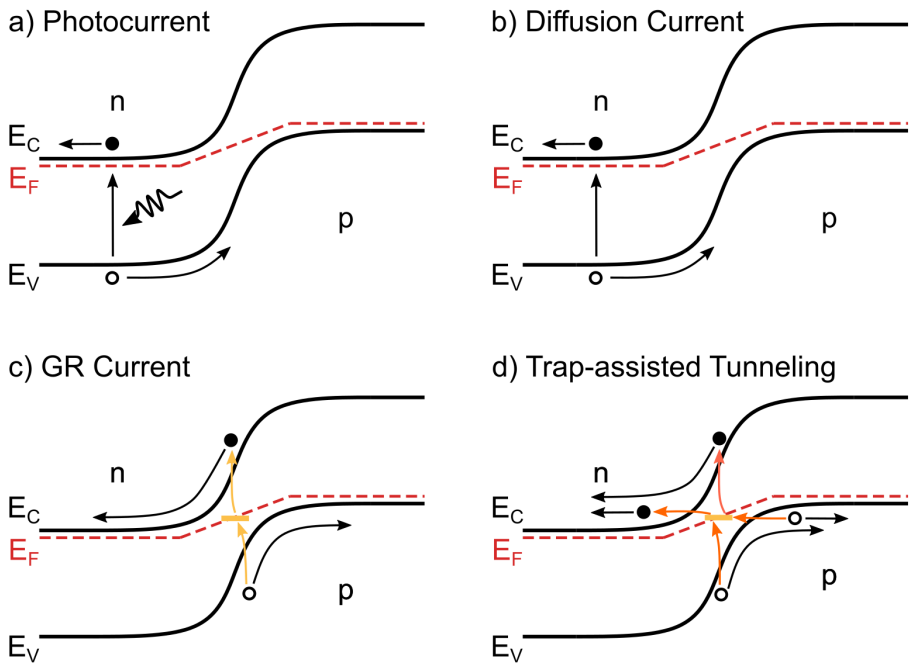


Figure 3.1: Illustration of various current sources in pn junctions using energy band diagrams. (a) Photocurrent, (b) diffusion current, (c) generation-recombination current (c), and (d) trap-assisted tunneling are presented. Adapted and redrawn after [54].

The diffusion current is the reverse bias saturation current of a pn junction, which is generated due to the thermally generated carriers in the vicinity of the depletion region. Carriers generated closer than the diffusion length can diffuse through the depletion region, leading to a dark current. The diffusion current is expressed as follows:

$$I_{diff} = qA\left(\frac{L_p}{\tau_p}\frac{n_i^2}{N_D} + \frac{L_n}{\tau_n}\frac{n_i^2}{N_A}\right)\left(e^{qV/kT} - 1\right) \tag{3.1}$$

where q is the elementary charge, A is the junction area, n_i is the intrinsic density, L_p and L_n are the diffusion length of holes and electrons, τ_p and τ_n are the lifetimes of holes and electrons, N_A and N_D are the acceptor and donor densities.

Another dark current component is generation recombination (GR) current, origi-

nating from generation recombination centers inside the depletion region. The GR current is also named Shockley-Read-Hall (SRH) current. Unfortunately, in most cases, it is not possible to have a perfect semiconductor crystal structure. There exist crystal defects such as vacancies, interstitial sites, and dislocations depending on the material quality. The crystal defects behave as traps allowing carriers to recombine or generate through these centers.

The SRH recombination rate, R_{SRH}, is expressed as follows:

$$R_{SRH} = \frac{np - n_i^2}{\tau_p(n + n_1) + \tau_n(p + p_1)} \tag{3.2}$$

where τ_p and τ_n are the SRH lifetimes of holes and electrons, p and n are hole and electron densities. p_1 and n_1 are the hole and electron parameters that explain the dependencies of recombination rate on the energy level of trap centers, where their mathematical expressions are given as follows:

$$p_1 = N_v e^{\frac{E_v - E_t}{k_b T}} \tag{3.3}$$

$$n_1 = N_c e^{\frac{E_t - E_c}{k_b T}} \tag{3.4}$$

In Equations 3.3 and 3.4, N_c and N_v denote conduction and valence band effective density of states, E_c and E_v denote conduction and valence band energy levels, and E_t represents the energy level of the trap. Assuming $E_t = E_i$, $\tau_n = \tau_p = \tau_{SRH}$, and totally depleted carriers inside the depletion region, Equations 3.3, 3.4, and 3.5 can be combined to obtain GR current as follows:

$$I_{GR} = qAW\frac{n_i}{2\tau}\left(e^{qV/2kT} - 1\right) \tag{3.5}$$

where q is the elementary charge, A is the junction area, and W is the depletion width. When Equations 3.1 and 3.5 are compared, it is straightforward to see that the dependency of the GR current on temperature is less than that of the diffusion current. Therefore, the diffusion current will decay rapidly with cooling, leaving the

detector GR current dominated. Alternatively, to suppress GR current, cooling to lower temperatures will be required.

Even if the detector is cooled down to cryogenic temperatures, tunneling dark current components will be resistant to decrease. Tunneling occurs in two mechanisms: Band to band tunneling (BtB) and trap-assisted tunneling (TAT). At higher doping densities, the junction's p and n sides are separated in energy. That separation causes the valence band of the p side to align with the conduction band of the n side. Then, carriers tunnel through to the junction leading to an undesired dark current contribution. When traps are present inside the depletion region, the tunneling process becomes easier with the help of traps, causing trap-assisted tunneling. Tunneling mechanisms should be strictly avoided to obtain the ultimate detector performance.

3.1.2 Unipolar Barrier Photodiodes

Placing unipolar barriers is one of the relatively recent ideas to suppress dark current mechanisms in photodiodes. Barriers filter the dark current mechanisms according to their spatial origins. If carefully designed and correctly inserted inside the device, a unipolar barrier can suppress tunneling, SRH, and surface currents, as schematically illustrated in Figure 3.2a. On the other hand, placing the same barrier on the p-side instead of the n-side as in Figure 3.2b will not affect the dark tunneling and SRH currents [54, 55].

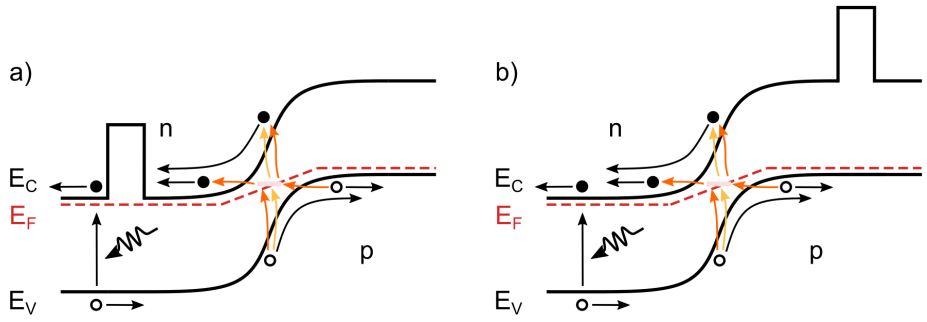


Figure 3.2: (a) Illustration of filtering achieved by unipolar barrier placed on the n-side, (b) on the p-side. Adapted and redrawn after [54,55].

3.1.3 nBn Photodetectors

Although unipolar barrier structures in photodiodes help filter the dark current components, tunneling and SRH still arise due to the existence of the depletion region. Then, those dark current components would be completely eliminated if the depletion region is avoided. Therefore, the nBn architecture is offered to design photodetectors free of a depletion region. A high bandgap material is sandwiched between the n-type absorber and contact regions to block the flow of the dark current while allowing the unimpeded flow of the photogenerated carriers, as illustrated in Figure 3.3. nBn devices can be described as photoconductors with unity gain, which makes them hybrid devices between photovoltaic detectors and photoconductors [56].

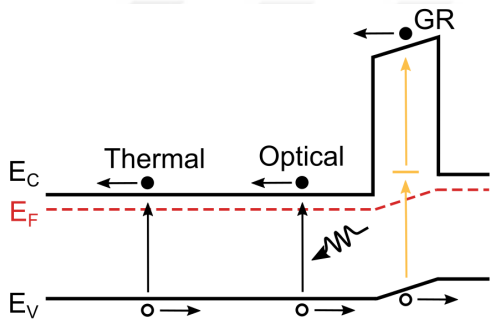


Figure 3.3: Illustration of flow of photocurrent and dark current components in an nBn photodetector. Adapted and redrawn after [56].

Since no depletion region exists in the nBn devices, the electric field inside the structure is strictly decreased. The existing electric fields are designed to lie inside the high bandgap barrier region, where intrinsic carrier density is too low compared to the absorber region. Therefore, the SRH rate decreases to insignificant levels making the devices diffusion current dominated even in low lifetime materials. In addition to the lowered electric fields, barriers can be thick enough to prevent tunneling mechanisms completely. Since the high energy offset in the conduction band blocks the flow of the majority carriers, it also blocks the flow of the surface currents in material systems where the surface is n-type [57].

On the other hand, finding an ideal barrier is not a straightforward task. An ideal barrier for an nBn detector must have the zero valence band offset while maximizing the

conduction band offset. Then, it only blocks the flow of the electrons contributing to the dark current. Otherwise, any offset in the valence band will drastically remove the photoresponse. Because the T2SL structures tailored in the 6.1 Å family provide the most flexible options, it is pretty common to exploit this material system to construct nBn photodetectors [58, 59, 60, 61, 62].

Finally, the comparison between the nBn detector and the unipolar photodiode regarding the filtering of dark currents is illustrated in Figure 3.4. If all barriers in the unipolar photodiode are assumed to be missing, the dark current will be equivalent to an ordinary pn junction detector, where the superiority of the nBn detector over the pn junction can be explicitly deduced [56].

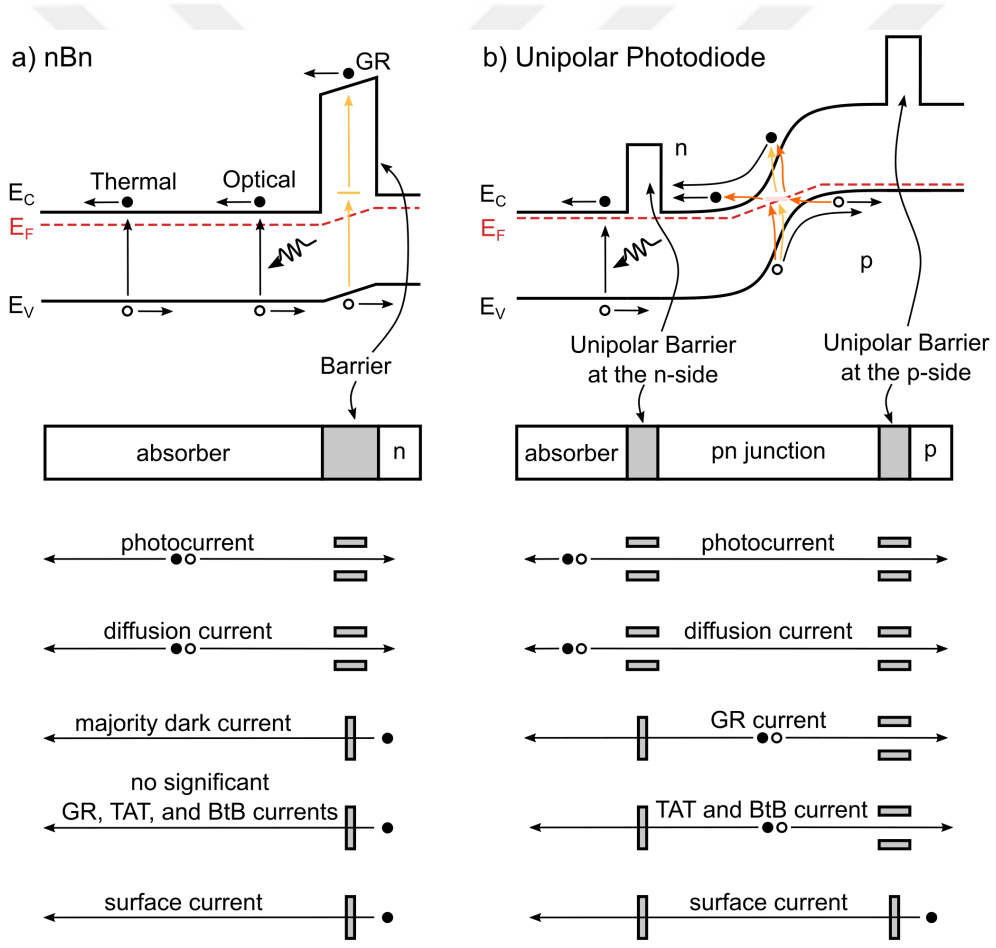


Figure 3.4: (a) Comparison of the flow of photocurrent and dark current components in an nBn photodetector, (b) and in a unipolar photodiode. Adapted and redrawn after [54,55,56].

If a pn junction and an nBn detector were made of the same material system assuming all the same physical parameters, the dark current characteristic of both devices would be as depicted in Figure 3.5. Two crucial outcomes can be inferred from Figure 3.5: The nBn detector can operate at higher temperatures with the same dark current, or the nBn detector can operate at the same temperature with a lower dark current.

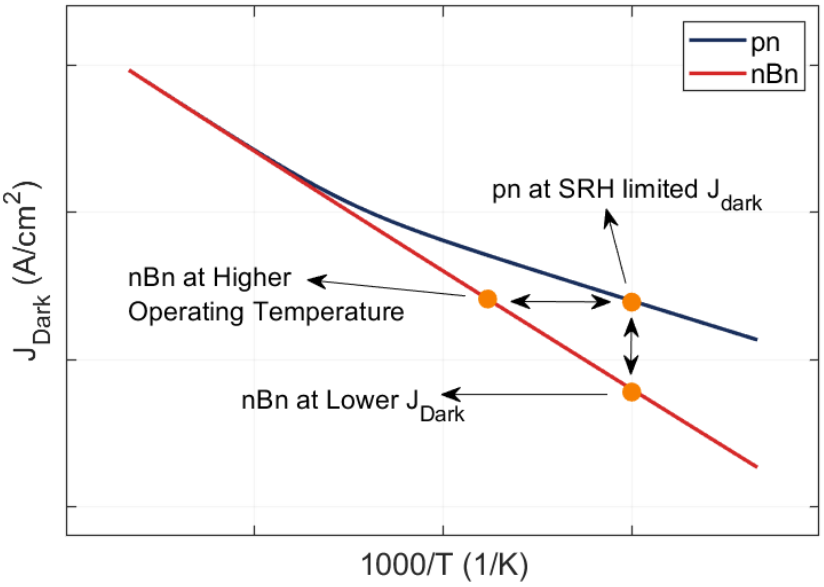


Figure 3.5: Comparison of the Arrhenius plots of an nBn photodetector and a photodiode. Adapted and redrawn after [56].

3.2 Design

During the design progress, a commercial simulation software, Synopsis Sentaurus TCAD, was utilized. This software has the ability to simulate various semiconductor devices including transistors, diodes, photodetectors, light emitting diodes, etc. Once the device is defined, Sentaurus seeks an initial solution to the electrostatic potential inside the device using Poisson's equation as given in Equation 3.6:

$$\nabla \cdot (\varepsilon \nabla \phi + \vec{P}) = -q(p - n + N_D - N_A) - \rho_{trap} \tag{3.6}$$

where ε is electrical permittivity of the medium, $\vec{P}$ is polarization vector, q is the

elementary charge, n is the electron density, p is the hole density, N_A is the concentration of ionized acceptors, N_D is the concentration of ionized donors, and ρ_{trap} is the charge density of traps or fixed charges. To compute the behavior of the device, then, Sentaurus uses hole and electron continuity equations as follows:

$$\nabla \cdot \vec{J_n} = qR_{net,n} + q\frac{\partial n}{\partial t} \tag{3.7}$$

$$\nabla \cdot \vec{J_p} = -qR_{net,p} + q\frac{\partial p}{\partial t} \tag{3.8}$$

where $R_{net,n}$ is the net electron recombination rate, $R_{net,p}$ is the net hole recombination rate, $\vec{J_n}$ is the electron current density, $\vec{J_p}$ is the hole current density, n is the electron density, and p is the hole density. When the Drift-Diffusion carrier model is employed for the carrier transport, the current equations simplify as follows:

$$\vec{J_n} = nq\mu_n \nabla \Phi_n \tag{3.9}$$

$$\vec{J_p} = -nq\mu_p \nabla \Phi_p \tag{3.10}$$

where Φ_n is quasi-Fermi potential for electrons, Φ_p is quasi-Fermi potential for holes, μ is the mobility of the corresponding carrier [63].

Depending on the application, various physical models can be included or excluded in the Sentaurus simulations. SRH recombination, tunneling, Auger recombination, radiative recombination, and surface recombination models were included in the simulations since the scope of this thesis considers the design of an InGaAs photodetector.

Dealing with the InGaAs/InP material system, where a lattice-mismatch was also introduced to cover extended wavelengths, requires modeling of the SRH recombination. This requirement occurs because relatively high trap densities are observed at lower bandgap regions when InGaAs is grown with higher indium mole fractions. As a result, extended shortwave InGaAs infrared detectors usually operate SRH-dominated. Sentaurus calculates the recombination rates using the Equations 3.2, 3.3 and 3.4 with user-specified trap and lifetime parameters.

In the depletion regions of the pn junctions, the carriers tend to tunnel through to the junction because of the large built-in electric fields. Furthermore, electrically active traps promote tunneling causing trap-assisted tunneling (TAT). Sentaurus treats the tunneling mechanisms using the Hurkx model, which modifies the SRH recombination lifetime considering the electric field, trap energy, and a parameter called carrier tunneling effective mass [64]. Carrier tunneling effective mass is a measure of how carriers are likely to contribute to tunneling action, where smaller effective mass means higher tunneling rates. After modification due to the Hurkx model is included, SRH recombination lifetime becomes:

$$\tau = \frac{\tau_{SRH}}{(1 + \Gamma)} \tag{3.11}$$

where Γ is the tunneling enhancement factor. Derivation of the Γ, which can be found in [64], is considered beyond the scope of this thesis.

Structures considered in this optimization study include some highly doped regions. Moreover, the optical excitation of semiconductors increases the carrier densities, causing Auger recombination to play an important role. Sentaurus considers Auger recombination as follows:

$$R_{auger} = (C_n n + C_p p)(np - n_i^2) \tag{3.12}$$

where C_n and C_p are the Auger constants, n and p are the carrier concentrations, and n_i is the intrinsic concentration.

In addition to the Auger recombination, the direct bandgap structure of the InGaAs material makes radiative recombination important in regions with high carrier densities. Radiative recombination is included in the Sentaurus as follows:

$$R_{rad} = C(np - n_i^2) \tag{3.13}$$

where C is the radiative recombination constant, n and p are the carrier concentrations, and n_i is the intrinsic concentration.

Surfaces of InGaAs devices are problematic, and passivation is quite challenging. Typically high surface recombination velocities make the surface recombination significantly affect the overall device characteristic. Furthermore, the surface Fermi level of the InGaAs is always pinned to a level so that surface is n-type regardless of bulk doping. Then, surface recombination is considered in Sentaurus as follows:

$$R_{surf} = \frac{np - n_i^2}{(n + n_1)/s_p + (p + p_1)/s_n} \tag{3.14}$$

where s_n and s_p are hole and electron surface recombination velocities, and p_1 and n_1 are calculated as in Equations 3.4 and 3.3 considering the energy level of the surface traps.

Finally, to move to the design phase, simulation parameters were meticulously compiled from the literature as presented in Table 3.1 with their explanations and numerical values.

Table 3.1: Simulation parameters

	Parameter	Value
τ	SRH Recombination Lifetime [65]	20 ns
C	Auger Recombination Coefficient [66]	$1.8 \times 10^{-28} cm^{-6}/s$
S_0	Surface Recombination Velocity [67]	10^4 cm/s
m_{trap}	TAT Effective Mass [68, 69]	0.03 m_0
	Acceptor Trap for e-SWIR Regions [47]	
E_{a1}	Activation Energy	$E_v + 0.31$ eV
N_{t1}	Trap Density	1.5×10^{15} cm^{-3}
σ_1	Capture Cross Section	5.31×10^{-16} cm^2
	Donor Trap for SWIR Regions [47]	
E_{a1}	Activation Energy	$E_c - 0.33$ eV
N_{t1}	Trap Density	1.5×10^{14} cm^{-3}
σ_1	Capture Cross Section	4.74×10^{-16} cm^2

3.2.1 InGaAs nBn Photodetector at 2.2 µm

Since nBn photodetectors have advantages over other photodetector types, an nBn type photodetector with dual-band capability was designed in the scope of this thesis. A single-band photodetector operating at 2.2 μm was selected as the starting point of the final design.

nBn detectors appearing in the literature are generally based on T2SL materials because engineering flexibility decreases when bulk materials are selected. An nBn detector requires a barrier that only hinders the flow of the majority carriers simultaneously, allowing the unimpeded flow of the photogenerated minority carriers. Even a minimal energy barrier in the valence band drastically disturbs the quantum efficiency. Finding such a barrier is not easy in bulk materials like InGaAs or HgCdTe.

In this design study, quaternary alloy InAlGaAs was employed as the barrier, where band offset estimations at the $In_{0.52}Al_{0.48}As/In_{0.53}Ga_{0.47}As$ interface agree that conduction band offset takes 70% ± 6% of the total energy bandgap difference [70, 71, 72]. It should be noted that these studies estimate the band offsets assuming zero doping density by subtracting the effect of doping [70]. In addition, a study regarding band alignments of InAlGaAs/InGaAs at lattice matched compositions to InP substrates also agrees with the $In_{0.52}Al_{0.48}As/In_{0.53}Ga_{0.47}As$ cases [73]. Thus, considering the previous studies, the energy bandgap difference between the InAlGaAs barrier region and InGaAs regions was distributed to the valence and conduction band so that the conduction band takes 64% of the energy band difference. The energy band diagram with zero doping for our structure was shown in Figure 3.6a. Simulated band diagram agreed with the literature, and band offsets (~64%) corresponded to the largest valence band offset [70, 71, 73], making our approach accounts for the worst case for optical performance. After applying the doping levels associated with the designed epilayer structure except the delta doping, the bands aligned as shown in Figure 3.6b. The resulting structure, obviously, was not suitable for collecting minority carriers required for a high photoresponse. Then, the issue with the valence band offset was nullified by using a p-type delta doping, which was relatively recently proposed in the literature [74, 75, 76, 44]. Also, the delta doping layer made the conduction band offset larger, improving the dark current performance. The resulting

energy band diagram was obtained as discussed below and as depicted in Figure 3.8.

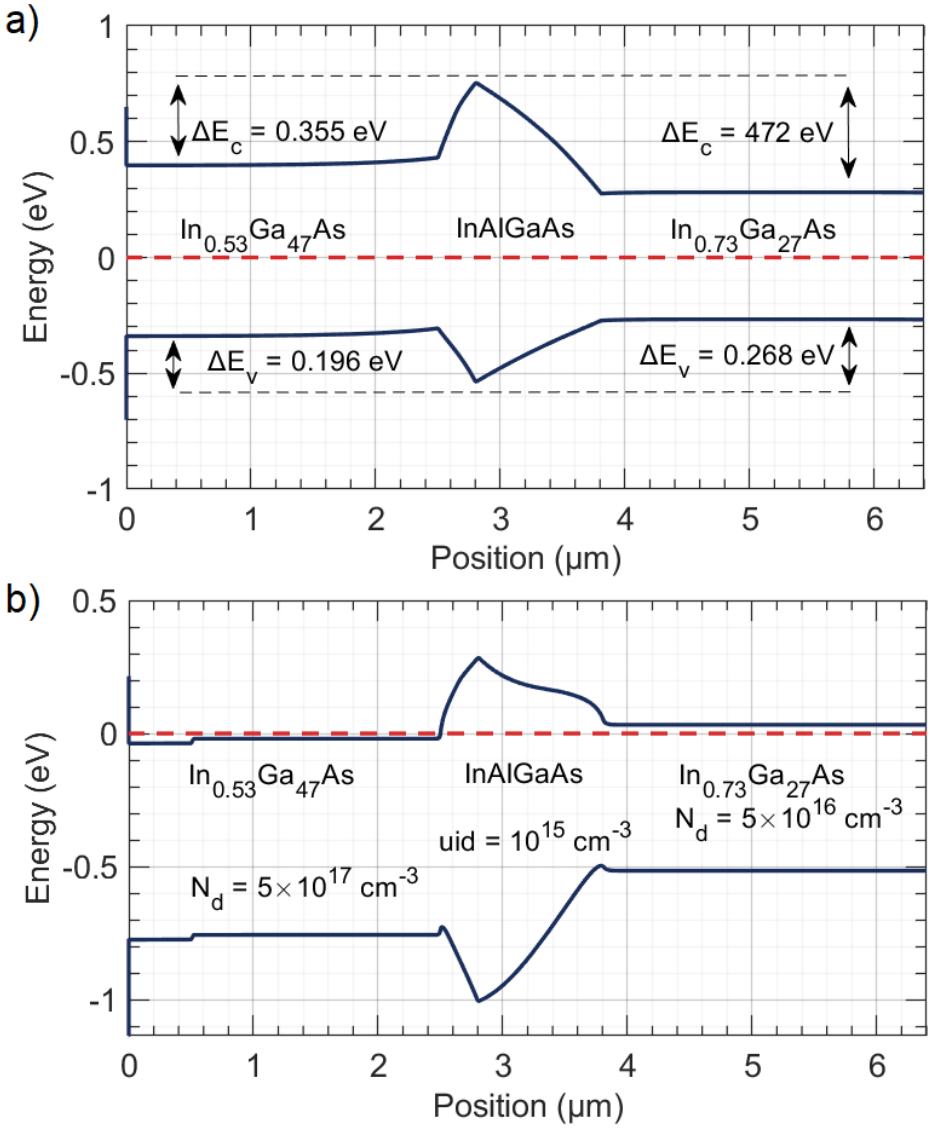


Figure 3.6: (a) Simulated band alignments between InGaAs and graded InAlGaAs assuming no doping, (b) assuming doping levels except the delta doping.

Using the simulation parameters given in Table 3.1, an nBn structures, whose epilayer was given in Figure 3.7, was considered. A short buffer layer of $In_{0.53}Ga_{0.47}As$ was designed on top of the InP substrate with lattice matching condition. Then by slowly variating Al/Ga ratio, the InAlGaAs barrier region was placed on the buffer region without changing the lattice constant until the highest Al/Ga ratio was reached. After the delta doping region, lattice mismatch was introduced. Metamorphic InGaAs absorber with the cut-off wavelength of 2.2 μm ended the structure. While the InAl-

GaAs regions were left unintentionally doped, the buffer layer and the absorber layer were n-type doped with a concentration of $N_d = 10^{18}\ cm^{-3}$ and $N_d = 5 \times 10^{16}\ cm^{-3}$, respectively.

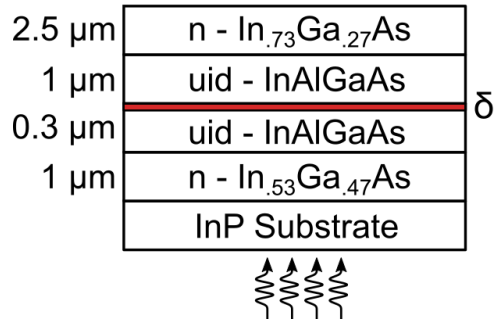


Figure 3.7: Epilayer of the proposed nBn structure.

Band diagrams of the structure were obtained first. As shown in the Figure 3.8, placing delta doped region inside the barrier effectively removed the valence band offset. When alignment of valence bands of the contact layer and the absorber layer was investigated in Figure 3.8a, that misalignment occurred due to the bandgap differences between that two layers. As in Figure 3.8b, a driving voltage of 240 mV removed the misalignment that hinders the flow of the photogenerated holes. As a result, the operating voltage of the nBn detector was selected to be $\sim 300\ mV$.

Since the profile of the delta doping layer has a crucial effect on band diagrams and the device performance, delta profiles with various thicknesses and densities were analyzed. Dark current and optical current performances obtained in simulations were presented in Figure 3.9a and Figure 3.9b. It was found that the device performance depends on the sheet doping density, which is the product of delta layer thickness and the doping density. Sheet doping density of $N_\delta = 2 \cdot 10^{11}\ cm^{-2}$ was observed to be the optimum delta doping dose that completely removes the valence band offset. Lower doping doses than the optimum values caused valence band offset, resulting in low photocurrent. Since the delta doping layer also helps to increase the conduction barrier height, lower delta doping densities than the optimum ended up with lower barrier height and higher dark current.

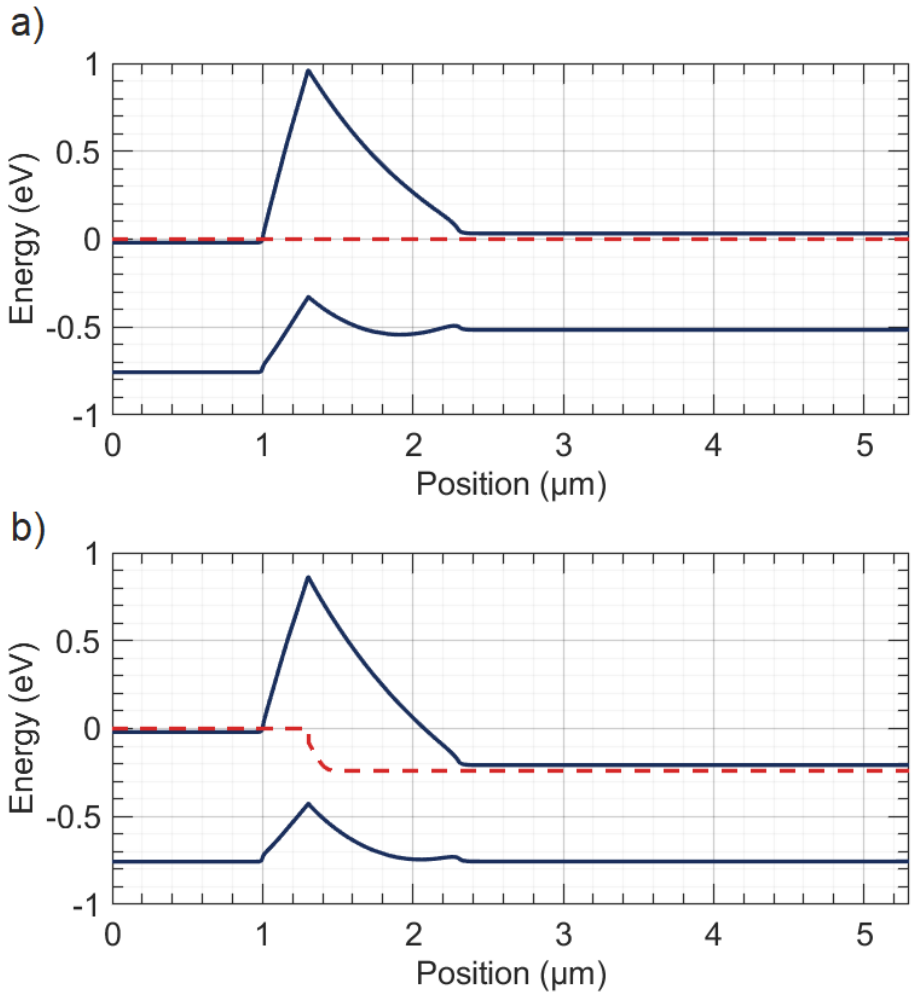


Figure 3.8: (a) Simulated band diagrams of the nBn photodetector at bias voltages of 0 mV, (b) and 240 mV. Solid lines represent conduction and valence bands while dashed lines represent quasi-Fermi levels.

On the other hand, increasing the delta doping dose beyond the optimum point led to an insignificant effect on device performance. Therefore, a delta doping sheet density of $N_\delta = 3.5 \cdot 10^{11}\ cm^{-2}$, slightly higher than the optimum, was selected as the final design parameter considering any deviation that might occur during the epitaxial growth.

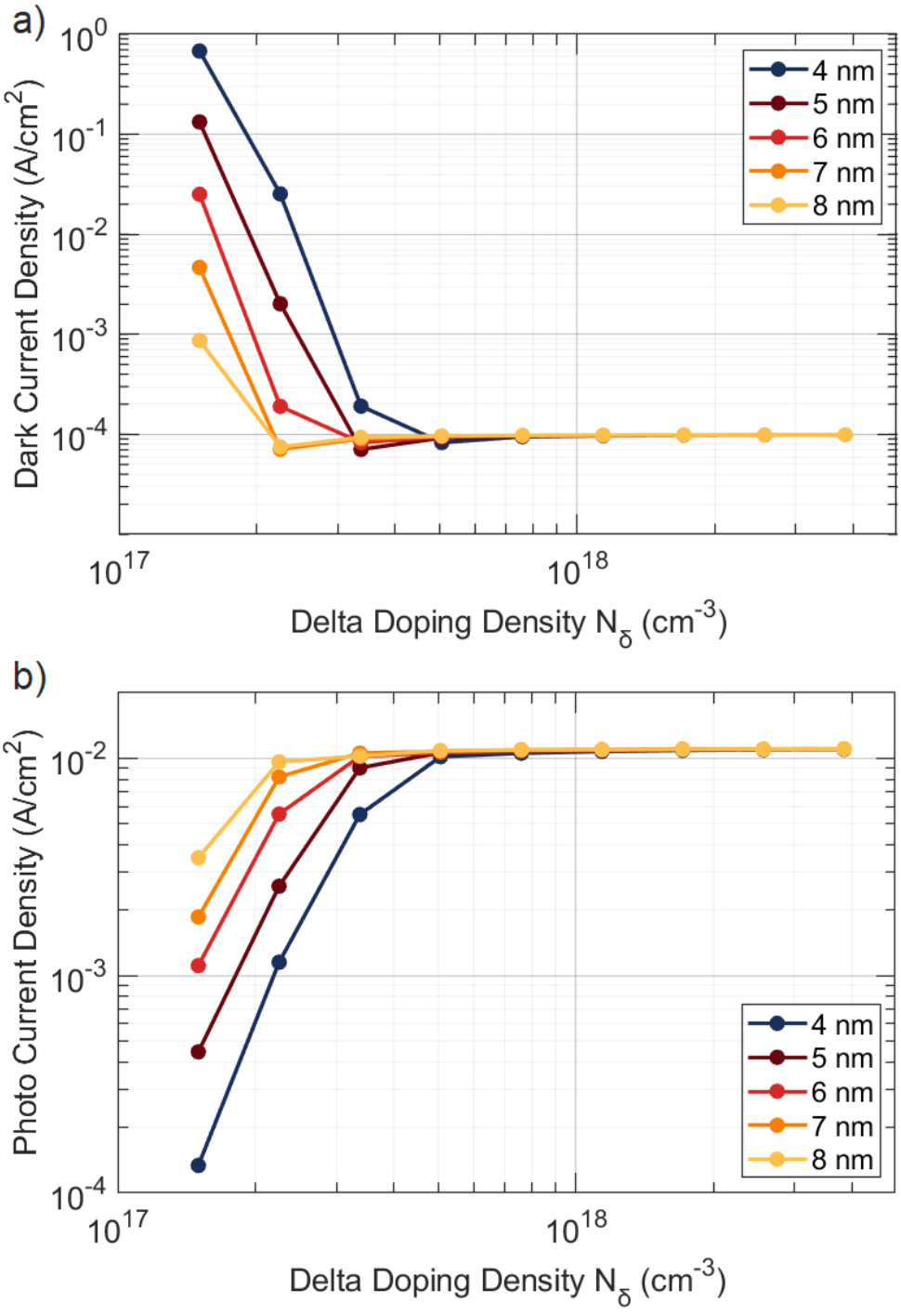


Figure 3.9: (a) Dark current values, and (b) photocurrent values at delta doping profiles with various thicknesses and doping densities.

Although alternative device architectures can be found in the literature, photovoltaic detectors are still the most common type and present high performance. Thus, a photovoltaic alternative, whose epilayer was presented in Figure 3.10, was also designed in addition to the nBn photodetector designed in this study. To ensure a fair comparison, both architectures were simulated using the same physical parameters, and both designs were optimized to provide their ultimate performance. In the pn junction, lattice mismatch was directly introduced in the metamorphic buffer layer as in the examples from the literature [46, 77, 78]. The n-InGaAs absorber region was followed by the p-InAlAs barrier and the p-InGaAs contact region. Absorber doping concentration was selected the same with the nBn, while p-type regions were doped with a concentration of $N_a = 10^{18}\ cm^{-3}$.

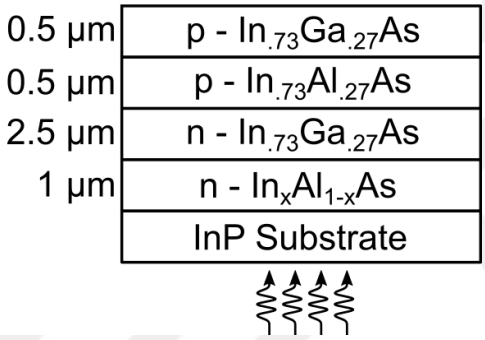


Figure 3.10: Epilayer of the pn structure.

When the dark currents of the two structures were compared, the nBn structure provided a significant improvement in dark current as shown in Figure 3.11 The reason why nBn provided lower dark current was inspected. This nBn structure was designed so that the electric field due to compositional grading of the barrier compensates the electric field due to the delta doping layer. Thus, built-in electric field inside the nBn structure was significantly lower than pn junction, as seen in Figure 3.12. In addition, the built-in electric field was placed inside the high bandgap barrier region, where intrinsic carrier concentration is much lower than the absorber region. The arrangements regarding the electric field resulted in a decreased SRH rate as shown in Figure 3.13. Reduced SRH rates was expected to decrease the ideality factor of the device in addition to the decrease of dark current at room temperature.

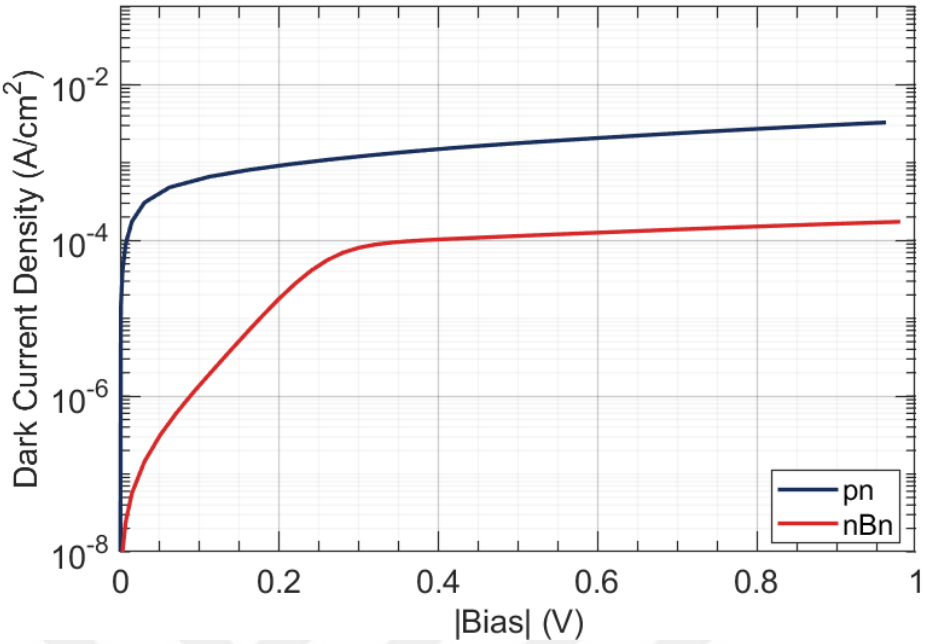


Figure 3.11: Comparison of dark currents of nBn and pn.

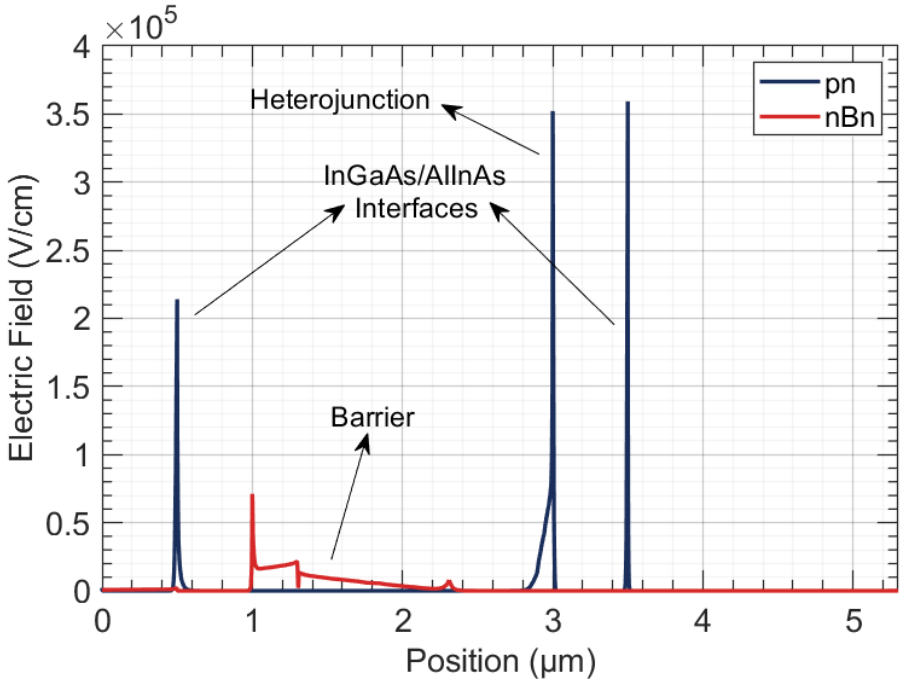


Figure 3.12: Built-in electric fields of nBn and pn structured photodetectors.

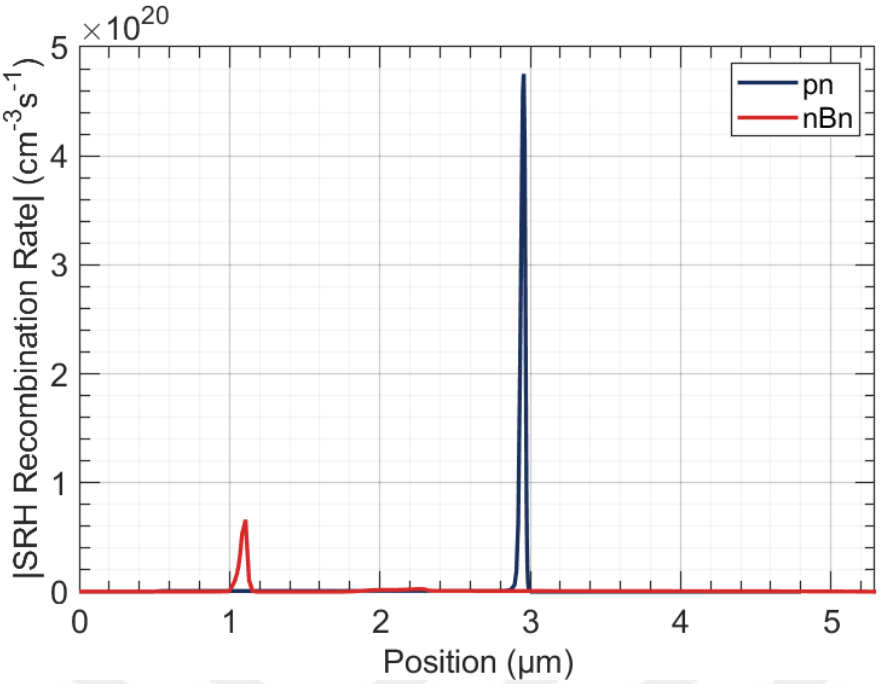


Figure 3.13: SRH recombination rates observed in nBn and pn structured photodetectors.

nBn structures are offered to suppress SRH current, which is problematic primarily for lattice-mismatched materials with lower carrier recombination lifetimes. Then, the SRH recombination lifetime was swept for the device to investigate behaviors of nBn and pn structures for different recombination lifetime values. Parallel with the expectation, the difference between nBn and pn structures increased with decreasing recombination lifetime, as shown in Figure 3.14.

The effective removal of the valence band offset was also observed in photocurrent simulations, as results were shown in Figure 3.15. The nBn type detector provided the same photocurrent as the pn junction detector, where pn junction detectors are associated with high quantum efficiencies.

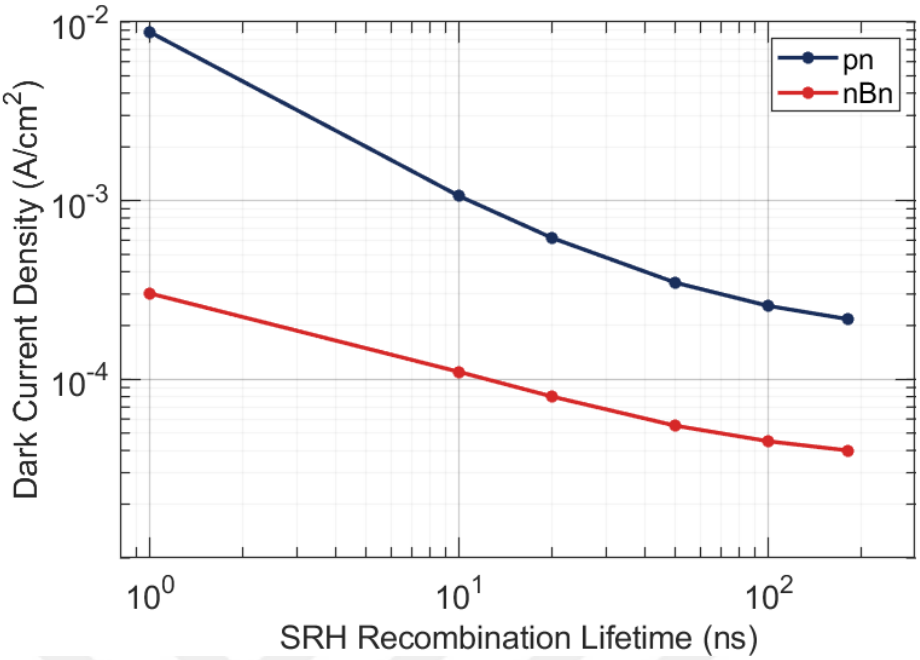


Figure 3.14: Dark currents calculated for different SRH recombination lifetimes for nBn and pn.

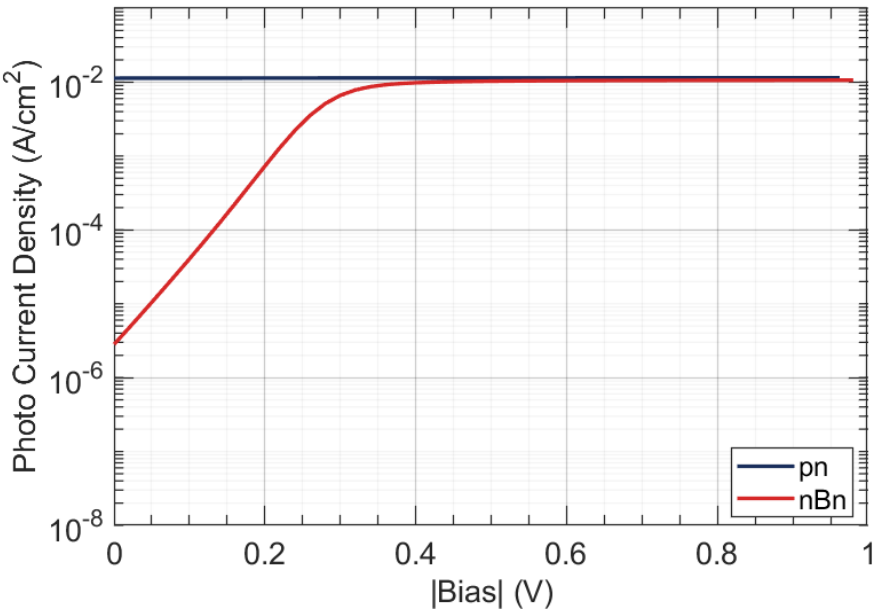


Figure 3.15: Comparison of photocurrents of nBn and pn.

3.2.2 Dual-Band InGaAs nBn Photodetector at 1.7 µm / 2.2 µm

It was noticed that it is also possible to use the designed nBn photodetector as a dual-band sensor. The single-band sensor was modified to be a dual-band sensor by converting 1 μm thick InGaAs layer to a SWIR absorber layer by increasing the thickness. On the other hand, the pn junction structure was modified to a greater extent to be converted to a dual-band detector, where the resulting epilayer was presented in Figure 3.16. Each diode being a single-color detector, two diodes were assumed to be connected back to back to obtain the dual-band structure. The lattice mismatch between the SWIR and eSWIR detectors was introduced during the p-type barrier region sandwiched between the absorbers.

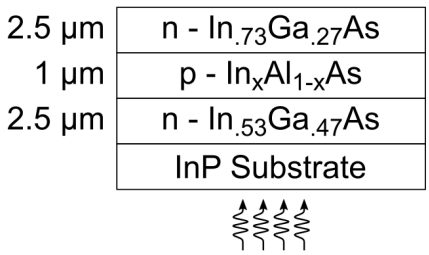


Figure 3.16: Epilayer of the npn structure.

In conclusion, nBn and npn detectors were arranged as bias selective dual-band photodetectors. In bias selective dual-band photodetectors, subdetectors with distinct spectral responsivities are separately activated by setting the dedicated biasing voltage and polarity. The Figure 3.17 illustrates bias selective dual-band operation for nBn and npn structures. The applied bias of -50 mV results in Figure 3.17a, where the carriers generated in the SWIR side can travel through the barrier while carriers generated in the eSWIR side are blocked by the barrier. The same principle applies to the npn case, as in Figure 3.17b. On the other hand, the applied bias of 300 mV causes generated carriers in the SWIR side to be blocked by the barrier, while the eSWIR side is actively providing photoresponse. This is achieved by changing the flow direction and overcoming the energy difference between two absorbing layers, as shown in Figure 3.17c. The same idea also applies to npn case as in Figure 3.17d.

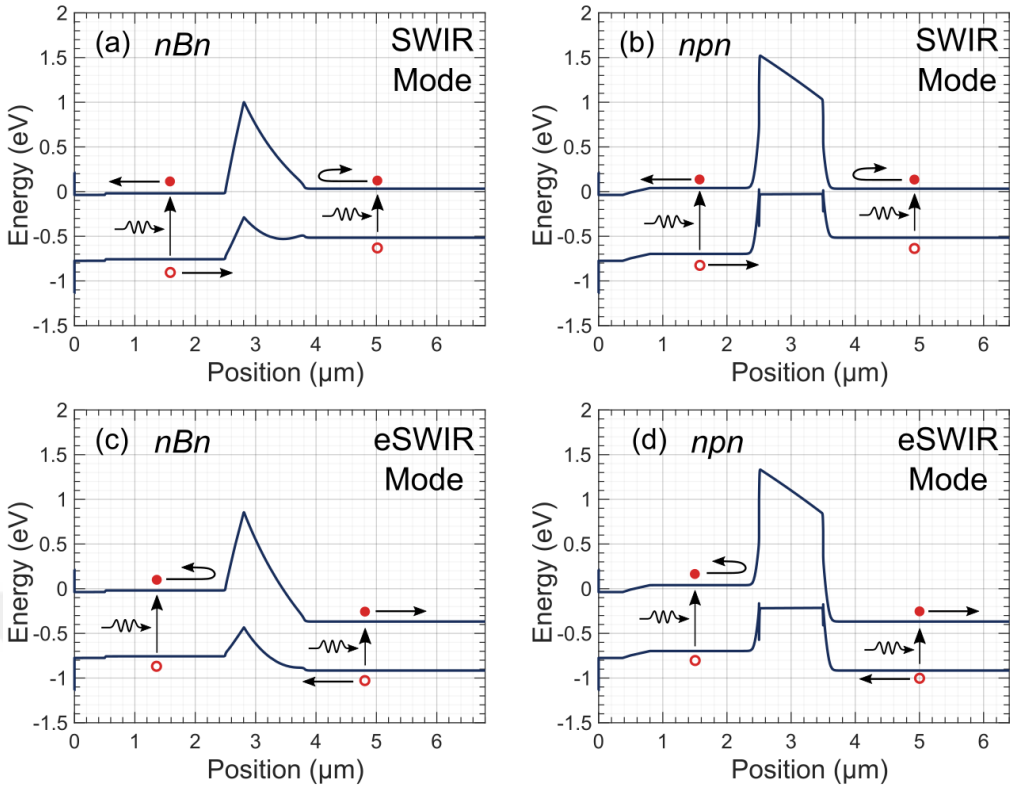


Figure 3.17: Dual-band operation. (a) SWIR mode in nBn, (b) in npn, (c) eSWIR mode in nBn, (d) in npn.

When dark currents of the resulting dual-band detectors were investigated, it was observed that dark currents are dependent on the SWIR absorber doping levels. Then, the SWIR absorber doping levels were swept from $N_d = 10^{15}\ cm^{-3}$ to $N_d = 2 \times 10^{18}\ cm^{-3}$ for both devices, where results are depicted in Figure 3.18. It was found that increasing doping density monotonically decreases the dark current for the nBn case, while the dark current density cannot be decreased below a certain level for the npn case.

The behaviors of both devices can be explained by investigating the built-in electric fields. Although nBn devices operate with lower electric fields than photovoltaic devices, the electric field still existed here. This nBn structure was designed so that the electric field due to compositional grading of the barrier compensates the electric field due to the delta doping layer. Since higher doping levels in the barrier causes valence band offset, the doping level of the barrier region was kept as low as the

MBE background doping level. If doping levels were also kept low in the absorber, the electric field tended to expand into the absorber region, as shown in Figure 3.19.

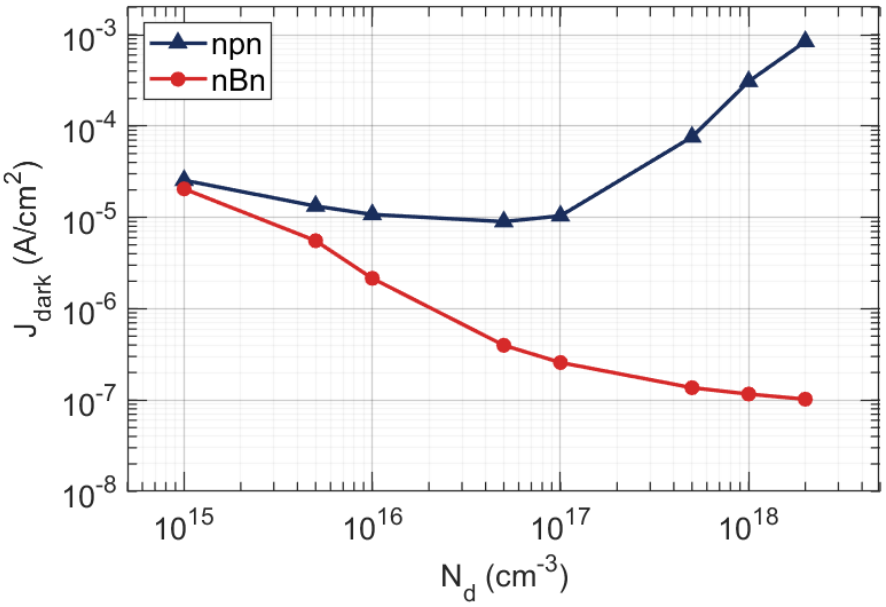


Figure 3.18: Dark current density vs. SWIR absorber doping density.

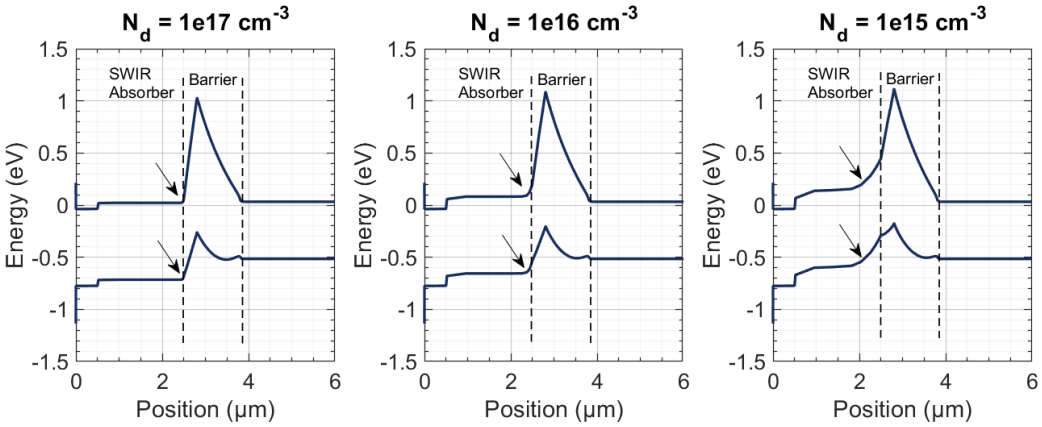


Figure 3.19: Band diagrams for different SWIR absorber doping levels, where band-bending occurring between the SWIR absorber and the barrier should be noticed.

Higher SRH rates causing higher dark current due to the expansion of the electric field was observed as in Figure 3.20. Therefore, increasing the doping density suppressed the SRH and the dark current by inhibiting the expansion of the electric field into the absorber. Because the energy barrier was thick enough to avoid tunneling

mechanisms, increased doping densities in the nBn device did not activate tunneling. On the other hand, the same idea did not not apply to the npn case. Higher doping levels were unsuitable in the npn case since higher doping levels promoted tunneling and further increased the dark current. Since tunneling should be strictly avoided, high doping levels in npn was also be avoided.

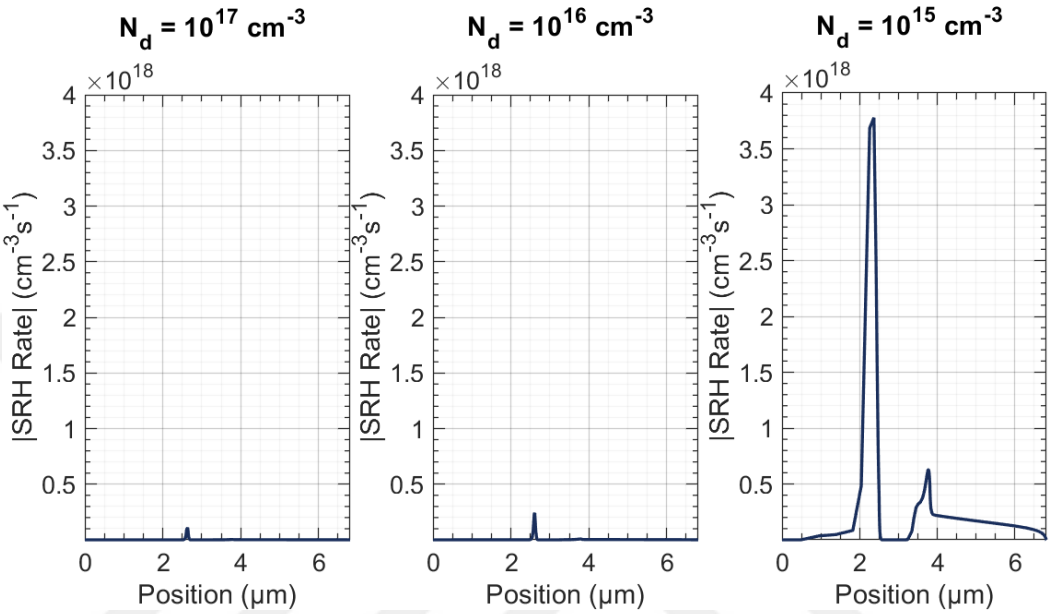


Figure 3.20: SRH rates for different SWIR absorber doping levels.

When the photocurrents were investigated for various absorber doping levels, it can be seen in Figure 3.21 that photocurrents decreased towards higher doping levels due to the Auger recombination. Finally, optimum spots for nBn and npn structures were selected as $N_d = 5 \times 10^{17}\ cm^{-3}$ and $N_d = 5 \times 10^{16}\ cm^{-3}$, respectively.

Current-voltage simulations for the optimum spots resulted in Figure 3.22, where nBn case provides significantly lower dark current for both bands. Not surprisingly, nBn detector yielded the same dark current density for positive operating voltages as it can be acknowledged by comparing Figure 3.11 and Figure 3.22. While assessing the performance of the npn detector, it should be noted that required biasing voltage increased to 300 mV for the extended shortwave operation. Similar to the nBn detector, bandgap differences between two absorber layers caused this increase, as it can be verified by Figure 3.17. Dark current performances of the SWIR sides of both structures were observed to be significantly worse than the state-of-the-art single-band

lattice-matched InGaAs photodetectors operating at 1.7 μm. This observation was attributed to the presence of low bandgap extended shortwave subdetector, forcing a higher trap density and a shorter recombination lifetime in simulations.

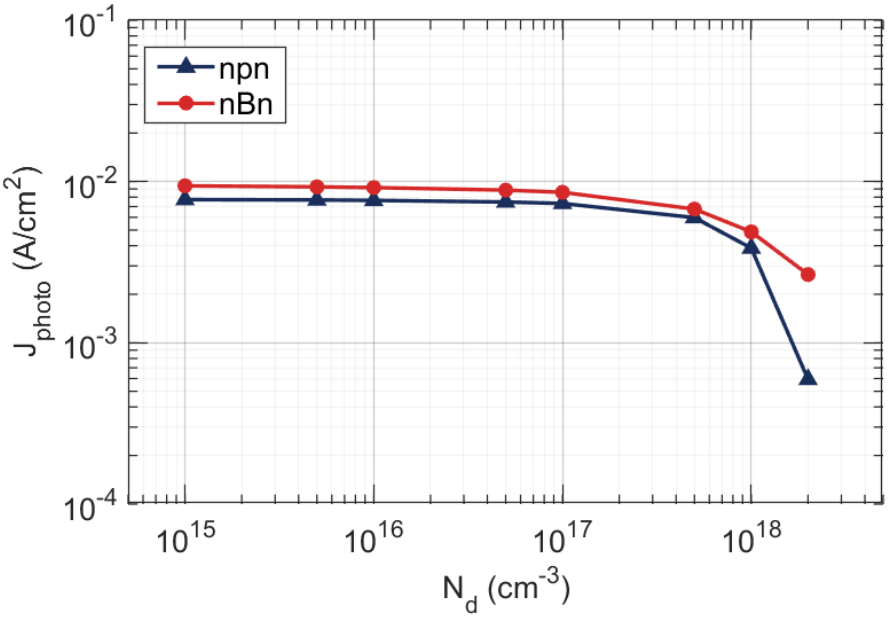


Figure 3.21: Photo current density vs. SWIR absorber doping density.

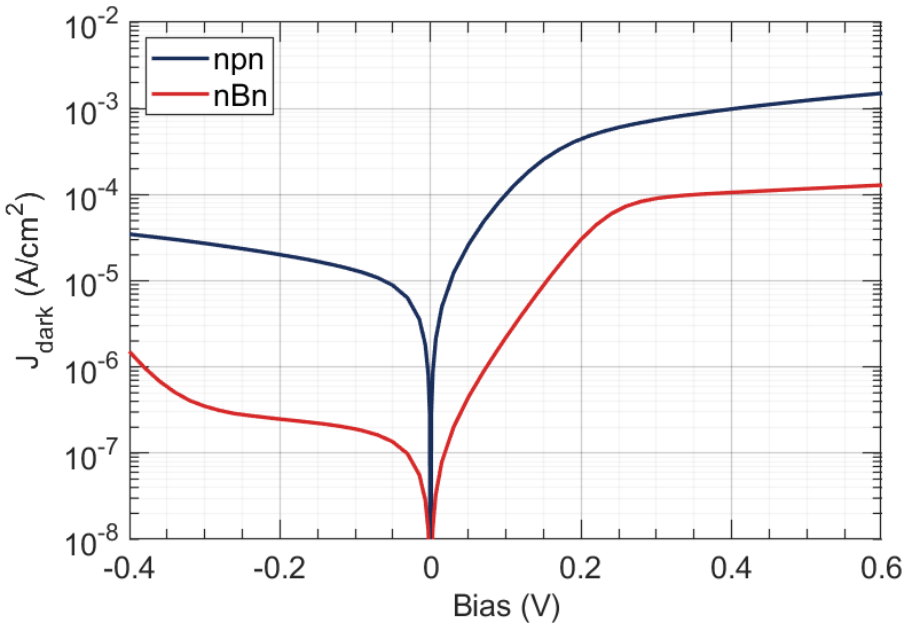


Figure 3.22: Dark current-voltage characteristics of nBn and npn photodetectors.

For the photocurrent simulations given in Figure 3.23, very similar characteristics of both devices can be acknowledged directly. For SWIR and eSWIR side simulations, monochromatic sources at 1.5 μm and 2.2 μm were assumed, respectively. Figure 3.23 might be considered numerical demonstration of the discussion related to Figure 3.17. It should be noticed that applying negative biasing voltages to the device result in zero photoresponses for 2.2 μm illumination, where the device was responsive for 1.5 μm radiation. On the other hand, a positive voltage of 300 mV created a photoresponse of eSWIR radiation, where the response to 1.5 μm significantly decreased. In conclusion, bias selective dual-band operation was numerically presented, in which negative voltage corresponds to SWIR mode, and positive voltage corresponds to eSWIR mode.

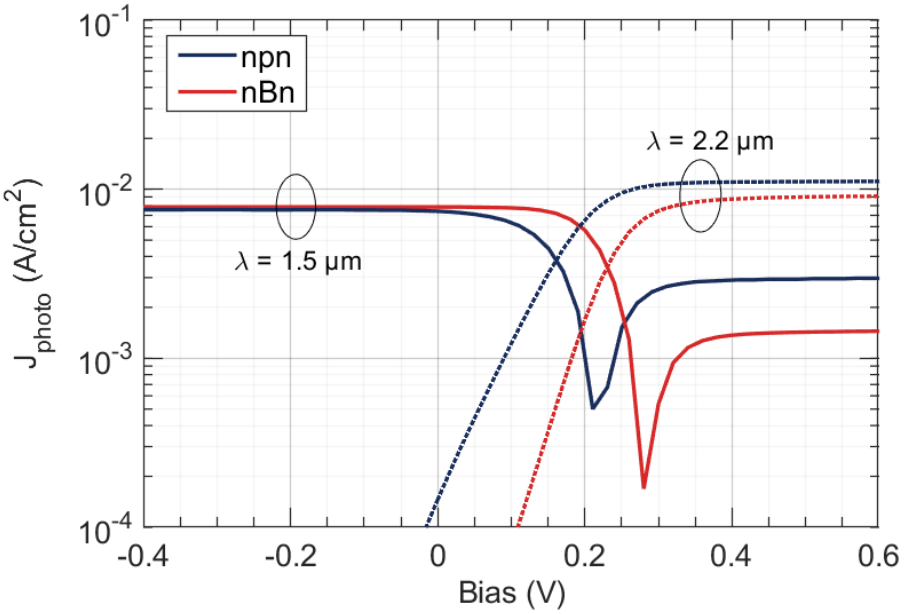


Figure 3.23: Photocurrent-voltage characteristics of nBn and npn photodetectors.

3.3 Realization

Designed and optimized wafer was grown using the in-house molecular beam epitaxy system (MBE). Then, the grown wafer was processed to fabricate photodetectors.

3.3.1 Growth Using Molecular Beam Epitaxy

MBE is one of the very high-quality semiconductor growing techniques where a schematical drawing of a typical MBE system was given in Figure 3.24. The growth chamber is the heart of the MBE machine. Typically, various vacuum pumps continuously operate to maintain an ultra-high vacuum (usually below 10^{-10} Torr) environment in the growth chamber of the MBE reactor. The substrate is introduced to the growth chamber through auxiliary chambers like the loading chamber and the buffer chamber. Effusion cells containing source materials are directly aimed at the substrate holder. Once source materials are evaporated from cells, they directly hit the substrate without any undesired collisions in the presence of the ultra-high vacuum environment. The substrate is typically heated to an optimum temperature depending on the material and structure desired to be grown. Then, at the surface of the wafer, evaporated source materials combine and crystallize to build the desired semiconductor epilayer.

Some sophisticated in-situ characterization devices are also included in the growth chamber. Some of them, such as pyrometer, ellipsometer, and reflecting high-energy electron diffractometry (RHEED), can be exemplified. A pyrometer reads the substrate temperature and helps to decide the correct manipulation of substrate temperature. Ellipsometry provides information about the mole fraction of epilayers utilizing the optical properties of thin films. RHEED is based on a similar principle to X-Ray Diffraction (XRD), where electrons are sent to the substrate, and the diffraction pattern due to reflecting electrons from the substrate is observed on the dedicated flourescent screen. If correctly interpreted, RHEED patterns might guide the semiconductor growing progress.

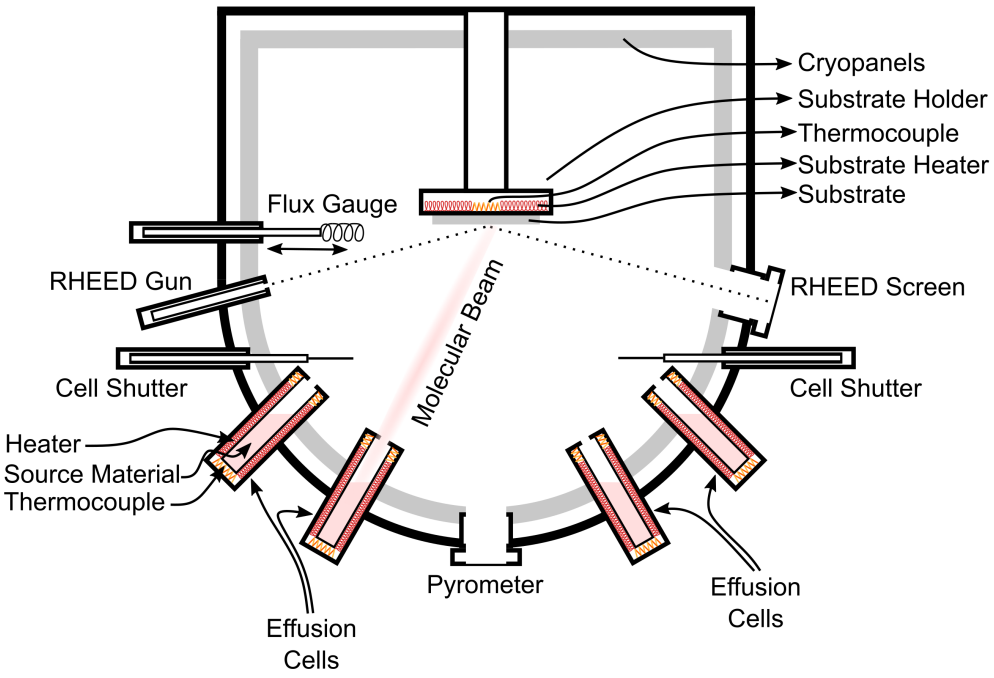


Figure 3.24: Schematical drawing of a typical MBE system.

The in-house MBE system, Riber Epineat, is dedicated to III-V semiconductors and provides excellent uniformity up to 4 inch substrates. Solid Al, Ga, In sources, P, As cracker cells, and Si, Be dopant cells are available. RHEED and pyrometer are utilized for in-situ monitoring of the growth process. The epilayer growth was conducted following the procedure outlined here.

First, liquid nitrogen was filled in the hollow walls of the growth chamber to further reduce the chamber pressure down to 10^{-11} Torr. Then, cells were heated to degassing temperatures to avoid any undesired degassing or evaporation during the growth. Meanwhile, the RHEED gun was fed with the current to degass and stabilize. Once the preparation steps were completed with the flux calibration of cells, native oxide on semi-insulating InP substrate was desorbed, and the growth was started by opening the main shutter. The RHEED screen and the substrate temperature were monitored frequently.

Since the nBn device was initially planned to be a single color photodetector, the SWIR absorber was grown 1 μm thick. Grading the Al, Ga, and In temperatures, barrier structure was grown. Finally, eSWIR absorber of 3 μm thick was grown, and

the MBE reactor was returned to standby configuration.

3.3.2 Fabrication of the Photodetector

Fabrication steps of the photodetector were completed using the in-house clean room and equipment. All structures were patterned on a standard Shipley S1828 photoresist using Heidelberg μPG501 direct writing lithography system. The overall fabrication process was outlined below in Figure 3.25.

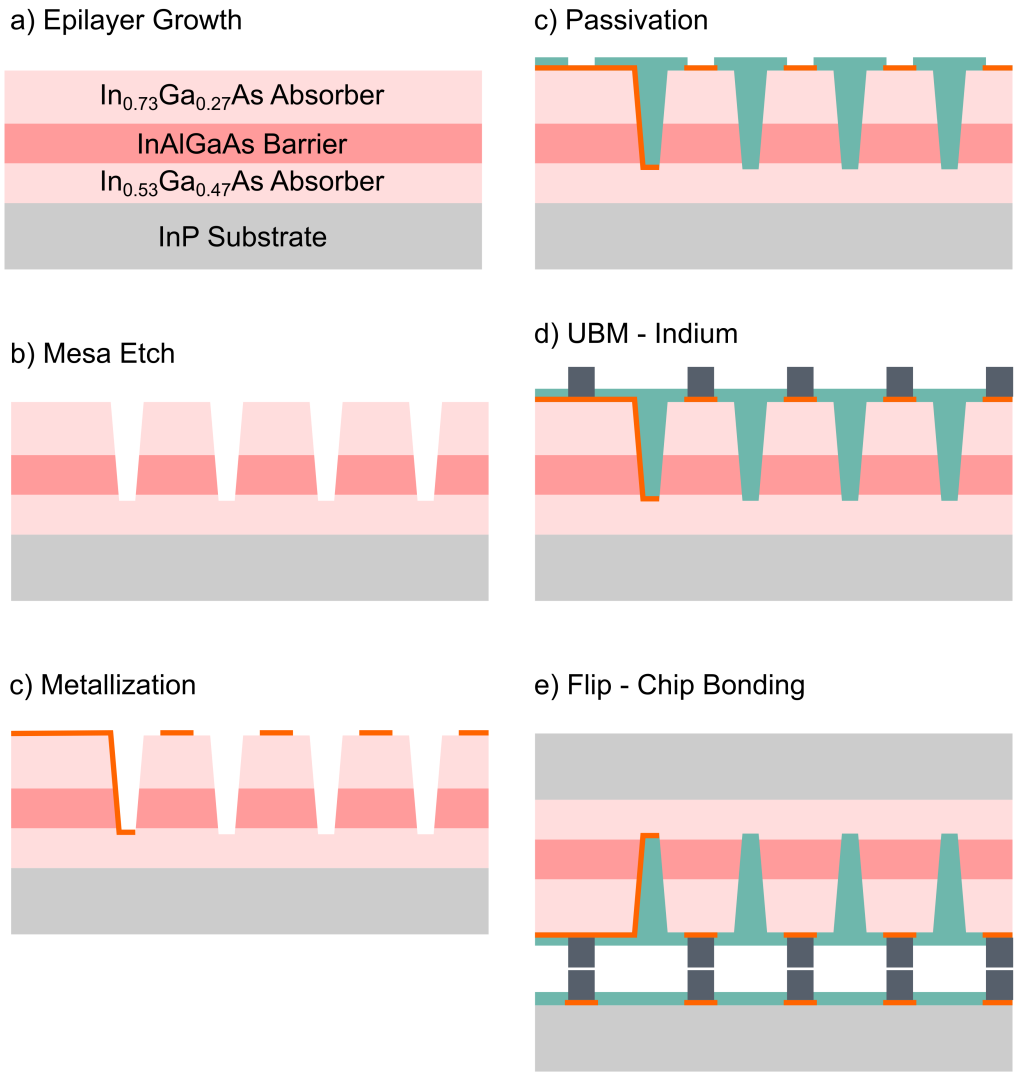


Figure 3.25: Fabrication of the Photodetector.

After the epilayer growth (a), a region of the wafer was diced into 1 x 1 cm chips. Photodetector mesas were defined (b) with wet etching using an anisotropic etchant solution $H_3PO_4 : H_2O_2 : H_2O$. Photolithography patterns were aligned to the [1-10] direction of the crystal. Then, angled walls [79] were obtained to achieve a higher fill factor. Following the mesa etching step, AuGe/Ni/Au metals were coated in predefined regions (c). A short annealing step was performed for ohmic contact formation by driving Ge atoms inside the epilayer and achieving a very high doping level. After a short dip in the etchant, a dielectric was spin-coated on the sample for passivation and encapsulation purposes (d). Following the under-bump metallization (UBM) with Ti/Ni/Au, indium bumps were formed (e). Finally, the detector was flip-chip bonded to a dedicated fanout circuit (e).

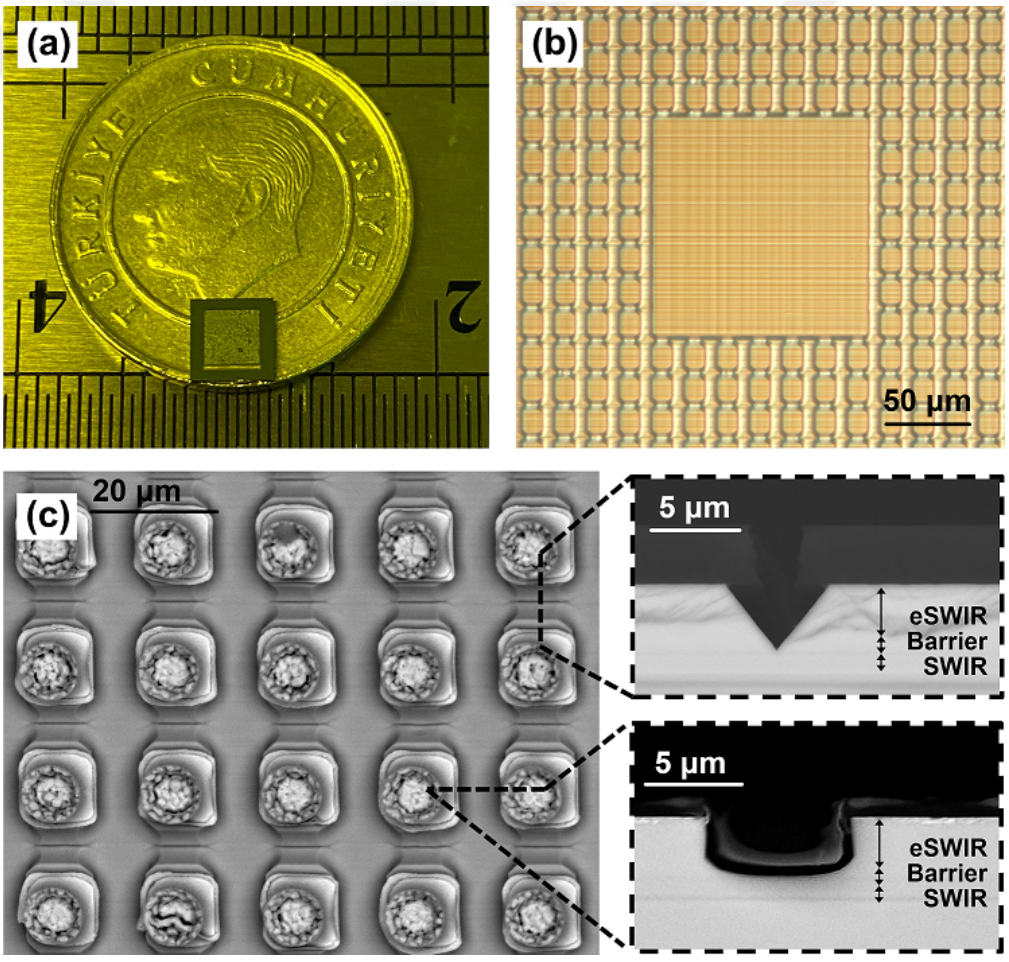


Figure 3.26: (a) Fabricated photodetector chip ready for flip-chip bonding, (b) optical microscope image showing different area pixels, (c) SEM images of $20\times20\mu m^2$ pixels with insets showing etching profiles.

Photodetector chips realized with the process steps, just explained above, were presented in Figure 3.26. Crosshatch pattern, which inevitably occurs due to the lattice mismatch between the epilayer and the substrate, did not cause a problem for processing of chips. Insets of Figure 3.26c clearly depicted the angled walls obtained with anisotropic etchant solution.

3.4 Characterization

Following the fabrication steps, the dark current and the optical performance of the nBn photodetector were characterized.

3.4.1 Optical Performance

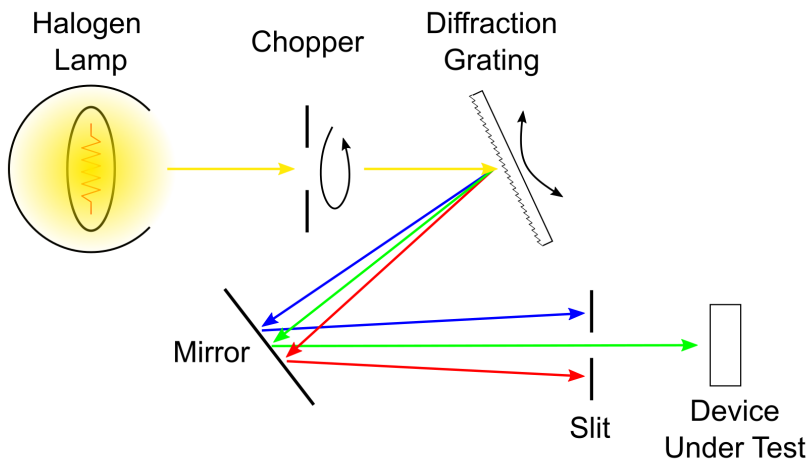


Figure 3.27: Schematical drawing of a monochromator similar to the one used for characterization.

Optical characterization of the fabricated back side illuminated FPA-like pixels was conducted using a monochromator with a low frequency chopper and a lock-in amplifier at mild room temperature. The monochromator test setup was drawn schematically in Figure 3.27, where a diffraction grating disperses the light coming from a halogen lamp, and wavelengths incident to the sample were selected according to the angular position of the grating. The preamplifier was employed to amplify the pho-

tocurrent signal and convert it to voltage. The lock-in amplifier was used to lock the signal with the frequency of the chopper to measure more accurately.

It was not possible to directly obtain the optical performance metrics of the photodetectors since the power incident to the device under test was not precisely known. A calibrated reference photodetector was first utilized to measure the spectral power incident to it. The relationship between the test setup and the measured signal level was expressed as follows:

$$v_{ref}(\lambda) = \phi(\lambda) \cdot A_{ref} \cdot G_{ref} \cdot R_{ref}(\lambda) \tag{3.15}$$

where v denotes signal reading, ϕ denotes incident optical power per unit area, R denotes responsivity, A denotes area, and G denotes preamplifier gain. Then, the detector under test (dut) was measured in the same conditions. Normalizing two measurements yielded the responsivity data of the detector as follows:

$$R_{dut}(\lambda) = \frac{v_{dut}(\lambda)}{v_{ref}(\lambda)} \cdot \frac{A_{ref}}{A_{dut}} \cdot \frac{G_{ref}}{G_{dut}} R_{ref}(\lambda) \tag{3.16}$$

Before determining the quantum efficiency and responsivity values, lateral collection distances were obtained. Since the SWIR side pixels were not completely isolated, photogenerated carriers in neighboring pixels flow to the pixels under test, contributing to the photocurrent as shown in Figure 3.28. Thus, the lateral collection distance should be considered to avoid being misguided by spuriously high signals due to the lateral collection of carriers. The measured signal from the photocurrent is proportional to its area under the same illumination conditions. In case of lateral collection, the effective area of pixels changes due to the contribution of photogenerated carriers from neighbors as follows:

$$I_{photo} \propto (d + 2l_c)^2 \tag{3.17}$$

where l_c is the lateral collection distance, and d is the geometrical side length of the pixel.

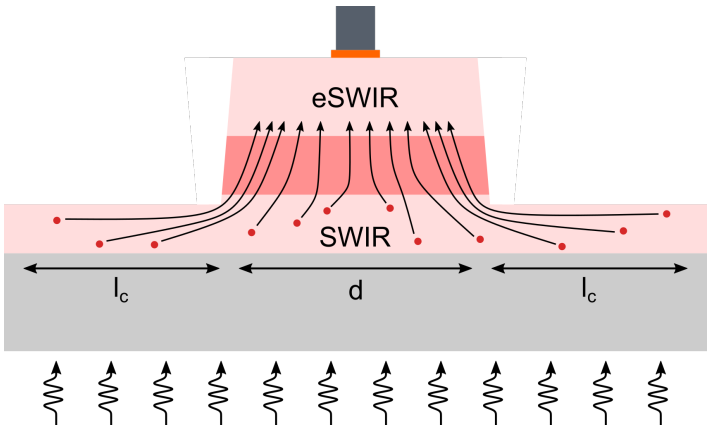


Figure 3.28: Illustration of lateral collection, where red dots demonstrate photogenerated carriers.

Therefore, using the different area pixels, square root of photocurrent values were drawn with respect to the geometrical side length of the pixels, as given in Figure 3.29. The lateral collection distance was found to be $l_c = 48.5\ \mu m$ for the SWIR side subdetector, while no lateral collection was observed in the eSWIR side since the pixels were fully isolated.

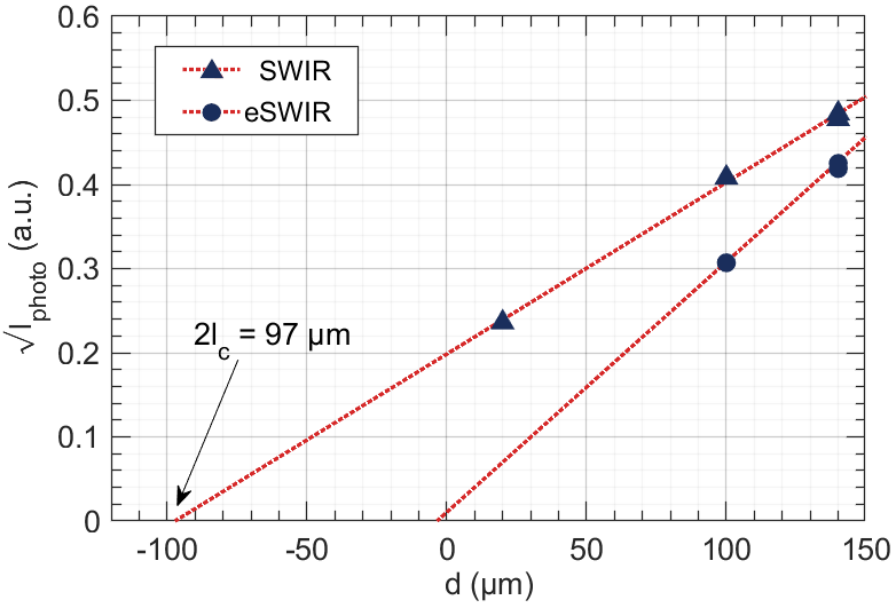


Figure 3.29: Photocurrent readings from signals with different areas for both SWIR and eSWIR regions.

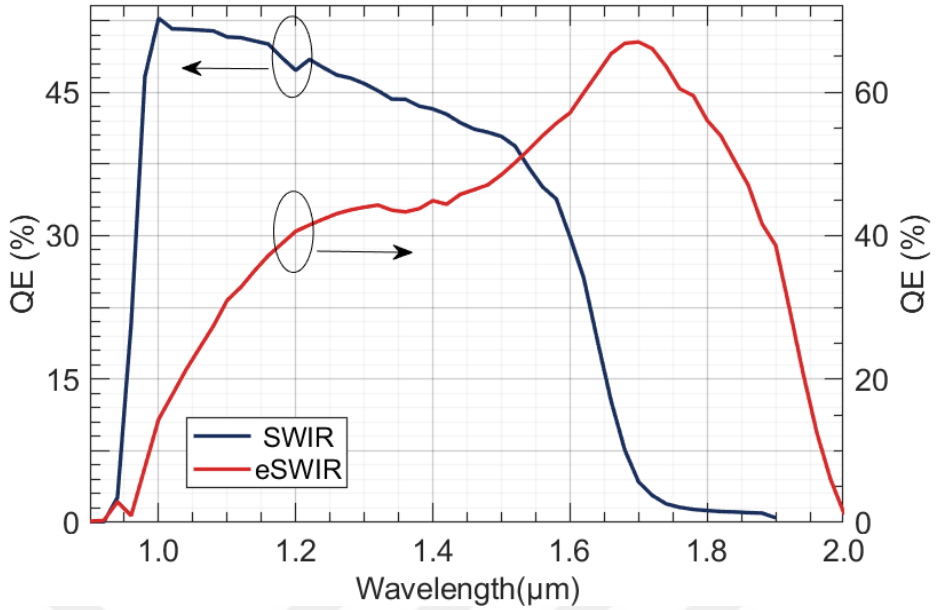


Figure 3.30: Room temperature quantum efficiencies at bias voltages -50 mV for SWIR and 300 mV for eSWIR.

Once lateral collection distances and reference measurements were obtained, quantum efficiency values of the nBn photodetector were calculated, as depicted in Figure 3.30. Operating bias voltage of -50 mV and 250 mV were assumed for SWIR and eSWIR detectors, respectively. Before commenting on the results, it should be noted that no anti-reflective coating (ARC) was applied to the surface of InP, where 27% of the incident radiation is reflected due to Fresnel's reflections. If a proper ARC were applied, the peak quantum efficiency of 67% measured for the eSWIR side would correspond to a quantum efficiency of 92%. To interpret the peak quantum efficiency of 53% observed for the SWIR side, the grown epilayer given in Figure 3.7 must be investigated. The 1 μm thick SWIR absorbing layer was insufficient to absorb all the incident radiation. Since the absorption coefficient for shorter wavelengths is greater than longer wavelengths, the peak quantum efficiency was observed at the incident wavelength of 1 μm. Since the absorption at the SWIR side was not high enough, a significant amount of photons passed through the SWIR side and reached the eSWIR side. Thus, spectral crosstalk between the bands was identified in the wavelength interval between 1.0 – 1.7 μm. A thicker SWIR absorber should increase the quantum efficiency at the SWIR side and decrease the spectral crosstalk between the bands.

3.4.2 Dark Current

The sample containing the large area pixels was placed in a cryostat, that can be cooled down to 80 K by filling its reservoir with liquid nitrogen. The temperature of the sample holder can be adjusted by a feedback controlled internal heater.

Temperature-dependent dark current measurements were taken between 200 K and 300 K with temperature steps of 10 K using a high precision source measure unit. Although sufficiently large pixels ($400 \times 400\,\mu m^2$) were fabricated to measure the devices at low temperatures, the dark current was still too low to be measured below 200 K. Once normalized versus active areas of pixels, measurement results were depicted in the Figure 3.31.

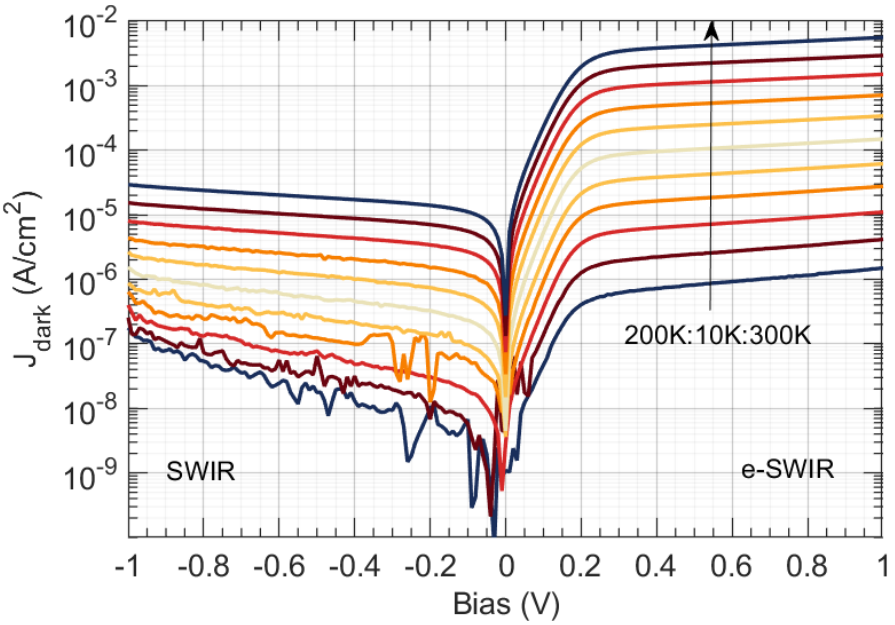


Figure 3.31: Temperature dependent dark current density vs. applied bias.

Dark current values at $V_b = -50\,mV$ and $V_b + 300\,mV$ were compiled for the SWIR, and the eSWIR detectors, respectively. Then, data points were plotted, and activation energies were modeled in the Arrhenius plot shown in Figure 3.32. Interestingly, both subdetectors yielded the same activation energy of $E_a = 452\,meV$, where numerical fitting results can be expressed as follows:

$$J_d = 2.33 \times 10^2 \times e^{-0.452/k_bT}\ A/cm^2 \tag{3.18}$$

$$J_d = 1.32 \times 10^5 \times e^{-0.452/k_bT}\ A/cm^2 \tag{3.19}$$

Considering the bandgap of the extended shortwave subdetector, which is $E_g = 0.62eV$, Equation 3.19 was arranged as follows:

$$J_d = 1.32 \times 10^5 \times e^{-0.62/1.37k_bT}\ A/cm^2 \tag{3.20}$$

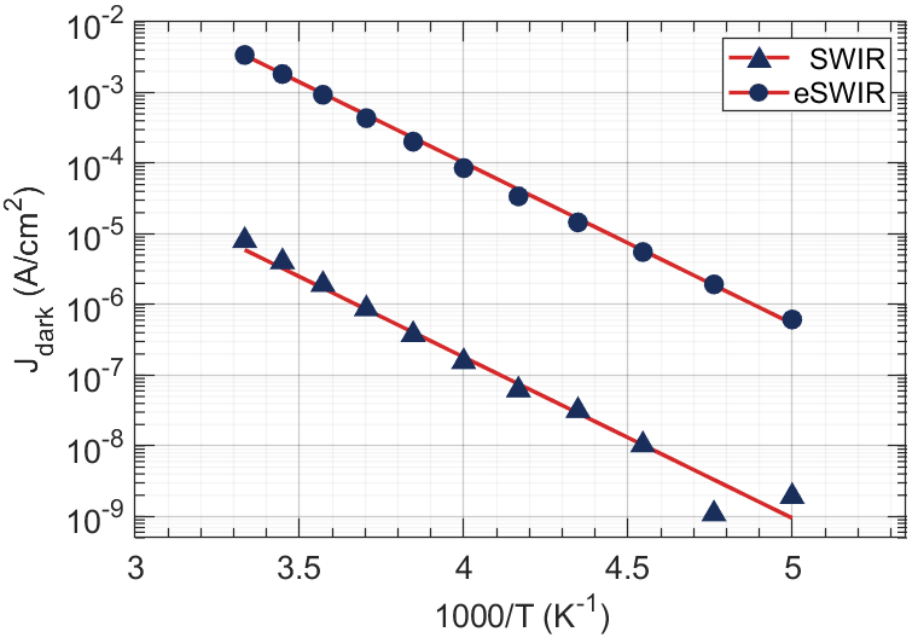


Figure 3.32: Arrhenius plot for current density.

The ideality factor of $\eta = 1.37$ was obtained, meaning that GR current was effectively suppressed, although some portion is still present [80]. Furthermore, no sign of tunneling and surface leakage was observed since the activation energies are constant throughout the measurement range. The identical activation energy of 0.452 eV for both subdetectors supported that there should be a dark current mechanism common to the whole device. This dark current source was attributed to the band bending inside the barrier region.

Dynamic resistance values were calculated and compiled in an Arrhenius plot, as shown in Figure 3.33. Numerical fitting yielded for the area-dynamic resistance product, considering the bandgap of 0.62 eV:

$$J_d = 4.04 \times 10^{-6} \times e^{0.62/1.37k_bT}\ \Omega cm^2 \tag{3.21}$$

$$J_d = 2.22 \times 10^{-5} \times e^{0.62/1.37k_bT}\ \Omega cm^2 \tag{3.22}$$

The same deductions were made with the Arrhenius plots for the dark current. It should be noted that a sufficiently high $R_d \times A$ product of $10^6\ \Omega cm^2$ was obtained for both subdetectors at 200 K. This $R_d \times A$ product was recognized as satisfactory in providing good injection efficiency to an ROIC and presenting low Johnson noise [46].

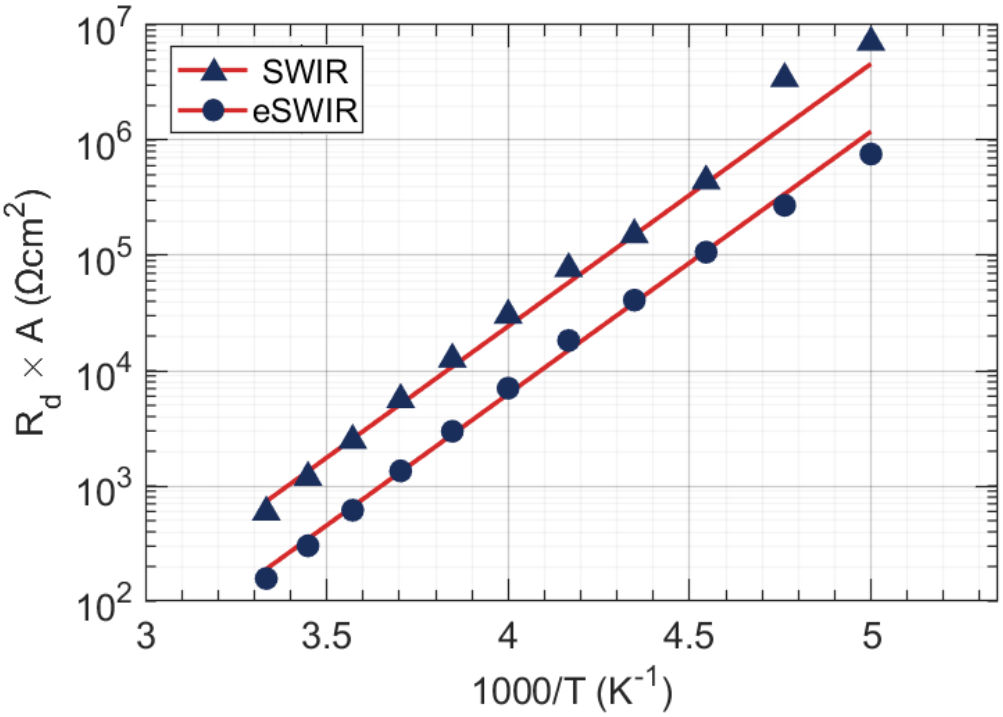


Figure 3.33: Arrhenius plot for resistance area product.

In addition to large area pixels, FPA-like small area pixels were also characterized. During the 20 μm fabrication process, some pixels were not isolated and left as large area pixels. These pixels were employed to characterize the surface leakage current.

Assuming there exists a surface leakage current, the total dark current can be estimated as follows:

$$I_d = J_{d,bulk}A + J_{d,surface}P \tag{3.23}$$

where A denotes the effective detector area, $J_{d,bulk}$ denotes bulk dark current density, P is the perimeter of the pixel, and $J_{d,surface}$ is the surface dark current density. Then, normalizing the equation with the detector area yields:

$$J_d = J_{d,bulk} + J_{d,surface}P/A \tag{3.24}$$

As a result, the dark current should be expected to change with the area to perimeter ratio of the detector if there is a significant surface leakage current. Employing pixels with various A/P ratios, dark current density measurements in a mild room temperature yielded Figure 3.34. The surface current free behavior observed in Figure 3.32 was also verified in Figure 3.34, considering the slopes of the fitting curves.

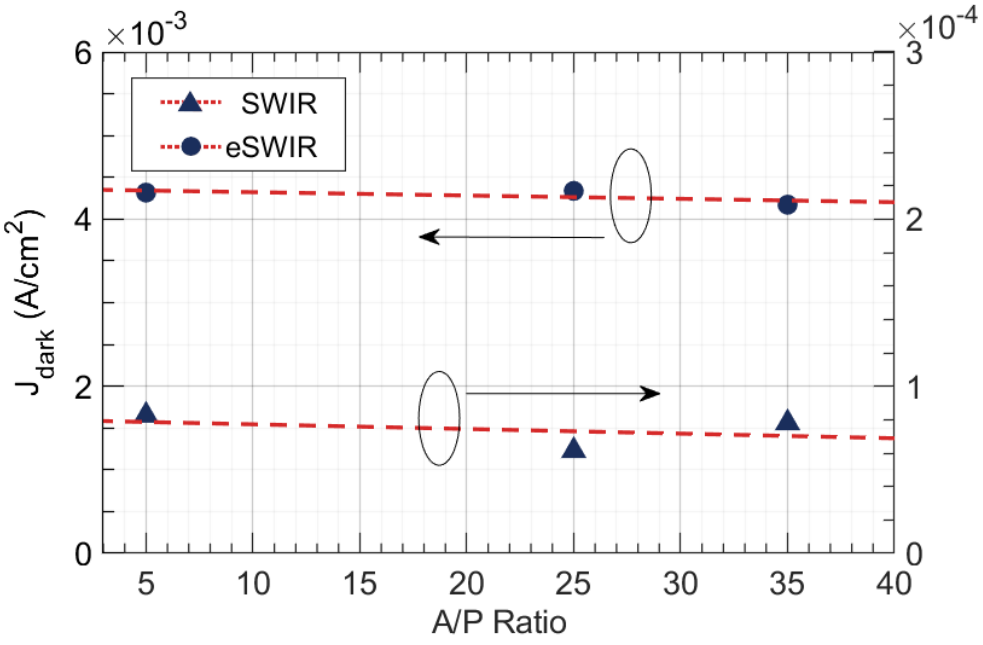


Figure 3.34: Dark current densities in different sized pixels.

If the design study and the characterization results were compared, it could be noticed that the measured cut-off wavelength was shorter than the designed cut-off wavelength. This discrepancy supported that an undesired deviation occurred in the In, Ga, or Al fluxes during the growth of the detector epilayers. Higher than expected dark current density was attributed to the same unoptimized growth conditions since any nonideality is prone to degrade the overall detector performance.

3.4.3 Noise

The noise measurements were conducted in the same cryostat using a low noise preamplifier and a dynamic signal analyzer. Near room temperature measurements on the eSWIR detector with the applied biasing voltage of 300 *mV* yielded a 1/f noise-dominated characteristic at low frequencies, as shown in Figure 3.35. Although the origin of the flicker noise is not precisely known, the 1/f noise observed here can be attributed to the dislocation and material defects occurring due to the significant lattice mismatch between the InP substrate and the eSWIR absorber [35].

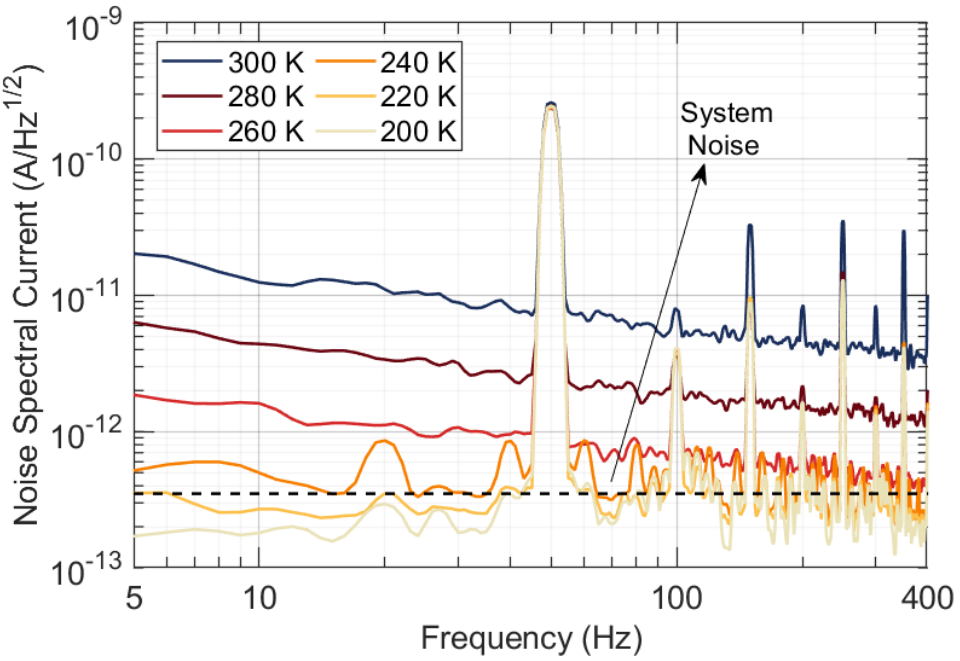


Figure 3.35: Noise characteristic of the eSWIR detector for a biasing voltage of +300 *mV* at different temperatures.

Cooling the detector decreased the noise with a slope having an activation energy of 329 meV, as shown in Figure 3.36. The slope with nearly $E_g/2$ supported the assumption that the flicker noise occurs due to the deep level traps. The fixed slope decrease in the noise could be observed at temperatures down to 240 K. However, the noise of the $400 \times 400\ \mu m^2$ large area could not be obtained below 240 K since the noise due to the measurement setup dominated the overall measured noise. Considering the dark current densities in Figure 3.31, the corresponding shot noise was also calculated using Equation 1.14, and also shown in Figure. It could be observed that the shot noise starts to be the dominant contribution for noise at 333 Hz for temperatures below 240 K. In addition, the dependence of the 1/f noise on temperature is greater than that of the shot noise, meaning that the detector would be shot noise limited at 200 K if the slope for 10 Hz noise remains constant.

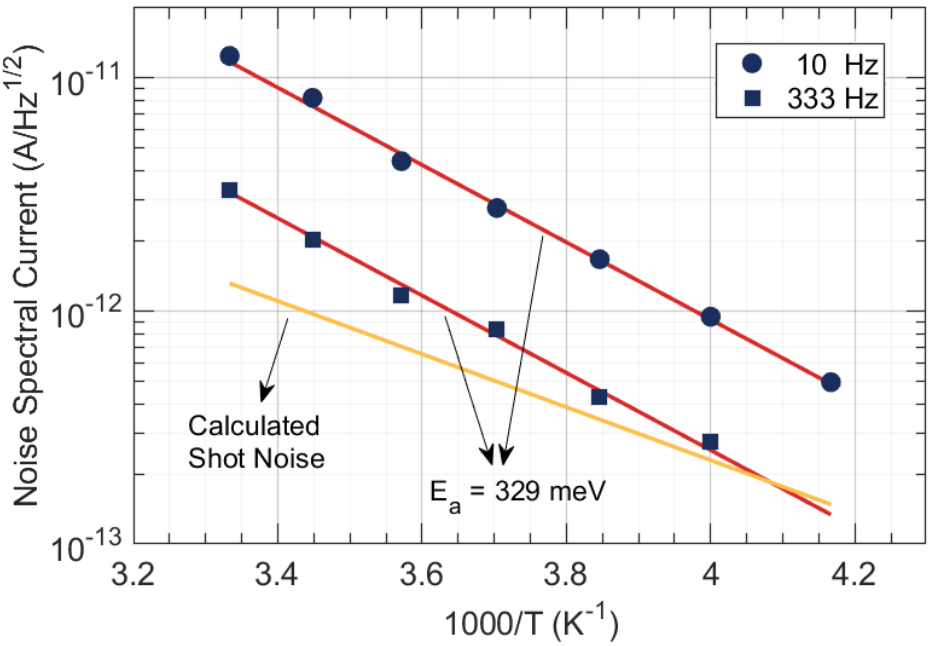


Figure 3.36: Arrhenius plot of noise characteristic of the eSWIR detector for a biasing voltage of +300 mV at different temperatures.

Similar to the low-temperature measurements on the eSWIR detector, the noise characteristic of the SWIR detector with the biasing voltage of -250 mV could not be measured even at 300 K due to the dominated system noise.

3.4.4 Specific Detectivity

Finally, the specific detectivity for the eSWIR detector at 300 K was calculated by combining the responsivity and the noise via Equation 1.17. As depicted in Figure 3.37, the eSWIR detector provided peak detectivity exceeding $10^{10}\ cm\sqrt{Hz}/W$ even at room temperature. As presented in Figure 3.36, the spectral noise current decreased by one order of magnitude if the detector was cooled to 250 K. In other words, operating the detector at 250 K would provide one order better specific detectivity. Furthermore, if the assumption of shot noise-dominated characteristic at 200 K is correct, the detector would yield a peak specific detectivity on the order of $10^{12}\ cm\sqrt{Hz}/W$.

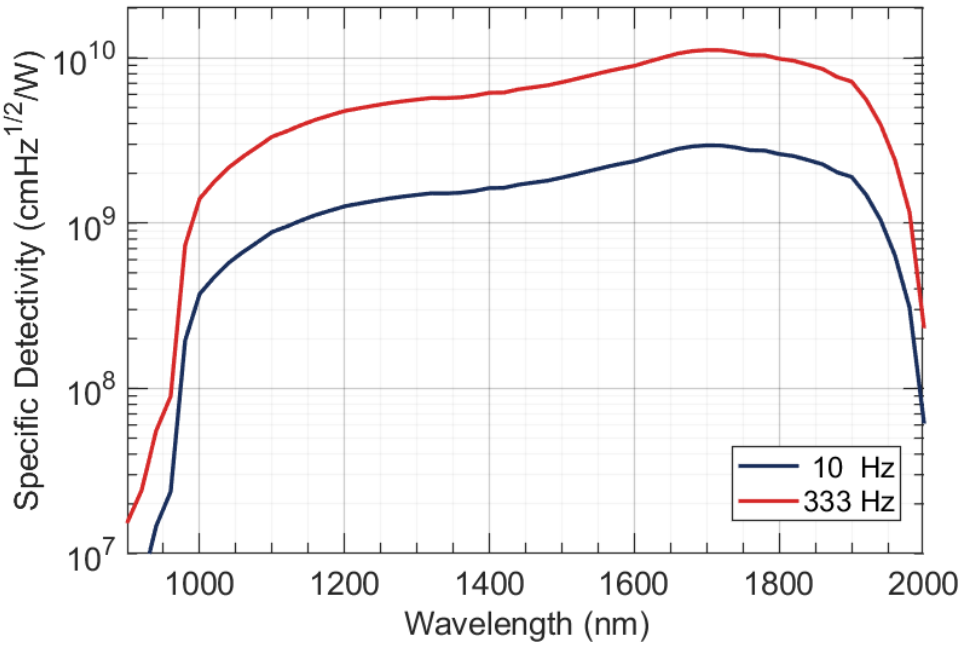


Figure 3.37: Specific detectivity of the eSWIR detector for a biasing voltage of +300 mV at room temperature.

Considering the noise of the measurement setup of $\sim 3 \times 10^{-13}\ A/\sqrt{Hz}$, the noise associated with the SWIR detector must be less than that values since it could not be obtained even at room temperature. Therefore, it is straightforward to predict that the peak detectivity for the SWIR side should be greater than $10^{12}\ cm\sqrt{Hz}/W$.

CHAPTER 4

CONCLUSION AND FUTURE WORK

In this thesis study, an nBn type dual-band InGaAs at 2 μm photodetector was designed, grown, fabricated, and characterized. Results were presented and discussed in detail.

Critical parameters were carefully compiled from the literature during the simulation period to create a realistic simulation environment. The simulation environment was employed for numerical calculations regarding photovoltaic and nBn type detectors. nBn detectors yielded lower dark current than photovoltaic ones, while a similar photocurrent for both structures was obtained. After a slight variation to the initial nBn single-color detector, a dual-band nBn device was designed. To construct the nBn structure, an unintentionally doped InAlGaAs barrier was sandwiched between two n-type InGaAs absorber regions. A p-type nanolayer was employed to completely remove the valance band offset so that photoexcited carriers could freely travel inside the device. Further investigation on the dependence of photodetectors on absorber dopings provided that increasing doping density in nBn results in better dark current performance while higher absorber doping densities causes tunneling-dominated dark current characteristic for the pn case.

The optimized final structure was grown using the in-house Riber Epineat MBE machine. Encouraging and competitive results were obtained. Arrhenius plots and varying area pixel characterizations presented no sign of tunneling current or surface leakage. High quantum efficiencies verified that delta doping successfully removes the valance band offset. Dark current measurements at 300 K on a large area pixel yield 3.40 mA/cm^2 and 0.61 $\mu A/cm^2$ for the eSWIR and SWIR sides, respectively. Dark current values at 200 K for the eSWIR decreased to 8.05 $\mu A/cm^2$, while the SWIR

side provided 1.09 nA/cm^2. Optical measurements without anti-reflective coating yielded 67% and 53% peak quantum efficiencies for eSWIR and SWIR sides, respectively.

Revisiting the literature review presented in Chapter 2 would be helpful in assessing the contribution of this thesis study to the literature. The detector yielded Arrhenius plots with a constant slope of 0.425 eV despite the 4 μm deep trenches beyond the eSWIR absorber layer. Considering the dependence of total dark current on etch depth reported by Liu et al. [49] and Uliel et al. [51], the device structure proved a significant opportunity for dual-band sensors where deep trenches are inevitably required. Quantum efficiency values presented here, up to 67% without ARC, were similar to the detectors based on bulk materials reported by Ma et al. [50], Shafir et al. [41], and Arslan et al [46]. and higher than the T2SL-based detectors reported by Uliel et al. [51], Xie et al [53]. Similar to the noise characteristic reported by Ma et al. [35], the eSWIR detector presented flicker noise due to the lattice mismatch, while the noise of the SWIR side remained under the system noise. The high peak detectivity of 10^{10} $cm\sqrt{Hz}/W$ obtained at room temperature for the eSWIR detector was in the same order as the examples from the literature presented here. Furthermore, intraband dual-color detectors in the 1.0-2.5 μm region were missing up until, where two rare examples were reported in the literature by Nguyen et al. [52], and Xie et al. [53]. The dual-band SWIR/eSWIR InGaAs nBn photodetector presented in this thesis study proved a significantly better performance than its rare rivals in terms of quantum efficiency and dark current.

In concluding the contribution of this thesis study to the literature, the thesis study appeared in two conference proceedings and a journal article. The theoretical study was presented in SPIE Defense and Commercial Sensing, including nBn photodetector design and sensitivity analysis for the possible growth deviations [2]. The possibility of dual-band operation of the device discussed in this thesis study was demonstrated in Photonics West [3]. Finally, experimental and numerical results were published in Applied Physics Letters [4].

Although the eSWIR side cut-off wavelength of 2.2 μm was targeted, 2.0 μm was measured. However, the SWIR side cut-off wavelength was measured to be close to the goal, 1.7 μm. It was interpreted that deviations in material composition started in the barrier region, where optimized structure might be disturbed. The difference in the dark current between simulation and actual measurements was attributed to the non-ideal growth. It is believed avoiding deviations during the growth will decrease dark current for the same cut-off wavelengths. From another perspective, covering longer wavelengths with the same device design would be worth observing in terms of dark current performance.

If a new growth can be planned, the thickness of the SWIR side absorber should be increased to achieve higher quantum efficiency in the SWIR band. Growing a thicker SWIR absorber will also help to avoid spectral crosstalk between the bands.

In addition, large format focal plane arrays (FPA) can be fabricated using the wafer presented here or a newly grown wafer. Dark current, quantum efficiency, and noise performances of thousands of pixels can be characterized separately using a read-out integrated circuit (ROIC). Then, a statistical distribution of performances provided by pixels among a large format FPA can be obtained. Pictures can be captured by focusing a proper lens on the ROIC-coupled FPA. In addition to the quantitative investigation of pixel characteristics, the captured pictures can be inspected qualitatively in different scenes and weather conditions.

REFERENCES

[1] A. Rogalski, "Infrared detectors: status and trends," *Progress in quantum electronics*, vol. 27, no. 2-3, pp. 59–210, 2003.

[2] A. Şahin and S. Kocaman, "Low dark current designs for mesa type swir photodetectors," in *Infrared Technology and Applications XLVI*, vol. 11407, p. 1140704, SPIE, 2020.

[3] A. Şahin, M. S. Gül, F. Uzgur, and S. Kocaman, "A numerical design for swir/eswir dual-band operation with ingaas nbn structures," in *Quantum Sensing and Nano Electronics and Photonics XVIII*, vol. 12009, pp. 16–22, SPIE, 2022.

[4] A. Şahin, M. S. Gül, F. Uzgur, and S. Kocaman, "Dual-band ingaas nbn photodetectors at 2 μ m," *Applied Physics Letters*, vol. 120, no. 9, p. 091104, 2022.

[5] A. Daniels, *Field Guide to Infrared Systems, detectors, and FPAS*. SPIE Press, 2018.

[6] A. Beiser, "Concepts of modern physics," 2021.

[7] A. Rogalski and K. Chrzanowski, "Infrared devices and techniques," *Optoelectronics Review*, vol. 10, no. 2, pp. 111–136, 2002.

[8] S. Gunapala, S. Bandara, J. Liu, E. Luong, S. Rafol, J. Mumolo, D. Ting, J. Bock, M. Ressler, M. Werner, *et al.*, "Quantum well infrared photodetector research and development at jet propulsion laboratory," *Sensors and materials*, vol. 12, no. 6, pp. 327–351, 2000.

[9] C. Besikci, "Nature allows high sensitivity thermal imaging with type-i quantum wells without optical couplers: A grating-free quantum well infrared photodetector with high conversion efficiency," *IEEE Journal of Quantum Electronics*, vol. 57, no. 2, pp. 1–12, 2021.

[10] C. J. Hill, J. V. Li, J. M. Mumolo, and S. D. Gunapala, "Mbe grown type-ii mwir and lwir superlattice photodiodes," *Infrared Physics Technology*, vol. 50, no. 2,

pp. 187–190, 2007. Fourth International Workshop on Quantum Well Infrared Photodetectors.

[11] K. Itoigawa, H. Ueno, M. Shiozaki, T. Toriyama, and S. Sugiyama, "Fabrication of flexible thermopile generator," *Journal of Micromechanics and Microengineering*, vol. 15, pp. S233–S238, aug 2005.

[12] A. Minhas and D. Bansal, "Effect of beam length on the uncooled microbolometer performance," *Microsystem Technologies*, vol. 27, pp. 3219–3223, Aug 2021.

[13] R. W. Hoogeveen, R. J. van der A, and A. P. Goede, "Extended wavelength ingaas infrared (1.0–2.4 μm) detector arrays on sciamachy for space-based spectrometry of the earth atmosphere," *Infrared Physics & Technology*, vol. 42, no. 1, pp. 1–16, 2001.

[14] R. H. Wilson, K. P. Nadeau, F. B. Jaworski, B. J. Tromberg, and A. J. Durkin, "Review of short-wave infrared spectroscopy and imaging methods for biological tissue characterization," *Journal of Biomedical Optics*, vol. 20, no. 3, pp. 1 – 10, 2015.

[15] R. D. M. Scafutto, H. van der Werff, W. H. Bakker, F. van der Meer, and C. R. de Souza Filho, "An evaluation of airborne swir imaging spectrometers for ch4 mapping: Implications of band positioning, spectral sampling and noise," *International Journal of Applied Earth Observation and Geoinformation*, vol. 94, p. 102233, 2021.

[16] L. K. Schmidt, M. Bochow, H. K. Imhof, and S. E. Oswald, "Multi-temporal surveys for microplastic particles enabled by a novel and fast application of swir imaging spectroscopy – study of an urban watercourse traversing the city of berlin, germany," *Environmental Pollution*, vol. 239, pp. 579–589, 2018.

[17] K. Liang, J. Huang, R. He, Q. Wang, Y. Chai, and M. Shen, "Comparison of vis-nir and swir hyperspectral imaging for the non-destructive detection of don levels in fusarium head blight wheat kernels and wheat flour," *Infrared Physics & Technology*, vol. 106, p. 103281, 2020.

[18] A. A. Hosani, F. Alhmoudi, M. Almurshidi, and M. Meribout, "A real-time SWIR- image-based gas leak detection and localization system," in *Infrared Sensors, Devices, and Applications IX* (P. D. LeVan, P. Wijewarnasuriya, and A. K. Sood, eds.), vol. 11129, pp. 65 – 78, International Society for Optics and Photonics, SPIE, 2019.

[19] R. G. Driggers, V. Hodgkin, and R. Vollmerhausen, "What good is SWIR? Passive day comparison of VIS, NIR, and SWIR," in *Infrared Imaging Systems: Design, Analysis, Modeling, and Testing XXIV* (G. C. Holst and K. A. Krapels, eds.), vol. 8706, p. 87060L, International Society for Optics and Photonics, SPIE, 2013.

[20] M. M. Myers, D. C. Dayton, J. D. Gonglewski, G. Fertig, J. Allen, R. Nolasco, D. Burns, and I. Mons, "SWIR air glow mapping of the night sky," in *Advanced Wavefront Control: Methods, Devices, and Applications VIII* (D. C. Dayton, T. A. Rhoadarmer, and D. J. Sanchez, eds.), vol. 7816, p. 78160J, International Society for Optics and Photonics, SPIE, 2010.

[21] D. C. Dayton, J. Allen, R. Nolasco, J. D. Gonglewski, M. Myers, D. Burns, I. Mons, and F. Maia, "Passive SWIR airglow illuminated imaging compared with NIR-visible for low-light nighttime observations," in *Infrared Imaging Systems: Design, Analysis, Modeling, and Testing XXII* (G. C. Holst and K. A. Krapels, eds.), vol. 8014, p. 801407, International Society for Optics and Photonics, SPIE, 2011.

[22] M. L. Vatsia, "Atmospheric optical environment," tech. rep., ARMY NIGHT VISION LAB FORT BELVOIR VA, 1972.

[23] N. Cohen and O. Aphek, "Extended wavelength swir detectors with reduced dark current," in *Infrared Technology and Applications XLI*, vol. 9451, pp. 30–41, SPIE, 2015.

[24] M. P. Hansen and D. S. Malchow, "Overview of swir detectors, cameras, and applications," in *Thermosense Xxx*, vol. 6939, pp. 94–104, SPIE, 2008.

[25] W. Wang, C. Li, E. W. Tollner, R. D. Gitaitis, and G. C. Rains, "Shortwave

infrared hyperspectral imaging for detecting sour skin (burkholderia cepacia)-infected onions," *Journal of Food Engineering*, vol. 109, no. 1, pp. 38–48, 2012.

[26] X. Qiao, J. Jiang, X. Qi, H. Guo, and D. Yuan, "Utilization of spectral-spatial characteristics in shortwave infrared hyperspectral images to classify and identify fungi-contaminated peanuts," *Food Chemistry*, vol. 220, pp. 393–399, 2017.

[27] G. Keiser, *Optical fiber communications*, vol. 2. McGraw-Hill New York, 2000.

[28] G. L. Hansen, J. L. Schmit, and T. N. Casselman, "Energy gap versus alloy composition and temperature in hg1xcdxte," *Journal of Applied Physics*, vol. 53, no. 10, pp. 7099–7101, 1982.

[29] R. Gu, J. Antoszewski, W. Lei, I. Madni, G. Umana-Membrenao, and L. Faraone, "Mbe growth of hgcdte on gasb substrates for application in next generation infrared detectors," *Journal of Crystal Growth*, vol. 468, pp. 216–219, 2017. The 18th International Conference on Crystal Growth and Epitaxy (ICCGE-18).

[30] L. He, X. Fu, Q. Wei, W. Wang, L. Chen, Y. Wu, X. Hu, J. Yang, Q. Zhang, R. Ding, *et al.*, "Mbe hgcdte on alternative substrates for fpa applications," *Journal of electronic materials*, vol. 37, no. 9, pp. 1189–1199, 2008.

[31] W. Lei, R. Gu, J. Antoszewski, J. Dell, G. Neusser, M. Sieger, B. Mizaikoff, and L. Faraone, "Mbe growth of mid-wave infrared hgcdte layers on gasb alternative substrates," *Journal of Electronic Materials*, vol. 44, no. 9, pp. 3180–3187, 2015.

[32] J. Zanatta, G. Badano, P. Ballet, C. Largeron, J. Baylet, O. Gravrand, J. Rothman, P. Castelein, J. Chamonal, A. Million, *et al.*, "Molecular beam epitaxy growth of hgcdte on ge for third-generation infrared detectors," *Journal of electronic materials*, vol. 35, no. 6, pp. 1231–1236, 2006.

[33] C. Livanelioglu, Y. Ozer, and S. Kocaman, "Swir nightglow radiation detection around room temperature with depletion-engineered hgcdte on alternative substrates," *J. Opt. Soc. Am. B*, vol. 37, pp. 56–66, Jan 2020.

[34] I. Vurgaftman, J. R. Meyer, and L. R. Ram-Mohan, "Band parameters for iii–v compound semiconductors and their alloys," *Journal of Applied Physics*, vol. 89, no. 11, pp. 5815–5875, 2001.

[35] Y. Ma, X. Li, X. Shao, S. Deng, J. Cheng, Y. Gu, Y. Liu, Y. Chen, X. Zhu, T. Li, Y. Zhang, H. Gong, and J. Fang, "320x00d7;256 extended wavelength in_xga_{1-x}asx002f;inp focal plane arrays: Dislocation defect, dark signal and noise," *IEEE Journal of Selected Topics in Quantum Electronics*, vol. 28, no. 2: Optical Detectors, pp. 1–11, 2022.

[36] Y. Liu, Y. Ma, X. Li, X. He, Y. Chen, S. Deng, X. Shao, B. Yang, Y. Gu, T. Li, and H. Gong, "Noise behaviors of swir inxga1-xas/inp focal plane arrays as a function of lattice-mismatch degree," *Infrared Physics Technology*, vol. 123, p. 104136, 2022.

[37] H. Wieder, "Surface and interface barriers of in x ga 1- x as binary and ternary alloys," *Journal of Vacuum Science & Technology B: Microelectronics and Nanometer Structures Processing, Measurement, and Phenomena*, vol. 21, no. 4, pp. 1915–1919, 2003.

[38] H. Wieder, "Fermi level and surface barrier of ga x in1- x as alloys," *Applied Physics Letters*, vol. 38, no. 3, pp. 170–171, 1981.

[39] D. Sidor, G. Savich, and G. Wicks, "Surface leakage mechanisms in iii–v infrared barrier detectors," *Journal of Electronic Materials*, vol. 45, no. 9, pp. 4663–4667, 2016.

[40] C. Liu, Y. Li, Y. Zeng, *et al.*, "Progress in antimonide based iii-v compound semiconductors and devices," *Engineering*, vol. 2, no. 08, p. 617, 2010.

[41] I. Shafir, N. Snapi, D. Cohen-Elias, A. Glozman, O. Klin, E. Weiss, O. Westreich, N. Sicron, and M. Katz, "High responsivity ingaassb p–n photodetector for extended swir detection," *Applied Physics Letters*, vol. 118, no. 6, p. 063503, 2021.

[42] D. Cohen-Elias, N. Snapi, O. Klin, E. Weiss, S. Shusterman, T. Meir, and M. Katz, "Minority carrier diffusion length for electrons in an extended swir

inas/alsb type-ii superlattice photodiode," *Applied Physics Letters*, vol. 111, no. 20, p. 201106, 2017.

[43] R. Blank, S. Anglin, J. W. Beletic, S. Bhargava, R. Bradley, C. A. Cabelli, J. Chen, D. Cooper, R. Demers, M. Eads, *et al.*, "H2rg focal plane array and camera performance update," in *High Energy, Optical, and Infrared Detectors for Astronomy V*, vol. 8453, pp. 280–295, SPIE, 2012.

[44] J. F. Klem, J. K. Kim, M. J. Cich, G. A. Keeler, S. D. Hawkins, and T. R. Fortune, "Mesa-isolated ingaas photodetectors with low dark current," *Applied Physics Letters*, vol. 95, no. 3, p. 031112, 2009.

[45] K. Circir, M. H. Dolas, and S. Kocaman, "Optimization of in-device depleted passivation layer for ingaas photodetectors," *Infrared Physics & Technology*, vol. 97, pp. 360–364, 2019.

[46] Y. Arslan, F. Oguz, and C. Besikci, "640x512 extended short wavelength infrared in0.83ga0.17as focal plane array," *IEEE Journal of Quantum Electronics*, vol. 50, no. 12, pp. 957–964, 2014.

[47] N. Avishan, "Identification and characterization of traps in ingaas short wavelength infrared photodetectors by deep level transient spectroscopy," m.S. thesis, Middle East Technical University, 2016.

[48] X. Ji, B. Liu, Y. Xu, H. Tang, X. Li, H. Gong, B. Shen, X. Yang, P. Han, and F. Yan, "Deep-level traps induced dark currents in extended wavelength inxga1-xas/inp photodetector," *Journal of Applied Physics*, vol. 114, no. 22, p. 224502, 2013.

[49] Y. Liu, Y. Ma, X. Li, Y. Gu, Y. Zhang, H. Gong, and J. Fang, "Surface leakage behaviors of 2.6 μ m in0.83ga0.17as photodetectors as a function of mesa etching depth," *IEEE Journal of Quantum Electronics*, vol. 56, no. 2, pp. 1–6, 2020.

[50] Y. Ma, S. Deng, J. Cheng, Y. Gu, Y. Liu, Y. Zhang, X. Shao, X. Li, H. Gong, and J. Fang, "Towards surface leakage free high fill-factor extended wavelength ingaas focal-plane arrays," *IEEE Journal of Quantum Electronics*, vol. 55, no. 6, pp. 1–8, 2019.

[51] Y. Uliel, D. Cohen-Elias, N. Sicron, I. Grimberg, N. Snapi, Y. Paltiel, and M. Katz, "Ingaas/gaassb type-ii superlattice based photodiodes for short wave infrared detection," *Infrared Physics & Technology*, vol. 84, pp. 63–71, 2017.

[52] T. D. Nguyen, J. O. Kim, Y. H. Kim, E. T. Kim, Q. L. Nguyen, and S. J. Lee, "Dual-color short-wavelength infrared photodetector based on ingaassb/-gasb heterostructure," *AIP Advances*, vol. 8, no. 2, p. 025015, 2018.

[53] Z. Xie, Z. Deng, X. Zou, and B. Chen, "Inp-based near infrared/extended-short wave infrared dual-band photodetector," *IEEE Photonics Technology Letters*, vol. 32, no. 16, pp. 1003–1006, 2020.

[54] G. Savich, J. Pedrazzani, D. Sidor, S. Maimon, and G. Wicks, "Use of unipolar barriers to block dark currents in infrared detectors," in *Infrared Technology and Applications XXXVII*, vol. 8012, pp. 910–919, SPIE, 2011.

[55] G. Savich, J. Pedrazzani, D. Sidor, and G. Wicks, "Benefits and limitations of unipolar barriers in infrared photodetectors," *Infrared Physics & Technology*, vol. 59, pp. 152–155, 2013.

[56] P. Martyniuk, M. Kopytko, and A. Rogalski, "Barrier infrared detectors," *Opto-electronics review*, vol. 22, no. 2, pp. 127–146, 2014.

[57] S. Maimon and G. W. Wicks, "nbn detector, an infrared detector with reduced dark current and higher operating temperature," *Applied Physics Letters*, vol. 89, no. 15, p. 151109, 2006.

[58] A. Dehzangi, A. Haddadi, R. Chevallier, Y. Zhang, and M. Razeghi, "nbn extended short-wavelength infrared focal plane array," *Opt. Lett.*, vol. 43, pp. 591–594, Feb 2018.

[59] J. F. Klem, J. T. Olesberg, S. D. Hawkins, P. H. Weiner, J. Deitz, C. N. Kadlec, E. A. Shaner, and W. T. Coon, "Extended-short-wavelength infrared AlInAsSb and InPAsSb detectors on InAs," in *Infrared Technology and Applications XLVII* (B. F. Andresen, G. F. Fulop, and L. Zheng, eds.), vol. 11741, pp. 19 – 27, International Society for Optics and Photonics, SPIE, 2021.

[60] A. Haddadi, A. Dehzangi, R. Chevallier, S. Adhikary, and M. Razeghi, "Bias–selectable nbn dual–band long–/very long–wavelength infrared photodetectors based on inas/inas1xsbx/alas1xsbx type–ii superlattices," *IEEE Transactions on Electron Devices*, vol. 7, p. 3379, 2017.

[61] A. P. Craig, A. R. J. Marshall, Z.-B. Tian, S. Krishna, and A. Krier, "Mid-infrared inas0.79sb0.21-based nbn photodetectors with al0.9ga0.2as0.1sb0.9 barrier layers, and comparisons with inas0.87sb0.13 p-i-n diodes, both grown on gaas using interfacial misfit arrays," *Applied Physics Letters*, vol. 103, no. 25, p. 253502, 2013.

[62] H. S. Kim, E. Plis, J. B. Rodriguez, G. D. Bishop, Y. D. Sharma, L. R. Dawson, S. Krishna, J. Bundas, R. Cook, D. Burrows, R. Dennis, K. Patnaude, A. Reisinger, and M. Sundaram, "Mid-ir focal plane array based on type-ii inasgasb strain layer superlattice detector with nbn design," *Applied Physics Letters*, vol. 92, no. 18, p. 183502, 2008.

[63] Synopsys, Mountain View, CA, USA, *Sentaurus Device User Guide Version K-2015.06*, 2016.

[64] G. Hurkx, D. Klaassen, and M. Knuvers, "A new recombination model for device simulation including tunneling," *IEEE Transactions on Electron Devices*, vol. 39, no. 2, pp. 331–338, 1992.

[65] Y. Ma, S. Deng, J. Cheng, Y. Gu, Y. Liu, Y. Zhang, X. Shao, X. Li, H. Gong, and J. Fang, "Towards surface leakage free high fill-factor extended wavelength ingaas focal-plane arrays," *IEEE Journal of Quantum Electronics*, vol. 55, no. 6, pp. 1–8, 2019.

[66] W. K. Metzger, M. W. Wanlass, R. J. Ellingson, R. K. Ahrenkiel, and J. J. Carapella, "Auger recombination in low-band-gap n-type ingaas," *Applied Physics Letters*, vol. 79, no. 20, pp. 3272–3274, 2001.

[67] M. Boroditsky, I. Gontijo, M. Jackson, R. Vrijen, E. Yablonovitch, T. Krauss, C.-C. Cheng, A. Scherer, R. Bhat, and M. Krames, "Surface recombination measurements on iii–v candidate materials for nanostructure light-emitting diodes," *Journal of Applied Physics*, vol. 87, no. 7, pp. 3497–3504, 2000.

[68] J. Chen, Z. Zhang, M. Zhu, J. Xu, and X. Li, "Optimization of ingaas/inalas avalanche photodiodes," *Nanoscale Research Letters*, vol. 12, no. 33, 2017.

[69] J. Xiaoli, L. Baiqing, T. Hengjing, L. Xue, S. Ming, Z. Ying, X. Yue, G. Haimei, and Y. Feng, "Improvement of surface leakage current of 2.6 um ingaas photodetectors by using inductive coupled plasma chemical vapor deposition technology," *Jpn. J. Appl. Phys*, vol. 54, no. 4S, 2015.

[70] R. People, K. W. Wecht, K. Alavi, and A. Y. Cho, "Measurement of the conduction-band discontinuity of molecular beam epitaxial grown in0.52al0.48as/in0.53ga0.47as, n-n heterojunction by c-v profiling," *Applied Physics Letters*, vol. 43, no. 1, pp. 118–120, 1983.

[71] D. F. Welch, G. W. Wicks, and L. F. Eastman, "Calculation of the conduction band discontinuity for ga0.47in0.53as/al0.48in0.52as heterojunction," *Journal of Applied Physics*, vol. 55, no. 8, pp. 3176–3179, 1984.

[72] C. Peng, A. Ketterson, H. Morkoc, and P. Solomon, "Determination of the conduction-band discontinuity between in0. 53ga0. 47as/in0. 52al0. 48as using n+-ingaas/inalas/n–ingaas capacitors," *Journal of applied physics*, vol. 60, no. 5, pp. 1709–1712, 1986.

[73] A. Sandhu, Y. Nakata, S. Sasa, K. Kodama, and S. Hiyamizu, "Energy-band offset of in0.53ga0.47as–in0.52(ga1-xAIx)0.48as heterostructures, determined by photoluminescenee excitation spectroscopy of quasi-parabolie quantum wells grown by MBE," *Japanese Journal of Applied Physics*, vol. 26, pp. 1709–1712, oct 1987.

[74] F. Uzgur and S. Kocaman, "Barrier engineering for hgcdte unipolar detectors on alternative substrates," *Infrared Physics & Technology*, vol. 97, pp. 123–128, 2019.

[75] F. Uzgur, U. Karaca, E. Kizilkan, and S. Kocaman, "All ingaas unipolar barrier infrared detectors," *IEEE Transactions on Electron Devices*, vol. 65, no. 4, pp. 1397–1403, 2018.

[76] F. Uzgur and S. Kocaman, "A dual-band HgCdTe nBn infrared detector design," in *Infrared Sensors, Devices, and Applications IX* (P. D. LeVan, P. Wijewarna-

suriya, and A. K. Sood, eds.), vol. 11129, pp. 25 – 31, International Society for Optics and Photonics, SPIE, 2019.

[77] Y. Zhang, Y. Gu, Z. Tian, A. Li, X. Zhu, and Y. Zheng, "Wavelength extended 2.4μm heterojunction ingaas photodiodes with inalas cap and linearly graded buffer layers suitable for both front and back illuminations," *Infrared Physics Technology*, vol. 51, no. 4, pp. 316–321, 2008.

[78] Y. Zhang, Y. Gu, Z. Tian, K. Wang, A. Li, X. Zhu, and Y. Zheng, "Performance of gas source mbe-grown wavelength-extended ingaas photodetectors with different buffer structures," *Journal of Crystal Growth*, vol. 311, no. 7, pp. 1881–1884, 2009. International Conference on Molecular Beam Epitaxy (MBE-XV).

[79] A. Stano, "Chemical etching characteristics of ingaas/inp and inalas/inp heterostructures," *J. Electrochem. Soc.*, vol. 134, no. 448, 1987.

[80] Y.-G. Zhang, Y. Gu, X.-Y. Chen, Y.-J. Ma, X. Li, X.-M. Shao, H.-M. Gong, and J.-X. Fang, "Iga-rule 17 for performance estimation of wavelength-extended ingaas photodetectors: validity and limitations," *Appl. Opt.*, vol. 57, pp. D141–D144, Jun 2018.